This is to certify that the
dissertation entitled

EPR Studies of Electron and Proton Transfer in
Cytochrome *c* Oxidase

presented by

Shujuan Xu

has been accepted towards fulfillment
of the requirements for the

Doctoral degree in Chemistry, Biochemistry and Molecular Biology

John L McCracken
Major Professor's Signature

August 15, 2008
Date

EPR STUDIES OF ELECTRON AND PROTON TRANSFER IN CYTOCHROME *C* OXIDASE

By

Shujuan Xu

A DISSERTATION

Submitted to
Michigan State University
In partial fulfillment of the requirements
For the degree of

DOCTOR OF PHILOSOPHY

Chemistry, Biochemistry and Molecular Biology

2008

ABSTRACT

EPR STUDIES OF ELECTRON AND PROTON TRANSFER IN CYTOCHROME *C* OXIDASE

By

Shujuan Xu

An understanding of the mechanism of electron and proton transfer in cytochrome *c* oxidase (C*c*O) is essential for a full understanding of the process of energy transduction in this key respiratory enzyme. Combining site-directed mutagenesis and EPR methods, some mutants at residue S44 associated with heme *a* were created and studied to determine its influence on the spectral characteristics of C*c*O. EPR data on S44G supports the prediction that this hydrogen bonding partner of the histidine ligand of heme *a* is one determinant of the EPR spectral difference between bovine and bacterial C*c*O. Of additional interest, the pH-dependence of the EPR spectrum of S44D and fast electron transfer studies showing dramatically inhibited electron transfer from Cu_A to heme *a* at high pH, indicate a proton-coupled electron transfer mechanism. This mutant could provide a new tool for studying proton and electron transfer reactions in cytochrome *c* oxidase.

Using the non-redox active Mg site of CcO, substituted with Mn, as a probe, proton/water movement was studied in its vicinity. Electron nuclear double resonance (ENDOR) studies provided us with detailed information on hyperfine coupling interactions between the Mn site and its liganded water molecules. Further studies of oxidized and reduced C*c*O, plus and minus cyanide or azide, with Electron spin echo envelope modulation (ESEEM) technique showed cyanide binding to the Mn in the

reduced enzyme. This finding supports the hypothesis that reduction of Cu_A causes one of the water ligands of the Mn to become a hydroxide ion, playing an important role in proton pumping in C*c*O. ESEEM simulations also provide support for this hypothesis.

As a more sensitive technique, high-field EPR was used to study C*c*O with the hope of gaining more information with higher resolution. The difference in Mn spectra of the reduced and the oxidized C*c*O was observed in *Rs.* C*c*O, which agrees well with findings in *Pd.* C*c*O. Further studies of super hyperfine coupling interactions between Mn and its water ligands in the oxidized and reduced enzymes showed some interesting data. The narrowing effect due to deuterium exchange was observed in the oxidized C*c*O, which can be potentially used to quantify the number of coupled protons. However, experiments with the reduced enzyme in $H_2{}^{17}O$ and ^2H_2O failed to show supposedly broadening and narrowing effects respectively. The possible reasons were explored and explained.

To my dear parents

Acknowledgements

I would like to express my sincerest gratitude to all those who made my Ph.D. period enjoyable.

I want to thank my advisor in Biochemistry, Dr. Shelagh Ferguson-Miller, who introduced me to the fascinating world of cytochrome *c* oxidase, deserves my deepest gratitude for all the help, guidance and encouragement she has given me during these years. With her enormous amounts of integrity, determination and dedication she has gained my greatest admiration and uppermost respect. I have furthermore to thank my advisor in Chemistry, Dr. John McCracken for agreeing to be my advisor when my previous advisor moved to another university. John has generously shared with me his vast knowledge of EPR theory and instrumentation and has been an endless source of advice and encouragement. I also wish to express my gratitude to my committee members: Dr. Robert, Cukier, Dr. Mike, Garavito, and Dr. David Weliky. They gave me great suggestions during my oral exam, annual report presentations.

There are also many numbers of coworkers I would like to thank. Many discussions I had with Dr. Denise Mills were invaluable and collaboration with her was a great experience I would never forget. Dr. Carrie Hiser helped me with molecular biology part to ensure my project go well. Her many suggestions helped me do well with my presentations. Dr. Martyn Sharpe taught me many things and "pushed" me to do better in my research. Dr. Denis Proshlyakov provided me assistance using his experiment setup. He is also a good source of knowledge and advice. And would also like to thank Dr. Rajendra Muthukumaran, who spent many hours teaching me how to use EPR machines and shared with me his knowledge of EPR theory. I also had many useful discussions

with other lab members in both Chemistry and Biochemistry: Dr. Bryan Schmidt, Dr. Ling Qin, Namjoon Kim, Jian Liu, Xi, Zhang, Leann Buhrow, Monika, Shannon, Morey, and Tom Casey as well as all the others who I interacted with through my Ph.D. Special thank comes to my lab member, Mattew, Krzyaniak who helped me a lot with ENDOR and ESEEM simulations and EPR instrumentation.

I would also like to acknowledge all my friends here at Michigan State University for their help and support. Without their friendship, I would not make it. My deepest thank to my husband, Zhenwei, for his love and support.

My deepest thank to my family!

TABLE OF CONTENTS

Chapter 5

LIST OF TABLES

LIST OF FIGURES

Images in this dissertation are presented in color

Chapter 1:
AN INTRODUCTION TO CYTOCHROME *C* OXIDASE AND EPR SPECTROSCOPY

1 The respiratory chain

Oxidative phosphorylation is the process by which energy is produced in aerobic organisms. In eukaryotes, oxidative phosphorylation occurs in the mitochondria, where O_2 is reduced to H_2O by electrons donated by NADH or $FADH_2$. A well-accepted chemiosmotic theory was proposed by Peter Mitchell in 1961 and was the basis for understanding ATP synthesis. The theory states that oxidative phosphorylation involves the flow of electrons through a chain of membrane-bound electron carriers. The electrons are used to reduce oxygen to water resulting the release of free energy as an exergonic process, which is coupled to the transport of protons against the positive outside membrane potential, establishing a transmembrane electrochemical potential. The transmembrane flow of protons down their concentration gradient through the membrane protein ATP synthase, provides the energy for ATP synthesis.

The discovery that mitochondria are the site for oxidative phosphorylation in eukaryotes marked the beginning of biological studies into energy transduction. The mitochondria have two lipid membranes. The outer membrane is permeable to small molecules (MW <5000 Da) and ions, which move freely through transmembrane channels formed by porin proteins. The inner membrane is impermeable to most small charged molecules, including protons, except through specific transport systems. The inner mitochondrial membrane bears the respiratory chain and ATP synthase. The mitochondrial matrix, enclosed by the inner membrane, contains many enzymes such as the pyruvate dehydrogenase complex, enzymes of the TCA cycle, and the fatty acid ß-

oxidation pathway. During the proton translocation process, protons are pumped from the mitochondrial matrix. This becomes negatively charged due to the uptake of protons, and is referred to as the negative/N-side. The intermembrane space becomes positively charged due to the pumped protons, and is referred to as the positive/P-side.

The respiratory chain is made up of four separate complexes (**Fig. 1.1**). They are: NADH dehydrogenase (Complex I), succinate dehydrogenase (Complex II), cytochrome bc_1 (Complex III), and cytochrome *c* oxidase (Complex IV). Complexes I and II catalyze electron transfer to ubiquinone from different electron donors: NADH (complex I) and succinate (complex II). Complex III transfers electrons from reduced ubiquinone to a soluble cytochrome *c*, and complex IV completes the reaction by transferring electrons from cytochrome *c* to O_2.

Complex I (NADH dehydrogenase) is a large enzyme composed of forty-two different peptide chains, including an FMN-containing protein and at least six iron-sulfur centers. Complex I catalyzes two simultaneous and obligatorily coupled reactions: it removes two electrons from NADH and transfers them to a lipid-soluble carrier, ubiquinone (Q). The reduced product, ubiquinol (QH_2), is free to diffuse within the membrane. At the same time, Complex I pumps four protons (H^+) across the membrane, producing a proton gradient. High-resolution electron microscopy shows that complex I is L-shaped with one arm of the L in the membrane and the other extending into the matrix.

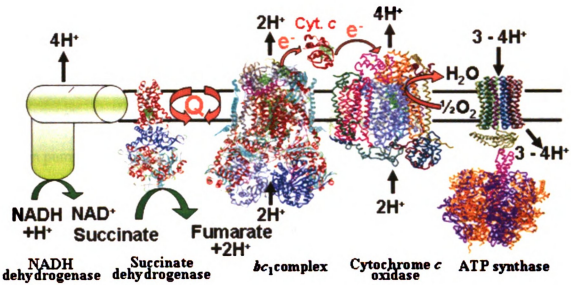

Figure1.1: The mitochondria respiratory chain. The structure represents the crystallographically defined structure of each enzyme [1-4]. This figure is a figure courtesy of Dr. Denise Mills.

Complex II (succinate dehydrogenase) is the only membrane-bound enzyme in the citric acid cycle (TCA cycle). It is smaller and simpler than complex I but still contains five prosthetic groups of two types and four different protein subunits. Subunits A and B contain three 2Fe-2S clusters, bound FAD and a binding site for the substrate, succinate. Subunits C and D are integral membrane proteins. They contain a heme *b* and a binding site for ubiquinone, which is the final electron acceptor in the reaction catalyzed by complex II. It serves to funnel additional electrons into the quinone pool (Q) by removing electrons from succinate and transferring them (via FAD) to Q. Complex II is not a proton pump, therefore it does not produce a proton gradient.

Complex III (bc_1 complex) transfers two electrons from ubiquinol (QH_2) to two molecules of the water-soluble electron carrier cytochrome *c*, releasing two protons from ubiquinol on the outside, and translocates an additional two protons from the N side to the P side of the membrane per pair of electron transferred via the Q-cycle, producing a proton gradient (a net four protons are translocated). Complex bc_1 contains four electron transfer centers, two hemes, cytochrome c_1, and an iron-sulfur protein as well.

Cytochrome *c* is a soluble protein of the intermembrane space. It plays a role as an electron carrier which accepts electrons from complex III and then transfers them to complex IV (cytochrome *c* oxidase).

Complex IV (cytochrome *c* oxidase (C*c*O)) is located at the end of the respiratory chain. It catalyzes the reduction of molecular oxygen to water at the binuclear heme

a_3/Cu_B center. The reaction is coupled to proton translocation across the mitochondrial or bacterial membrane, contributing a transmembrane pH gradient, which provides energy for adenosine triphosphate (ATP) synthesis. The ATP produced is then delivered to different locations throughout the cell, providing the necessary energy supply to a broad variety of biochemical reactions. Because of the extreme importance of C*c*O for the bioenergetic reactions in living cells, it has been an important research topic for the past decades from its first discovery by MacMunn [5], and further confirmation by Keilin [6]. It took scientists more than a century to have a better, yet not full, understanding of cytochrome *c* oxidase (C*c*O).

2. Cytochrome c oxidase (C*c*O)

C*c*O catalyzes a seemingly simple reaction: the four-electron reduction of molecular oxygen to two waters. In the reaction, four equivalents of ferrocytochrome *c* provide four electrons, one at a time, and the enzyme takes up four substrate protons. The reaction is highly exergonic and the free energy released by this reaction is stored in the form of an electrochemical gradient across the membrane[7]. The active site of the enzyme is buried within the membrane, and the electrons and protons that are used to form water come from the opposite sides of the membrane, which results in charge separation across the membrane (**Fig.1.2**). The reduction of one dioxygen molecule to two waters results in the net movement of four charges across the membrane (four electrons consumed from the outside, four protons consumed from the inside), and therefore the generation of a transmembrane potential gradient. This deceptively simple vectorial mechanism makes

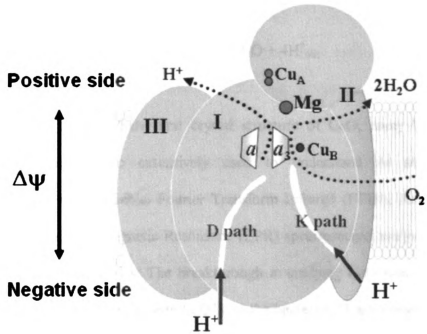

Figure 1.2: Overall structure of C*c*O showing arrangements of metal centers and proton uptake pathways. The picture is from Schemidt B. et al[8]

cytochrome *c* oxidase a powerful bioenergetic machine. What is more amazing is its ability to translocate protons across the membrane. For each turnover, four additional protons are pumped across the membrane (Eq.1.1).

$$4 \text{ cyt. } c^{2+} + 8\ H^{+}_{in} + O_2 \rightarrow 4 \text{ cyt. } c^{3+} + 2H_2O + 4H^{+}_{out} \qquad 1.1$$

Before the advent of the first crystal structure of C*c*O, many biochemical and biophysical methods were extensively used to understand its structure-function relationship such as UV-visible, Fourier Transform Infrared (FTIR), Resonance Raman (RR), and Electron Paramagnetic Resonance (EPR) spectroscopic analyses, site-directed mutagenesis, and fast kinetics. The breakthrough in studying C*c*O was the atomic level X-ray crystal structures from bovine C*c*O[9] and the bacterium *Paraccocus denitrificans* [3]. These crystal structures provided a full picture of the enzyme, and also verified many findings on the positions of the metal sites by other biophysical and biochemical methods. Upon careful inspection of the first two crystal structures, aqueous channels, suggested previously by mutagenesis, were clearly confirmed. These two channels were later established to be two proton uptake pathways. In 2002 and 2006, two more crystal structures from the bacterium *Rhodobacter sphaeroides* [4, 10] were determined at 2.3 Å /2.0 Å resolutions. With the aid of high-resolution crystal structures, the Ferguson-Miller lab is able to address many fundamental questions, such as the proton/water transfer routes.

2.1 The overall structure

Mammalian cytochrome *c* oxidase contains four redox-active metal centers and thirteen subunits. The complexity of its physical structure, and the difficulty of manipulating the genome using site-directed mutagenesis, has made structure-function analysis a difficult task. *Rhodobactor sphaeroides* (*Rs.*) C*c*O, on the other hand, has only four subunits but contains the same redox-active metal centers. It shows a strong sequence homology to the mammalian C*c*O and is functionally equivalent to its mammalian counterpart; therefore it is a useful model for structure-function analysis[11] (**Fig.1.3**). Of the four subunits, subunit I is the largest subunit, with twelve transmembrane helices. It contains the redox-active heme *a*, the heme a_3/Cu_B active site, and a non-redox active calcium ion whose role is still not clear. Subunit II has only two transmembrane helices with an extra-membrane beta-pleated region that contains the dinuclear Cu_A center, the initial electron acceptor from ferrocytochrome *c*. At the interface of subunits I and II is another metal center, a Mg^{2+}, liganded by residues from both subunits. Subunit III contains seven transmembrane helices which form a V-shape, and has no metal centers. The function of subunit III is not well understood, but it has been shown that the absence of subunit III promotes 'suicide' inactivation of the enzyme, which may be due to the loss of the structural integrity of the Cu_B center during turnover. Subunit IV of *Rs.* C*c*O has only one transmembrane helix that interacts with subunit I via lipids, but its function, unfortunately, is still unknown (**Fig.1.4**).

Six phospholipid molecules were identified in the bovine structure (PDB ID: 1occ). Based on the electron density map, they were assigned as phosphatidylethanolamines (PE). Two of the PE molecules were found in a cleft formed by the helices of subunit III.

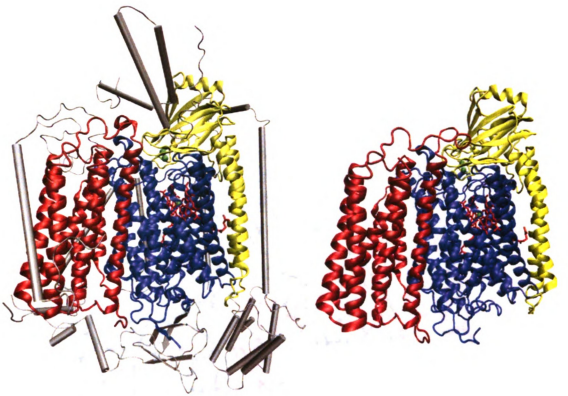

Figure 1.3: Comparison of mammalian and bacterial C*c*O crystal structures. The bacterial C*c*O structure from *Rs.* (right) contains subunits that are highly similar to three core subunits of bovine C*c*O (left), showing in yellow, blue, and red. They both contain the same spatial alignment of the redox active metal cofactors (hemes are shown in red, Cu_A and Cu_B are shown in green). *Rs.* C*c*O contains subunit IV consisting of only one transmembrane helix (not shown in this picture). Bovine C*c*O contains additional ten subunits (shown in gray in the picture). The figure is made using VMD software program.

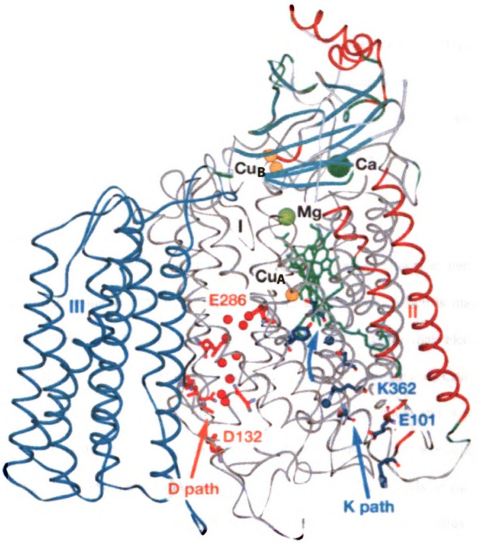

Figure 1.4: Overall structure of *Rhodobacter sphaeroides* CcO. Diagram of four subunit structure of *Rhodobacter sphaeroides* cytochrome c oxidase showing two proton uptake pathways, The D (red), and K (blue) paths. The three redox-active centers are labeled: dinuclear Cu_A center, heme *a*, heme a_3/Cu_B binuclear center. The two non-redox centers, Mg^{2+}, and Ca^{2+} are also included. This figure is a modification of figure from Mills, D. et al.[12]

The other four PE molecules were found at the interface between subunits I, III, and IV. Subunit IV has little direct interaction with the other three subunits, as revealed by the X-ray structure, but maintains its contact via lipid molecules. In the bovine crystal structures, over two hundred water molecules per monomer were resolved. Most of them were found on the surfaces exposed to the solvent. Still, quite a few water molecules were within the enzyme molecule forming hydrogen-bonded networks that are believed to facilitate proton pumping [13] (**Fig.1.5**).

2.1.1 The redox-active metal centers

Cytochrome *c* oxidase has four redox-active metal centers: heme *a*, heme a_3, the dinuclear copper center (Cu_A), and a type II copper center (Cu_B) which is magnetically coupled with heme a_3. Time-resolved spectroscopies have shown that electrons are transferred from a reduced cytochrome *c* to heme *a*, then to the heme a_3/Cu_B binuclear center, the catalytic site of the enzyme, where molecular oxygen binds and is reduced to water. For the Cu_A dinuclear center, the crystal structure [13] shows that two copper atoms are bridged by two cysteines, with two histidines for the terminal ligands of each copper; a methionine residue ligates one copper atom and another glutamate ligates the other copper atom loosely (**Fig.1.6**). The planes of both the heme *a* and the a_3 are perpendicular to the membrane plane and facing each other. Heme *a* has two axial histidine ligands and is a low-spin heme. Heme a_3 is also ligated by a single histidine residue, and is a high spin heme. The Cu_B site is coordinated by three imidazoles of histidines, in agreement with mutagenesis studies. In the bovine crystal structures, Cu_A is 19Å from heme *a* and

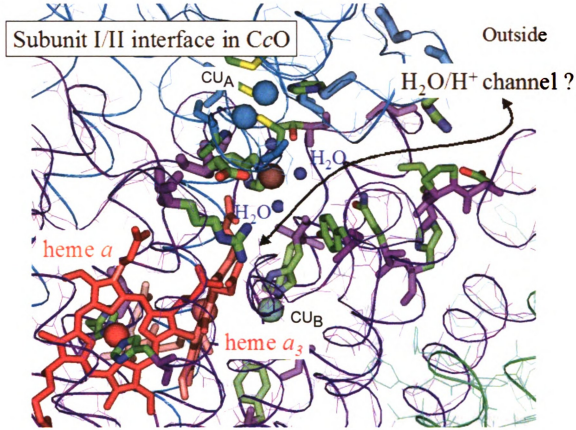

Figure1.5: Proposed water channel in bovine C*c*O. Blue ribbons on the top are from subunit II which houses dinuclear Cu_A site (blue spheres). The green ribbons on the far right represent subunit III, which does not have any metal centers and its function is unclear. The purple ribbons represent subunit I which contains two hemes (red) and Cu_B site (light green sphere). The proposed water channel is shown as the gap between subunits I and II, beginning near heme a_3 propionates and the Mg/Mn site (brown sphere), with residues lining the channel in ball-and stick form. The three small blue spheres represent crystallographically visible water molecules. The figure is from Florens, L. et al.[14]

22 Å from heme a_3. Both hemes *a* and a_3, and Cu_B are located at about the same depth in the membrane, which is about 1/3 of the membrane spanning region.

2.1.2 The non-redox active metal centers

Besides the redox-active metal centers, crystal structures of bovine and bacterial C*c*O revealed two non-redox active metal centers. The Mg site is12Å from the surface of the protein, at the bottom of a proposed water channel. It bridges subunits I and II, shares one ligand with the Cu_A center, and is bonded through a histidine ligand and a water molecule to the propionate of heme a_3. The role of this site is not clear. However, it is located in the vicinity of an apparent water channel, which hints that it may function as a regulator of proton/water exit [7]. The other is the Ca/Na binding site, which is located near the P side of the membrane in subunit I and appears to be accessible to solvent. It is formed by residues on the top of helix I of subunit I and in the loop following it, with possible additional contacts from the loop (**Fig.1.6**).

2.2 The oxygen chemistry

During the catalytic cycle, electrons are transferred from reduced cytochrome *c* to Cu_A, from Cu_A to heme *a* and from there to the binuclear catalytic center heme a_3/Cu_B. The measured steady-state activity of the *Rs.*C*c*O is ~1600 to 2,000 s^{-1} at pH 6.5 [11]. Spectroscopic and chemical methods have provided a quite clear picture of the mechanism of oxygen chemistry carried out by C*c*O (**Fig.1.7**). Cu_A and heme *a* are the electron carriers which transfer two electrons from reduced cytochrome *c*, one at a time, to heme *a* and then to the binuclear center. Once the heme a_3 and Cu_B center are reduced,

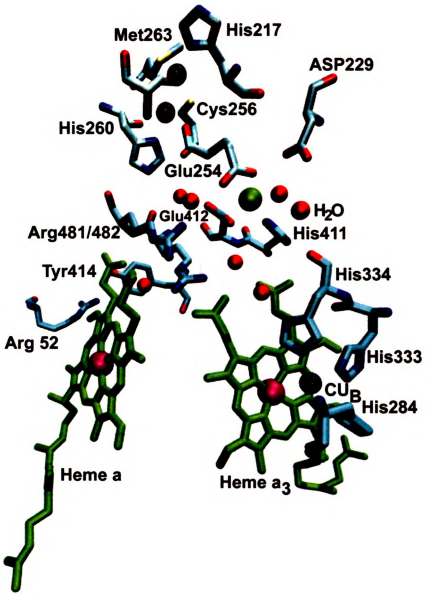

Figure1.6: Structure showing the arrangement of metal centers and associated amino acids in bacterial C*c*O. The copper centers are shown as black spheres, Mg is shown as green sphere, heme *a* and heme a_3 are both in green.

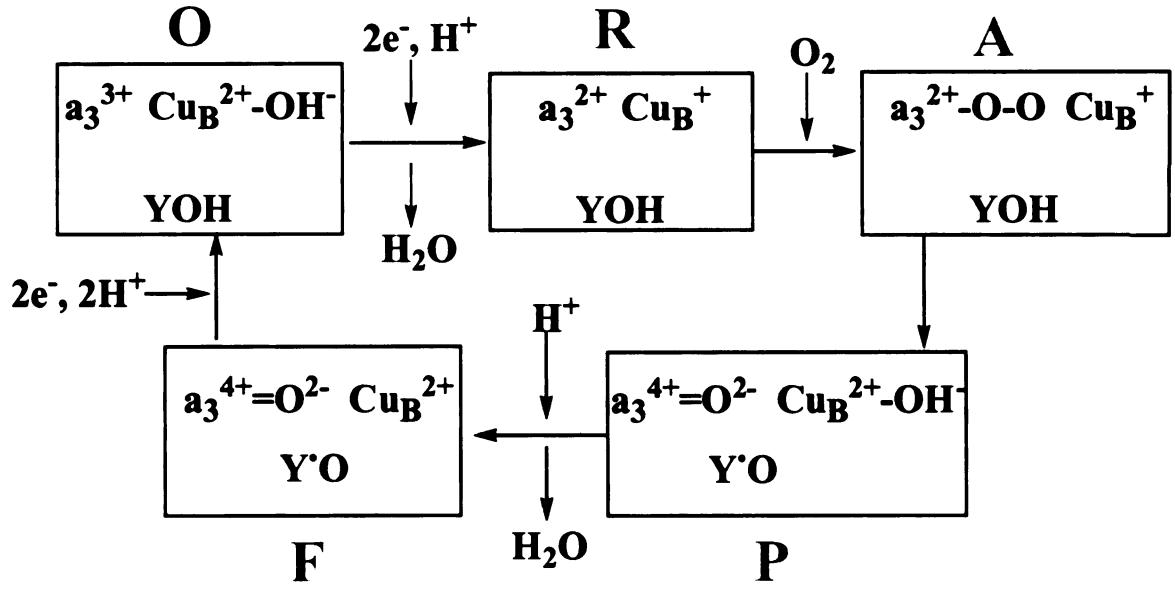

Figure 1.7: Proposed catalytic reactions at the active site of C*c*O. Abbreviation used as follows: Y, Y288 (*R.sphaeriodes* numbering); R, reduced; A, oxy; P, oxoferryl; F, protonated form of P; O, oxidized. Pumped protons are not shown in the view. The two phases of the catalytic cycle merge to a certain extent, but the metal reduction is essentially from O to R. The figure is reproduction of a figure from Mills, D. et al.[12].

O_2 binds to the binuclear center and transiently forms the intermediate A (Fe^{2+}-O_2). The O-O bond is rapidly broken in a concerted fashion requiring a total of four electrons and at least one proton. Three of the four electrons are donated by the Fe_{a3}^{2+} and Cu_B^{+} center, forming the ferryl-oxo state, Fe^{4+}=O, and cupric ion Cu_B^{2+}. If heme *a* is oxidized, the electron required to break the O-O bond appears to come from a nearby tyrosine forming a radical. However, if heme *a* is in its reduced state, then the electron comes from heme *a*.

2.3 Electron and proton transfer theory

2.3.1 Electron transfer in biological system

Numerous processes in biology involve electron transfer reactions, including photosynthesis, and respiration. Many metabolic pathways as well as detoxification routes also involve electron transfer. Classical theory (Marcus theory) was used to explain inner-sphere and outer-sphere electron transfer and the electron transfer rate is given by the expression[15]:

$$k_{ET} = \frac{2\pi}{\hbar} H_{AB}^2 \frac{1}{\sqrt{4\pi\lambda k_b T}} \exp\{\frac{-(\lambda + \Delta G^o)^2}{4\lambda k_b T}\} \qquad 1.2$$

Where k_{ET} is the electron transfer rate, H_{AB} is the electronic coupling between the initial and final states, λ is the reorganization energy, and ΔG^o is the total Gibbs free energy change for the electron transfer reaction, and k_b is the Boltzmann constant. The key parameters are depicted in **Fig.1.8**.

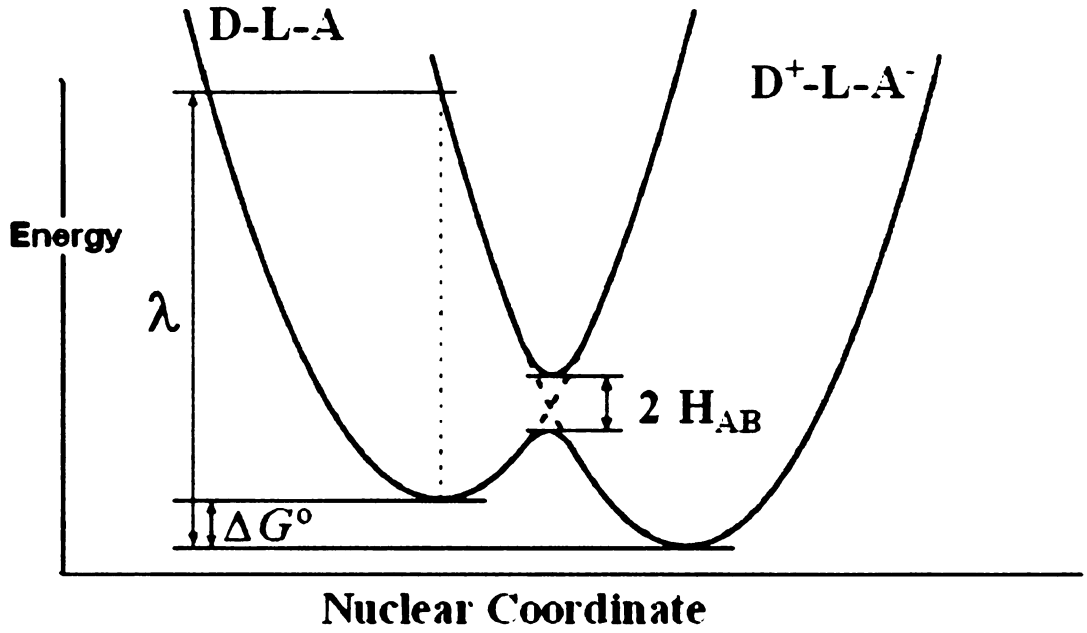

Figure 1.8: Potential energy diagram showing parameters from Marcus electron transfer equation. The left hand parabola represents the potential energy surface for the nuclear motion of the reactants in the initial state, and the right hand parabola represents the potential energy surface for the nuclear motion of the products in the final state. The λ represents the reorganizational energy of the eletron transfer reaction and ΔG° is the driving force for the electron transfer reaction, and H_{AB} represents the electronic coupling between the initial and final states. The figure is the modification of the diagram from the following link: http://www.life.uiuc.edu/crofts/bioph354/lect19.html

According to the Marcus theory, the activation barrier for electron transfer depends on three factors: the driving force (ΔG^o), the reorganization energy (λ), and the distance between the redox centers. The reorganization energy reflects the extent of inner sphere (λ_{in}) and outer sphere (λ_{out}) nuclear re-arrangement upon electron transfer. The balance between ΔG^o and λ result in different electron transfer rates.

Protein structure is an important determinant of the reorganization energy in biological electron transfer reactions. Molecular dynamic simulations using dielectric continuum models indicate that embedding a redox center inside a cavity with low dielectric constant can greatly lower the outer-sphere reorganization energy[16]. Furthermore, it is found that constraining the coordination environment around metal centers could reduce the inner-sphere reorganization energy [17]. This is demonstrated by an experiment in which a small water soluble protein, cytochrome *c*, was treated with guanidine-HCl to unfold the protein and alter the environment such that the redox potential of the heme was changed, as well as the reorganization energy, altering the electron transfer rate[18].

Another factor in the Marcus equation is the H_{AB}, the electronic coupling. It reflects the strength of the reaction between reactants and products at the nuclear configuration of the transition state. When donors and acceptors are separated by a long distance (≥10 Å), the interaction between donors and acceptors are weak. In electron transport enzymes, because of the folding of polypeptides, electron transfer centers are often buried deeply in polypeptides and cannot come into contact. In 1974, Hopfield

proposed a tunneling model in which the coupling depends exponentially on the distance (r) between redox centers [19]. Combining Hopfield's tunneling model with McConnell's model [20], it is seen that the coupling depends on both the length and the nature of the spacing elements between the donor and acceptor. Electron transfer between the donor and acceptor, spaced by the spacing elements is referred to as tunneling, and is generally found to have an exponential dependence on the distance between the donor and the acceptor described in equation 1.4:

$$k_{ET}(r_{DA}) = k_0 \exp(-\beta r_{DA}) \qquad 1.3$$

where k_0 is a temperature prefactor, r_{DA} is the distance between the donor and the acceptor, and β is the exponential decay constant and reflects the nature of the intervening matter. Different donor-acceptor systems have different β values due to the variant nature of the bridge elements, therefore they have different electron transfer rates. For example, conjugated polyenes exhibit smaller β values, as low as 0.04 $Å^{-1}$ and show remarkably efficient electron transfer over long distances [21] while in proteins possessing α-helix or β-sheet, the β values are about 1.0-1.3 $Å^{-1}$.

Long-range electron transfer is commonly found in many enzymes and can still show high efficiency. For example, electron transfer in C*c*O, from Cu_A to heme *a*, is over 19 Å with an electron transfer rate of 2-9 $x10^4 s^{-1}$. Some possible electron transfer pathways were proposed and identified by mutagenesis[22]. The very efficient long-range electron transfer from Cu_A to heme *a* ($2x10^4 s^{-1}$) proceeds at a very low driving force (ΔG^o= -0.05eV) [23]. Three electronic coupling routes have been proposed to explain the fast electron transfer [24-27]. Some electron coupling pathways between heme *a* and heme a_3

are also considered in which the axial histidine ligands of heme *a* and heme a_3 are involved [25, 28]. It is still controversial as to whether there are particular routes for electron transfer facilitated by the protein, or whether the β factor for electron movement through protein is approximately the same as the reorganization energy.

Redox reactions can involve both electron and proton transfers. The coupling between electrons and protons is an important feature in the complexes of the respiratory chain. Proton-coupled electron transfer (PCET) mechanisms have been studied in pH-dependent rate studies of some self-exchange reactions in model systems, in which a rate is increased with the increasing pH. Reviews concerning PCET in metal complexes came out in the 1990s [29]. In the same period, a series of theoretical calculations of the PCET mechanism were published by several researchers [30-32]. As more insights are gained from the study of enzymes and their biological processes, it became more evident that biological systems take great advantage of PCET. Over the time span of evolution, complex structures have evolved so that the PCET mechanisms are utilized to drive vectorial proton translocation. The coupling of electron and proton transfer is at the heart of photosynthesis, respiration, nitrogen fixation, and many other key bioenergetic processes. Photosystem II is a good example of how the biological system uses PCET. In the photosynthetic water oxidation reaction depicted in **Fig.1.9,** a substantial body of data provide evidence that both the oxidation of tyrosine and the reduction of the tyrosine

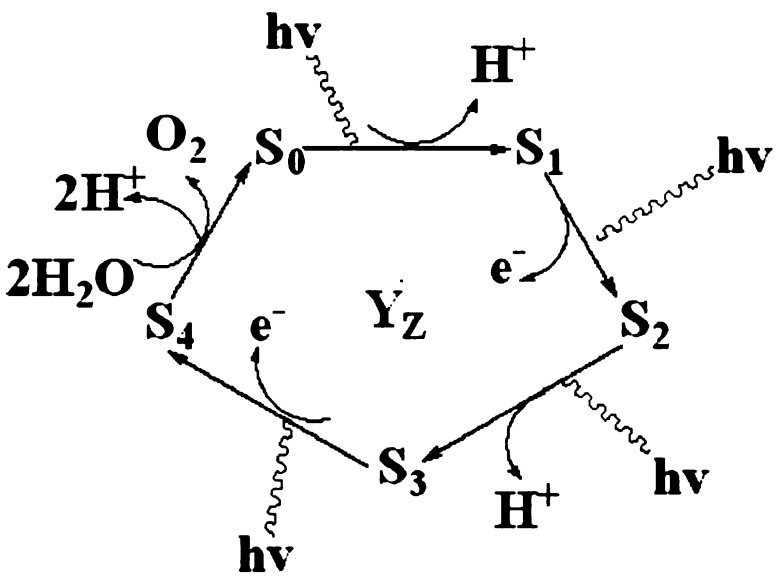

Figure 1.9: S-cycle of Photosystem II. The jagged line represents photon radiation. Oxidation of two molecules of water requires removal of four electrons. Absorption of each photon results in the transfer of only one electron. So the oxygen evolving complex must oxidize four times in a row to form two dioxygen molecules. The Mn in Mn_4 cluster undergoes five different oxidation states from S_0 to S_4.

radical by a tetranuclear manganese-oxo cluster, the active site for water oxidation, involve coupled electron and proton transfers [33].

2.3.2 Proton transfer theory

To achieve biological energy conversion, membrane-spanning protein assemblies use the energy provided by photochemical or redox reactions to pump protons against the electrochemical gradient, which in turn creates the energy to drive ATP synthesis. To understand the mechanism of proton pumping, a high level of detail is needed. In addition to knowing the driving forces behind proton movement in enzymes, the structure and function of proton translocation pathways must also be elucidated. Cytochrome *c* oxidase (C*c*O) is a bioenergetic enzyme that functions as a proton pump, driven by reducing oxygen to water. While advances in understanding proton transfer in C*c*O have been greatly aided by a number of crystal structures, along with site-directed mutagenesis, the functional and structural complexity of C*c*O presents a formidable obstacle to understanding how, when and where protons move through the protein. Therefore, studies on simpler, well-understood systems could provide us with some insights into how protons are taken up and released from the protein.

More so than electron transfer, proton transfer is extremely dependent on the distance. Since tunneling is inversely proportional to the mass, m½, the distance over which a proton can tunnel is less than a covalent bond length. For example, long-range electron transfers (over 10-20 Å) are commonly found in biological systems with competent rates, whereas the range for proton transfer is restricted to less than 1 Å. To

achieve a long-distance transfer, protons appear to move via hydrogen-bonded chains formed by water and amino acid residues within the protein.

Proton transfer is achieved, presumably, via a hopping mechanism that is similar to the relay theory proposed by Grotthuss[34] 200 years ago. The remarkable thing about the Grotthuss mechanism is that it was proposed prior to the understanding of atomic theory, and at that time, the composition of water was not determined. In modern molecular terms, the Grotthuss mechanism can be summarized as a "hop-and-turn" mechanism (**Fig.1.10**) involving the chemical exchange of hydrogen nuclei along successive hydrogen-bond donor and acceptor groups, sometimes involving an extensive network, followed by the reorientation of these water bonded networks. The true significance of the mechanism was not appreciated until quantum mechanics was developed and ions could be described in more detail. Grotthuss's theory and later Onsager's theory [35] of fast proton transport along hydrogen-bonded chains were further developed into a proton wire theory by Nagle and Morowitz, when they revolutionarily applied it to proton transfer in proteins[36]. Proton wires are thought to be important mechanisms to account for the fast conductance of protons along chains of hydrogen-bonded protonable groups in biological systems.

Redox-driven proton transfer in proteins can be considered to occur by two general mechanisms: a direct mechanism or an indirect mechanism or a combination of both. A direct mechanism is one where proton movement depends on the protonation/deprotonation of the redox center involved, in response to a change in

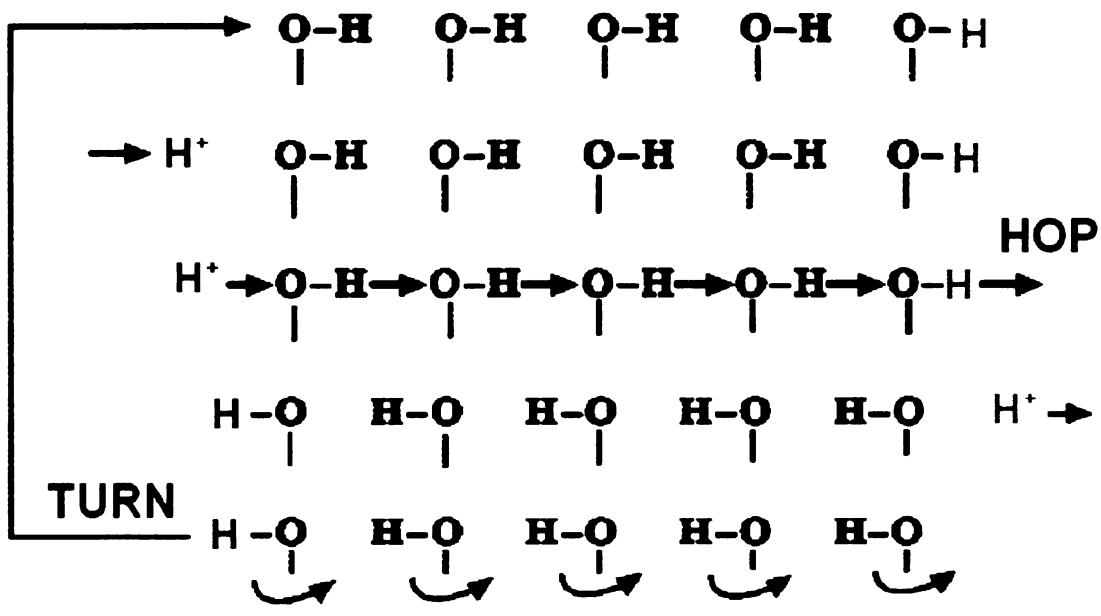

Figure1.10: Schematic depiction of the hop-and-turn mechanism for proton transfer through a hydrogen-bonded water chain. Protons (blue) approaching an oriented hydrogen-bonded water chain can hydrogen bond to the terminal water. The extra charge now on the water can be released as the terminal proton (red) on the other side, effectively transferring a charge across the chain. In order to accept another proton from the same side, a turn step is required. The figure is a modification of a figure from Pomes, R. et al. [37]

oxidation state. An indirect mechanism can be characterized as one where proton uptake and release occur through conformational changes, leading to p*Ka* changes at a distance from the redox center.

A good example of a direct mechanism is demonstrated in the Mitchell hypothesis, as seen in the Q-cycle in cytochrome bc_1 of the respiratory chain[38]. When quinone is reduced to quinol, it is required to take up two protons; if the reduction (and proton uptake) on one side of the membrane is followed by oxidation and deprotonation on the opposite side, the vectorial proton transfer is accomplished.

The classical example of an indirect mechanism is the Bohr effect in hemoglobin. When oxygen binds to the heme, the protein undergoes a conformational change in its structure, leading to a change in p*Ka* of the participating residue at a distance from the heme and release of a proton. Conversely, the acid pH in tissues causes protonation of a key histidine and a conformational change, favoring unloading of the O_2 from the heme.

A combination of both direct and indirect mechanisms are used by some proton pumping proteins such as bacteriorhodopsin (BR)[39]. In BR, light absorption drives the conversion of retinal from all-trans to 13-cis (**Fig.1.11**). This conversion leads to the deprotonation of its Schiff base and protonation of an aspartate (D85). D85 is connected to a glutamate (E204) near the protein surface through water molecules and an arginine. This connectivity leads to the cooperative p*Ka* change between D85 and E204; when D85 is protonated, E204 releases one proton to the extracellular side. To reprotonate the Schiff

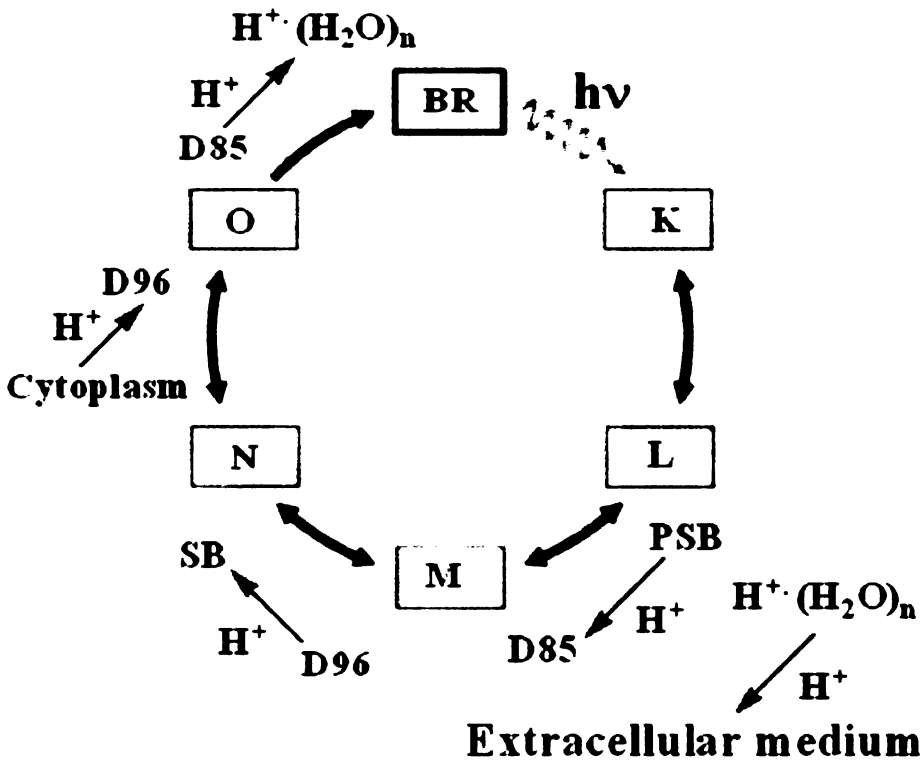

Figure1.11: Photocycle scheme showing the main steps in light-driven proton transport in bacteriorhodopsin. BR, ground state bacteriorhodopsin; PSB, protonated Schiff base. The absorption of light hν induces an all-*trans* to 13-*cis* isomerization of retinal and leads to a metastable protein state termed the K intermediate. L, M, N, and O are all transition intermediates during the proton transfer. The figure is from Garczarek, F. et al.[40].

base, another conformational change takes place, creating a hydrogen-bonded pathway from the inside. Protonation of the Schiff base returns the retinal to its initial all-trans resting state, finishing the cycle. By using both direct and indirect mechanisms during its cycle, bacteriorhodopsin achieves proton translocation.

2.3.3 Proton transfer in C*c*O

The catalytic center of C*c*O is buried deeply within the protein and is situated about 30Å from the internal bulk aqueous phase where substrate protons are taken up to form water at the active site. To effectively deliver the substrate protons to the active site, the enzyme must have a proton-delivering path. Mutation studies [41-45] and X-ray crystallography results [3, 46] have established two pathways by which protons are transferred into the protein: the D and K pathways (**Fig.1.12**). The D and K pathways are named after two key conserved amino acids, aspartate (D132) and lysine (K362). The D channel starts at D132, and continues through a hydrogen-bonded network consisting of approximately ten ordered water molecules and polar residues, to another highly conserved amino acid E286 which is about 24Å from D132. The K channel contains two important residues E101 and K362 as well as T359 and Y288. Depending on the steps in the catalytic cycle, the protons can be delivered via either the D- or the K-channel. Mutation studies showed that the K channel is essential for providing substrate protons to make water[47]. The D channel supplies protons for both water formation and for the pumped protons ($1H^+/e^-$). The uni-directional proton transfer could be achieved by either conformational changes of the E286 side chain during turnover or by changes in water chain structure.

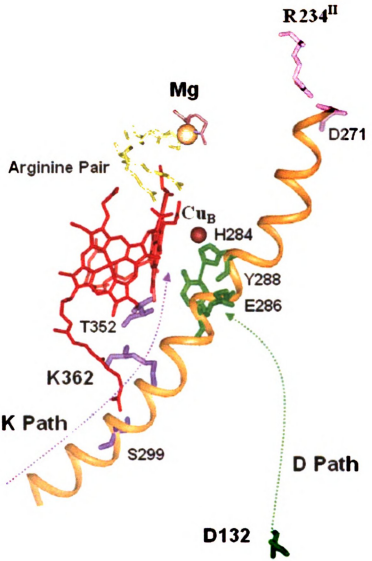

Figure1.12: Key amino acid residues in well-defined D and K proton uptake pathways in *Rs.Cc*O structure. The metal centers are represented by different colorful spheres: organge, dinuclear Cu_A; purple, Mg; green, Cu_B. Heme *a* and heme a_3 are green and brown color-labeled. D pathway is indicated as red dashed line and K pathway is as blue dashed line. The figure is a modification of figure from Mills, D. et al.[48].

High-resolution crystal structures greatly facilitate our understanding of C*c*O at a molecular level, however, the stationary snapshots of the protein structure cannot provide any dynamic information. The mechanism of proton pumping and how this is coupled to electron transfer remains controversial, particularly regarding the proton exit routes. Close examination of the crystal structures, however, reveals a hydrophilic region located at the interface between subunits I and II. Previous work done by Florens et al suggested that the Mn/Mg site was part of the water exit channel and/or involved in a proton exit pathway [14]. A systematic mutagenesis study of amino acids R481/482 (*Rs.*) in this region, which interact with the D ring of the propionates of both hemes, suggested that these arginines might be part of a proton exit or backflow channel[49]. Yoshikawa proposed E51 as a proton release group that is part of the proton exit pathway on the basis of the bovine crystal structure[46]. Electrostatic calculations were employed to examine the possible proton exits by evaluating the electrostatic potential, energies, and protonation state of bovine C*c*O for different redox states of the enzyme (**Fig.1.13**). The results indicate that K171B/D173B in bovine (R408 and K227B in *Rs.*C*c*O) form the most likely proton exit pathway[50]. This has not yet been resolved as there are considerable differences in the *Rs.* and bovine oxidases in this region above the hemes.

2.4 Water channels in proteins

The ubiquitous nature of water in living systems could lead one to think that water channels are not necessary in proteins. Indeed, both experimental and computational data show that even the most hydrophobic regions of proteins are accessible to water molecules [51]. However, the control of water movement in some proteins is necessary and

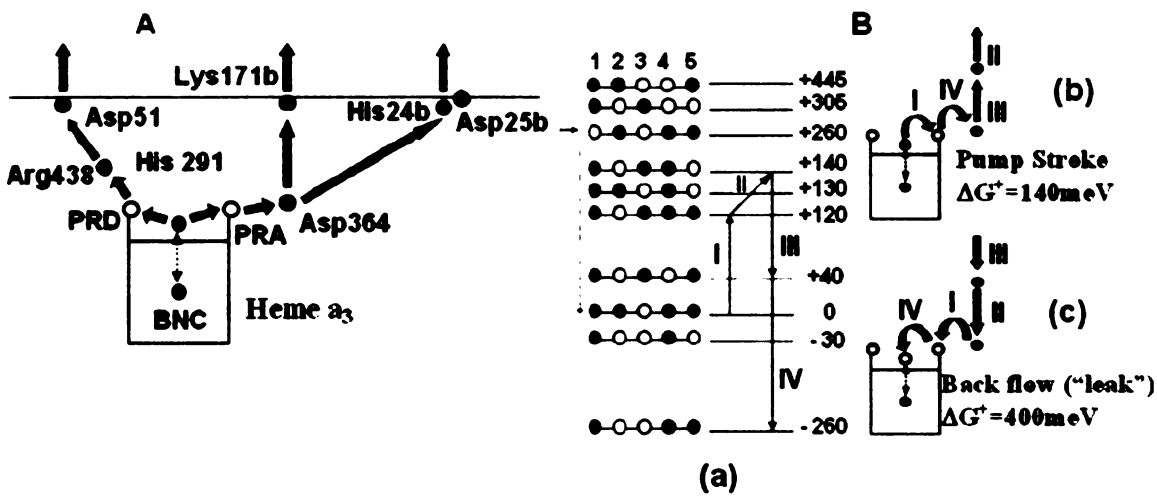

Figure1.13: (A) The most possible proton exit pathways in bovine C*c*O and the energy diagram. (B) Lysine171B proton pathway. (a) Energy diagram of different protonation states of key residues of the binuclear center (BNC). (b) Sequence of proton transfer steps in the pump stroke. (c) Sequence of proton transfer steps leading to the backflow. The numbers represent: 1, BNC; 2, His291; 3, PRA a_3; 4, Asp364; Lys171b. In both cases, energy barriers are evaluated. The full or empty circles represent protonated or deprotonated sites. The figure is a modification of figures from Popovic, D. et al.[50].

important. It is likely that specific mechanisms for water transport occur in many organelles. Since the first water channel, aquaporin, was discovered in 1992, research on aquaporins has been a rapidly developing field. Aquaporins are crucial for life and they are found in all organisms, from bacteria to plants to human. Aquaporins facilitate rapid, highly selective water transport, thus allowing the cell to regulate its volume and internal osmotic pressure according to hydrostatic and/or osmotic pressure differences across the cell membrane. The particularly remarkable thing about aquaporins is that the selectivity of aquaporin water channels is so high that even protons cannot pass. The discovery of aquaporin-1 (AQP-1) was serendipitous and occurred during studies of red cell Rh blood group antigens, but turned out to be an important chapter in water channel studies [52]. Since AQP-1 was discovered, ten more aquaporins in this family were identified. So far, the best understood members of this family are AQP-1 and the bacterial channel protein aquaglyceroporin, Glp-F, which preferentially transfers glycerol[53].

Before crystal structures of AQP-1 [54] and Glp-F [53] were reported, little was known about the origin of water selectivity. Both of these proteins are made up of six transmembrane α-helical domains arranged in a right-handed bundle, with the amino and the carboxyl termini located on the cytoplasmic surface of the membrane. The amino and carboxyl halves of the sequence show similarity to each other, in what appears to be a tandem repeat (**Fig.1.14**). There are also five interhelical loop regions (A – E) that form the extracellular and cytoplasmic vestibules. Loops B and E are hydrophobic loops which

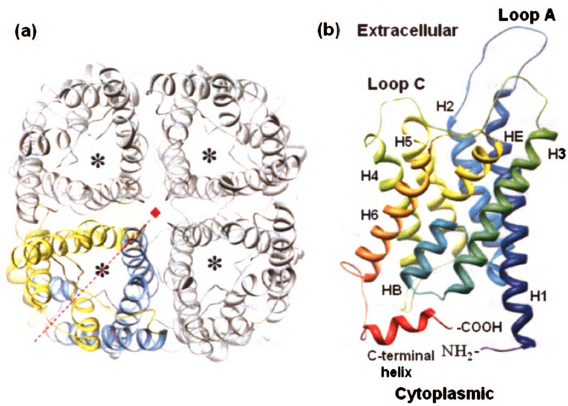

Figure1.14: X-ray crystal structure of AQP1. (a) AQP1 tetramer viewed from the extracellular surface. Blue part in one monomer representing the N-terminal and yellow part representing the C-terminal tandem repeat. The red dashed line indicates the pseudo-2-fold axis relating the two halves of the monomer, and the red square indicates the 4-fold axis of the tetramer. The asterisks indicate the water pore in each of the four subunits. (b) AQP1 monomer viewed in the direction parallel to the membrane. Membrane-spanning helices are denoted as H1–H6, loops are denoted as A–E, and the two pore helices formed by loops B and E as HB and HE, respectively. The figure is a figure from Walz, T. et al. [55]

contain the signature motif Asn-Pro-Ala (NPA), and these two loops overlap in the middle of the lipid bilayer of the membrane, forming a 3-D 'hourglass' structure where the water flows through. This overlap forms one of the two well-known channel constriction sites in the peptide, the NPA motif and a second and usually narrower constriction known as the "selectivity filter". The crystal structures of aquaporins explain how aquaporin allows water to permeate while excluding other cations. Through a combination of channel sterics and solute binding sites, AQP1 facilitates the rapid and highly selective throughput of water.The steric limit of ~2.8 Å is established at the constriction region, and the chemical properties of the residues forming this structure provide additional criteria for solute selection. Different aquaporins have different peptide sequences, which allows for the size of the pore in the protein to differ between aquaporins. The resultant size of the pore directly affects what molecules are able to pass through the pore, with small pore sizes only allowing small molecules like water to pass through the pore while excluding ions such as H^+or K^+.

In C*c*O, both protons and waters are transferred through the protein, but these two processes may take place in separate channels. However, water is produced at the active site and it has been suggested that it may exit close to the Mg/Mn site, exiting at the interface of the subunits I/II/III. The pumped protons may exit through the same path, or via a different path. The selective mechanism for water transport in C*c*O via the Mg/Mn site may be similar to aquaporin and may prevent the flow of protons in this region. A proposed water channel was studied in C*c*O by rapid-freeze quench-EPR (ESEEM) in the laboratory of Ferguson-Miller. The studies showed that bulk water can exchange quickly

within the region near the Mg/Mn site and suggest that water exits the protein via a discrete pathway, not by random diffusion [8].

Water channels are not necessarily static. Members of the cytochrome P450 family catalyze mono-oxidation of a wide variety of endogeneous or xenobiotic compounds. The typical reaction involves the insertion of one atom of oxygen into an organic substrate (RH) while the other oxygen atom is reduced to water. The exclusion of water from the active site has been shown to be essential for efficient enzymatic function[56]. Oprea et al. proposed a two-state model in which a conserved arginine undergoes a conformational change from the initial stable state to another metastable state[57]. In the new state, a new functional water channel is formed. This water cluster communicates with the surface in the closed state and is partially replaced by the flipping arginine side chain in the open state, allowing water molecules to exit to the surface or to reaccess the active site (**Fig.1.15**).

2.5 Questions to be addressed

Although considerable progress has been made on understanding the mechanism of C*c*O, with the help of high-resolution crystal structures, mutations, and kinetic analysis, the mechanism of coupling between proton translocation and electron transfer has not yet been resolved and many fundamental questions regarding regulation of activity and efficiency remain to be addressed. In my thesis, some efforts are made to try to understand the following aspects: the proton coupled electron transfer events in some

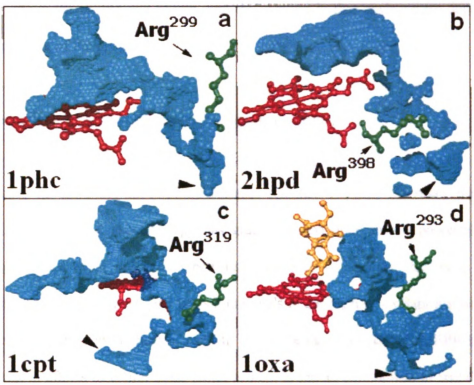

Figure1.15: Snapshots of four representative P450 structures (1phc, 1cpt, 2hpd, and 1oxa) in which cavities forming the aqueduct can be observed. The grid points comprising the cavities are shown in blue. Black arrowheads indicate where the cavities reach the protein surface. The substrate-access channel is not shown. (*a*) In P450cam (1phc), rotation of the R299 side chain opens a wide channel directly connecting the substrate cavity to the protein surface. (*b*) In the R398-modified P450BM3 (2hpd), the substrate cavity extends into the region previously occupied by water. However, the guanidinium group of the rotated R398 blocks a direct path from the substrate cavity to the protein exterior. (*c*) In P450terp, substrate and solvent cavities are only connected if the probe radius is reduced to 0.82 Å in the cavity calculations (purple). Dynamic fluctuations are expected to widen the narrow channel formed between W317 and T103, which separate the two cavities. The second cavity, extending to the left, does not connect with the surface. (*d*) In P450eryF (1oxa), the solvent channel extends from the substrate cavity to the surface, with the narrowest part between the heme propionate A and T291. The figure is the figure from Oprea, T. et al.[57]

site-directed mutants in the vicinity of heme *a*, the proton/water environment of the Mg/Mn site in the proton exit region, and the changes in that environment depending on the redox state of the protein.

3. Introduction of Electron Paramagnetic Resonance (EPR)

Since its discovery in 1944 by Russian scientist Yevgeny Zavoisky from Kazan State University, EPR spectroscopy has gradually developed into a powerful tool for studying species with unpaired electrons. Examples of centers that have unpaired electrons are organic radicals and transition metals in appropriate oxidation states such as Cu^{2+}, low spin ferric ion in hemes, and Mn^{2+}. For the past three decades, EPR has been a major tool in efforts to characterize metal centers in model compounds or metalloenzyme active sites in bioinorganic chemistry and biology. By analyzing hyperfine-coupling interactions between the electron spin and the nuclear spin associated with either the ligands or the nearby nuclei, valuable information regarding the composition, structure, and bonding of paramagnetic centers in proteins can be gained. The application of this technique is the major focus of this thesis, and therefore a more detailed account of the underlying theory will be explored.

Every electron has a magnetic moment and this makes every electron behave like a tiny bar magnet. The spin does not contribute to the overall energy of a system when the external magnetic field is absent, resulting in a degeneracy of energy levels. However, this degeneracy can be broken when an external magnetic field with strength $\mathbf{B_0}$ is

applied. It will have the lowest energy state when the magnetic moment of the electron, μ, is aligned with the magnetic field and a highest energy state when μ is aligned against the magnetic field. The magnetic energy is given by the expression: $E = -\mu H\cos\theta$ where E is the magnetic energy, μ is the magnitude of magnetic dipole moment, H is the magnitude of the magnetic field, and θ is the angle between the magnetic moment and the external field. The two states are labeled by the projection of the electron spin M_S, on the direction of the magnetic field. Because the electron is a spin ½ particle, the parallel state is designated as $E = g_e\mu_B B_0$ where g_e is so-called "g factor" and μ_B is the electron Bohr magneton. This equation implies that the energy difference is directly proportional to the strength of the magnetic field, as shown in the diagram below (**Fig1.16**). The absorption or emission of electromagnetic radiation of energy = $h\nu$ causes a transition of unpaired electron between two energy levels. When combining $\varepsilon = h\nu$ and $\Delta E = g_e\mu_B B_0$, the fundamental equation of EPR spectroscopy $h\nu = g_e\mu_B B_0$ is obtained. From the equation, we can see two possible alternative instrumental configurations. We can apply a constant magnetic field and scan the frequency of the electromagnetic radiation as in conventional spectroscopy. Alternatively, we can keep the electromagnetic radiation frequency constant and scan the magnetic field. A peak in the absorption will occur when the magnetic field tunes the two spin states, so that their energy difference matches the energy of the radiation. This field is called the field for resonance. To solve sensitivity issues in an EPR experiment, commercial instruments often have the frequency fixed while scanning the magnetic field.

EPR has two categories: continuous-wave (cw) EPR and pulse EPR. In cw EPR,

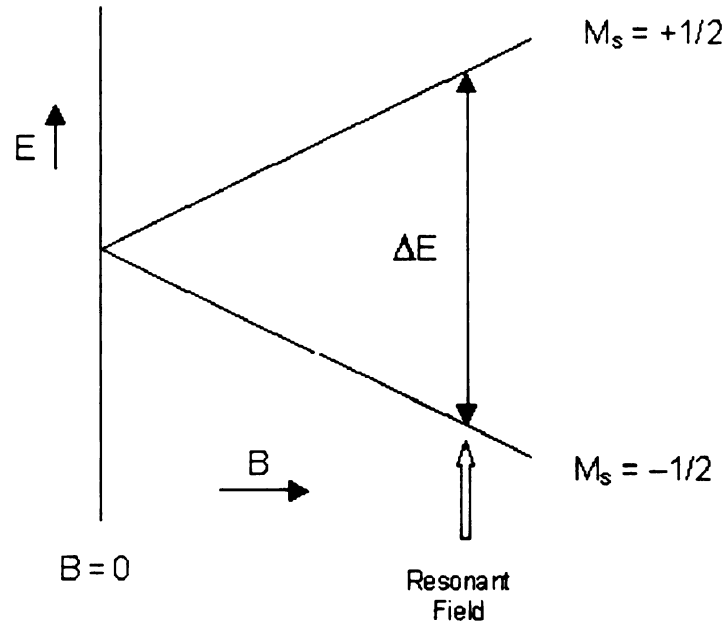

Figure1.16: EPR energy diagram for S=1/2 system. As the external magnetic field is applied to a paramagnetic system with spin S=1/2, the degenerate energy levels are lifted and split into two spin manifold M_S= -1/2 and M_S= +1/2. When the resonance condition $\Delta E = h\nu = g\beta B$ is met, the absorption of the microwave radiation occurs. The magnetic field strength at the resonant point is called the resonant field.

molecules are irradiated continuously by low-power microwave radiation; while in pulse EPR, microwaves are applied in very short and high-powered pulses. Most EPR spectrometers are operated at 9GHz (also known as X band), a frequency that provides a compromise between sensitivity and ease of sample handling. Some other frequencies are also used to achieve higher resolution.

Measurement of g-factors can give us some useful information; however, they do not tell us much about the molecular structure of our sample. Fortunately, the unpaired electron, which gives us the EPR spectrum, is very sensitive to its local surroundings. The nuclei of the atoms in a molecule or complex often have a magnetic moment, which produces a local magnetic field at the electron. The magnetic coupling between the electron and nuclear magnetic moments is called the hyperfine interaction. It gives us a wealth of information about our sample, such as the identity and number of atoms involved in a coupling, as well as their distances from the unpaired electron. Two mechanisms by which electrons and nearby nuclei interact are by through-bond interactions and through-space interactions (dipolar interaction). The former applies to the case of isotropic interactions (spectra independent of sample orientation in a magnetic field) and the latter to the case of anisotropic interactions (spectra dependent on sample orientation in a magnetic field). In principle, the hyperfine couplings are manifested in EPR spectra, however, in practice, these couplings cannot be observed directly because of the inhomogeneous broadening of EPR lines in protein samples. Two techniques can reduce these static inhomogeneous broadening contributions and dramatically increase the spectral resolution so that coupling information can be extracted. These are: 1)

electron nuclear double resonance (ENDOR) and 2) electron spin echo envelope modulation (ESEEM). In both methods, the NMR transition frequencies of nuclear spins are monitored through EPR electron spin transitions in an indirect way.

3.1 Electron spin echo envelope modulation (ESEEM) spectroscopy

In the ESEEM experiment, the NMR transitions are observed due to the mixing of the nuclear states within each electron spin manifold. This state mixing is derived from the anisotropic hyperfine coupling and yields non-zero EPR transition probabilities for semi-forbidden ($\Delta m_S = \pm 1$, $\Delta m_I = \pm 1$) and allowed ($\Delta m_S = \pm 1$, $\Delta m_I = 0$) EPR transitions. Because of the constraints placed on ESEEM by the requirements of nuclear state mixing (each energy level must be involved in at least two different microwave transitions) and the microwave pulse bandwidth (the microwave pulse bandwidth needs to be broad enough to cover the spread in frequencies needed to fully excite the "branching"), ESEEM is particularly useful for studying systems with weak hyperfine coupling interactions.

ESEEM is a pulse version of the electron paramagnetic resonance (EPR) technique. It is a powerful tool for measuring spin transitions of nearby nuclei with relatively weak magnetic couplings to electron spins, and is used widely to study the electronic and geometric structure of paramagnetic centers in biological systems. ESEEM is mostly used in determining hyperfine couplings between a paramagnetic center and its ligands, which will help identify the types of interacting ligands, and determine their orientation with regard to the paramagnetic center's magnetic axes. In the ESEEM experiment, electron

spin echoes are generated by applying suitable short and high-power microwave pulses to induce semi-forbidden transitions, in addition to allowed transitions of nuclear spins magnetically coupled to the electron spins. The electron spin echo decay envelope is then measured by plotting the integrated intensity of these echoes as a function of the time, τ. The resulting spectrum shows an overall decay of the electron spin magnetization that is modulated by electron-nuclear hyperfine interactions [58]. Here two ESEEM experiments, two-pulse Hahn echo and the three-pulse stimulated echo, will be discussed in detail. For simplicity, an electron spin of 1/2 and nuclear spin of 1/2 system will be used as the example in this chapter.

For a S=1/2 and I= 1/2 system, the spin Hamiltonian can be expressed with the assumption that the g is isotropic and hyperfine coupling is axial as follows:

$$H/\hbar = \omega_S S_Z + A_{zz} S_Z I_Z + A_{xz} S_Z I_X - \omega_I I_Z \qquad 1.4$$

Where the first term is the electronic Zeeman, the second and third terms are electron-nuclear hyperfine interaction and the last term is the nuclear Zeeman. The Hamiltonian matrix is easily constructed in a general basis set consisting of electron and nuclear spin product states, $|m_S, m_I\rangle$. Diagonalization to yield the eigenvalues and eigenvectors of eqn.1.4 can be carried out independently for the two electron spin manifolds since the only term in the operator that gives rise to off-diagonal matrix elements is that involving I_x (McCracken, John, Encyclopedia of Inorganic Chemistry). The results are summarized in the energy level diagram (**Fig.1.17**).

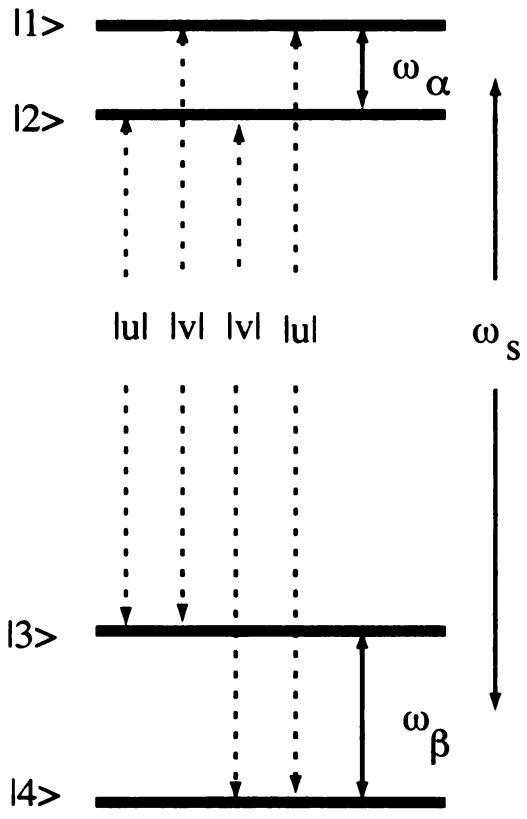

Eigenvectors:

$$|1\rangle = \cos(\varphi_\alpha/2)\,|+\,+\rangle + \sin(\varphi_\alpha/2)\,|+\,-\rangle$$

$$|2\rangle = -\sin(\varphi_\alpha/2)\,|+\,+\rangle + \cos(\varphi_\alpha/2)\,|+\,-\rangle$$

$$|3\rangle = \cos(\varphi_\beta/2)\,|-\,+\rangle + \sin(\varphi_\beta/2)\,|-\,-\rangle$$

$$|4\rangle = -\sin(\varphi_\beta/2)\,|-\,+\rangle + \cos(\varphi_\beta/2)\,|-\,-\rangle$$

$$\omega_\alpha = \sqrt{(\omega_I - A/2)^2 + B^2/4}$$

$$\omega_\beta = \sqrt{(\omega_I + A/2)^2 + B^2/4}$$

Figure1.17: Energy level scheme and eigenvectors for the S=1/2, and I=1/2 system. This figure is a figure courtesy of Dr. John McCracken

The |u| and |v| in **Fig. 1.17** are normalized probability amplitudes for the EPR transitions. The angles, φ_α and φ_β respectively, define the axes of quantization for the α and β electron spin manifolds, and are expressed as $\sin\varphi_\alpha = B/2\omega_\alpha$ and $\sin\varphi_\beta = B/2\omega_\beta$, where ω_α and ω_β are the nuclear transition frequencies. Four EPR transitions are possible between the upper and lower doublets. When microwave pulses are applied to the spin system, the allowed and forbidden transitions are induced with different probabilities determined by the corresponding matrix elements.

Mims [59] derived the originally analytical expression for two-pulse ESEEM function as equation 1.6:

$$E_{mod}(\tau) = 1-k/2\{1-\cos(\omega_\alpha\tau) - \cos(\omega_\beta\tau) + \tfrac{1}{2}\cos[(\omega_\alpha+\omega_\beta)\tau] + \tfrac{1}{2}\cos[(\omega_\alpha-\omega_\beta)\tau]\} \qquad 1.5$$

Where τ is the time interval between the microwave pulses and k is the modulation amplitude factor with the expression: $k= \sin^2(\omega_\alpha-\omega_\beta) = [\omega_I B/(\omega_\alpha\omega_\beta)]^2$ 1.6

The observed ESEEM spectrum is a composition of modulation function and a decay function that describes the loss of magnetization due to spin relaxation. From equation 1.6, we can see that modulations of the two-pulse echo amplitude occur at both fundamental hyperfine frequencies and their sum and difference combination frequencies. The amplitude of the modulations is directly related to the transition probabilities for the two different transitions. In a spin system with multiple nuclei contribute to the modulation of a single paramagnetic center. The modulation function in this instance is given by the expression:

$$E(\tau) = V_{decay}\prod_{i=1}^{N} E^i_{\mathrm{mod}}(\tau) \qquad 1.7$$

where N represents the number of coupled nuclei. In equation 1.7, the observed ESEEM spectrum is the product of contribution from each nucleus, leading to frequencies that are combinations of the frequencies arising from different nuclei. This increased complexity, combined with the lowered resolution due to short phase memory time, makes two-pulse ESEEM analysis a formidable challenge.

Three-pulse ESEEM has the pulse sequence of 90°-τ-90°-T-90° in which two microwave pulses separated by τ are applied, followed by a third pulse after time T, and the stimulated echo is observed at time τ after the third pulse (**Fig.1.18**). Unlike two-pulse ESEEM, no sums and differences of fundamental nuclear frequencies are observed in three-pulse ESEEM spectrum, greatly simplifying the whole spectrum. Moreover, the short phase memory time limitations associated with two-pulse ESEEM are largely alleviated in three-pulse experiments, therefore, the modulation echo envelope stays longer, resulting in narrower lines in the spectrum. For a typical three-pulse measurement, τ is fixed to a value shorter than the spin-spin relaxation time of the electron spin center, and the interval (T) between the second and third microwave pulses ranging from 40 ns to ~ 10 μs is scanned. For the specific case of the Mn(II) site in C*c*O, τ was set to 204 ns and T was stepped in 16 ns increments from 40 ns to > 8 μs.

For a three-pulse ESEEM, the analytical expression for a S=1/2, I=1/2 system is given in equation 1.8:

$$E_{mod}(\tau, T) = 1-k/4\{[1-\cos(\omega_\alpha\tau)][1-\cos\omega_\beta T)]+[\ 1-\cos(\omega_\beta\tau)][1-\cos\omega_\alpha T)]\} \qquad 1.8$$

The equation shows that three-pulse ESEEM has a simpler form, in that there are only lines from fundamental nuclear frequencies. The equation also shows that the modulation is affected by the τ value. If carefully chosen, different τ values can either enhance or suppress certain ESEEM signals from contributions of different nuclei. This τ-suppression effect is very useful in making spectral assignments.

3.2 Electron nuclear double resonance (ENDOR) spectroscopy

ENDOR is another pulse EPR technique in which the ENDOR spectrum is obtained by recording the echo intensity as a function of the frequency of the RF pulse. A change in the echo amplitude occurs when the RF is on resonance with a NMR transition, therefore, generating an ENDOR signal. There are many ways to run pulse ENDOR. Mims ENDOR [60] and Davies ENDOR [61] are the most frequently employed methods so far. Davies ENDOR is a selective method and is suitable for systems with medium to large hyperfine couplings (A>2MHz). Mims ENDOR, on the other hand, is nonselective and most efficient for systems with small hyperfine couplings (A<2MHz) but suffers blind spots. If carefully chosen, proper τ values can place blind spots well outside the ENDOR spectrum. Generally speaking, Davies ENDOR is a better way to record ^{1}H while Mims is best for ^{2}H. Davies ENDOR is employed in the projects in this thesis and will be given more space for discussion.

Fig.1.19 shows a schematic description of the Davies ENDOR sequence and the evolution of spin state populations during a Davies ENDOR pulse sequence. "In the

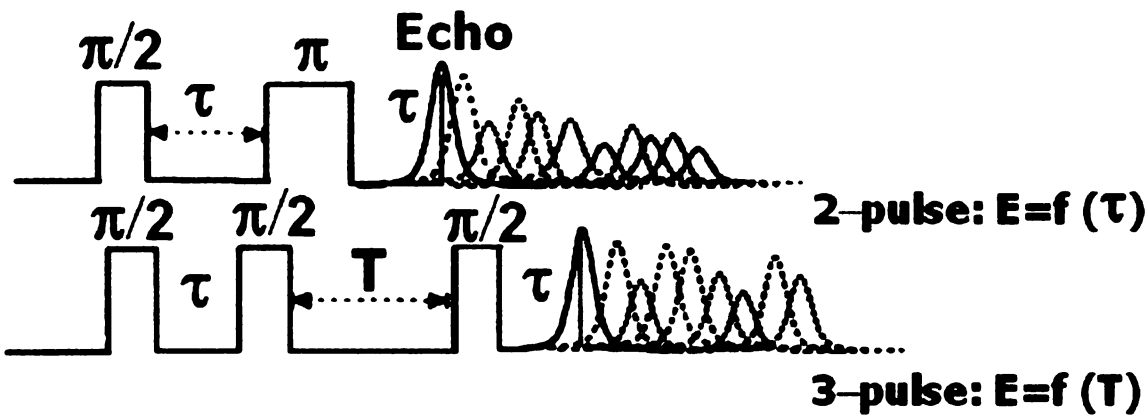

Figure1.18: The diagram of pulse sequence for two- and three- pulse ESEEM experiments. In the two-pulse experiment at time τ after the second pulse, a spin echo is formed. The modulation envelope is obtained as τ is incremented. In the three-pulse sequence, two pulses separated by τ are applied, followed by a third pulse after time T, and the stimulated echo is observed at time τ after the third pulse. The modulation envelope is obtained as T is incremented. The figure is a modulation of the figure from Deligiannakis, Y. et al. [62]

preparation step of the pulse sequence, a selective microwave π pulse is applied to one of the electron spin transitions to transfer the initial thermal polarization of the electron spin to the nuclear spin polarization. In the mixing step, a single RF pulse is applied, when the RF frequency matches the frequency of one of the polarized NMR transitions for a nucleus that is hyperfine coupled to an electron, nuclear spin polarization is transferred between nuclear levels. This transfer of nuclear spin polarization also changes the electron spin polarization of those electron spin states connected by the EPR transition in the preparation period, which can be detected using a two-pulse (Hahn) echo pulse sequence. The RF-induced nuclear spin polarization transfer is manifested as a change in the electron spin echo intensity"[63]. For nuclei with different hyperfine couplings, one can vary the width of the microwave pulse to achieve enhancement in amplitude. In general, longer microwave pulse width enhances ENDOR amplitude from nuclei with small hyperfine couplings, while amplitudes from nuclei with large hyperfine couplings can be enhanced by using shorter microwave pulse widths with higher magnetic field strengths.

"ENDOR is a nonlinear phenomenon. Intensities of ENDOR can be markedly altered by, not only the calculable effects, such as spin concentration, but also by spin relaxation, by the degree of EPR and RF power saturation, and the size of holes burned by the microwave pulse"[63]. So ENDOR is not suitable for quantification, but is useful in providing hyperfine-coupling interactions between the paramagnetic center and its surrounding nuclei. Obtaining hyperfine-coupling constants using the ENDOR method is very common.

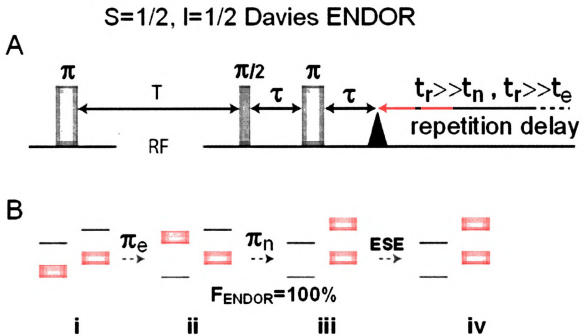

Figure1.19: A) Davies ENDOR pulse sequence, B) Evolution of spin state population during the Davies ENDOR pulse sequence. Electron (π_e) and nuclear (π_n) spin transitions excited by selective microwave and RF pulses, respectively. State populations are shown using colored bars. The figure is a modification of a figure from Tyryshkin, A. et al. [64]

4. Conclusion:

Progress has been made in the study of C*c*O for the past three decades, but many questions still have to be addressed. Proton transfer and electron transfer during protein turnover and how these processes are coupled, are still not well understood. In this thesis, the author attempts to understand the enzyme from the following perspectives:

Previous work indicates that electron transfer from heme *a* to the binuclear center depends on a protonation event and the reaction is limited by the proton transfer [65-68]. It was also found that electron transfer from Cu_A to heme *a* is also coupled to proton transfer[69-73]. Studies on the dependence of electron transfer from Cu_A to heme *a* on proton transfer has led to conflicting results in the literature. In the second chapter, a series of mutants at position 44, close to heme *a*, were studied by EPR, fast kinetics, and electrochemistry methods in a systematic way with the hope of shedding some new light on proton coupled electron transfer reaction associated with this site.

Proton movement pathways in C*c*O are of great importance in trying to understand the mechanisms of proton translocation across the membrane. Crystal structures of C*c*O have enhanced our understanding of likely proton uptake and exit pathways. However, the dynamics, or motions, of the protein cannot easily be observed in a static crystal structure. Additionally, the resolution of the crystal structure is usually not good enough to determine the placement of protons, but EPR is a complementary technique in this regard. Previous studies, using the Mn-substituted enzyme and rapid freeze quench coupled EPR, provided some intriguing results on possible proton/water exit(s)[8, 14]. In

chapters three and four, ENDOR and ESEEM studies of Mn-substituted C*c*O are described in detail, following up on the previous work to better define the dynamics of water and other ligands in this critical region.

High field cw EPR was also performed to study the enzyme at different oxidation states in the presence of deuterium or ^{17}O-labeled water, utilizing the strong Mn^{2+} signal. Some unexpected disappointing results were explained and several factors explaining the findings were also found. In the future, high-field EPR could be very useful as it has the potential to facilitate our understanding of C*c*O.

REFERENCES:

1. Bushnell, G. W.; Louie, G. V.; Brayer, G. D., High-resolution three-dimensional structure of horse heart cytochrome c. *J Mol Biol* **1990,** 214, (2), 585-95.

2. Iverson, T. M.; Luna-Chavez, C.; Cecchini, G.; Rees, D. C., Structure of the Escherichia coli fumarate reductase respiratory complex. *Science* **1999,** 284, (5422), 1961-6.

3. Iwata, S.; Ostermeier, C.; Ludwig, B.; Michel, H., Structure at 2.8 Å resolution of cytochrome c oxidase from *Paracoccus denitrificans*. *Nature* **1995,** 376, 660-669.

4. Svensson-Ek, M.; Abramson, J.; Larsson, G.; Tornoth, S.; Brzezinski, P.; Iwata, S., The X-ray crystal structures of wild-type and EQ(I-286) mutant cytochrome c oxidases from *Rhodobacter sphaeroides*. *J. Mol. Biol.* **2002,** 321, 329-339.

5. MacMunn, C. A., Researches on myohaematin and the histohaematins. *Philosophical Transactions of the Royal Society of London. Series B: Biological Sciences* **1886,** 177, 267-298.

6. Keilin, D.; Hartree, E. F., Cytochrome and cytochrome oxidase. *Proceedings of the Royal Society of London. Series B: Biological Sciences* **1939,** 127, 167-191.

7. Ferguson-Miller, S.; Babcock, G., Heme/Copper Terminal Oxidases. *Chemical Reviews* **1996,** 96, (7), 2889-2907.

8. Schmidt, B.; McCracken, J.; Ferguson-Miller, S., A discrete water exit pathway in the membrane protein cytochrome c oxidase. *Proc Natl Acad Sci U S A* **2003,** 100, (26), 15539-42.

9. Tsukihara, T.; Aoyama, H.; Yamashita, E.; Tomizaki, T.; Yamaguchi, H.; Shinzawa-itoh, K.; Nakashima, R.; Yaono, R.; Yoshikawa, S., Structure of Metal Sites of Oxidized Bovine Heart cytochrome c Oxidase at 2.8 Å. *Science* **1995,** 269, 1069-1074.

10. Qin, L.; Hiser, C.; Mulichak, A.; Garavito, R. M.; Ferguson-Miller, S., Identification of conserved lipid/detergent-binding sites in a high-resolution structure of the membrane protein cytochrome c oxidase. *Proc Natl Acad Sci U S A* **2006,** 103, (44), 16117-22.

11. Hosler, J. P.; Fetter, J.; Tecklenburg, M. M. J.; Espe, M.; Lerma, C.; Ferguson-Miller, S., Cytochrome aa_3 of *Rhodobacter sphaeroides* as a Model for Mitochondrial Cytochrome *c* Oxidase. *J. Biol. Chem.* **1992,** 267, (34), 24264-24272.

12. Hosler, J. P.; Ferguson-Miller, S.; Mills, D. A., Energy Transduction: Proton Transfer Through the Respiratory Complexes. *Annu Rev Biochem* **2006.**

13. Tsukihara, T.; Aoyama, H.; Yamashita, E.; Tomizaki, T.; Yamaguchi, H.; Shinzawa-Itoh, K.; Nakashima, R.; Yaono, R.; Yoshikawa, S., The Whole Structure of the 13-Subunit Oxidized Cytochrome c Oxidase at 2.8 Å. *Science* **1996,** 272, 1136-1144.

14. Florens, L.; Schmidt, B.; McCracken, J.; Ferguson-Miller, S., Fast deuterium access to the buried magnesium/manganese site in cytochrome c oxidase. *Biochemistry* **2001,** 40, (25), 7491-7497.

15. Marcus, R. A.; Sutin, N., Electron transfers in chemistry and biology. *Biochim. Biophys. Acta* **1985,** 811, 265-322.

16. Simonson, T., Gaussian fluctuations and linear response in an electron transfer protein. *Proceedings of the National Academy of Sciences of the United States of America* **2002,** 99, (10), 6544-6549.

17. Gray, H. B.; Malmstrom, B. G.; Williams, R. J. P., Copper coordination in blue proteins. *Journal of Biological Inorganic Chemistry* **2000,** 5, (5), 551-559.

18. Winkler, J. R.; WittungStafshede, P.; Leckner, J.; Malmstrom, B. G.; Gray, H. B., Effects of folding on metalloprotein active sites. *Proceedings of the National Academy of Sciences of the United States of America* **1997,** 94, (9), 4246-4249.

19. Hopfield, J. J., Electron-Transfer between Biological Molecules by Thermally Activated Tunneling. *Proceedings of the National Academy of Sciences of the United States of America* **1974,** 71, (9), 3640-3644.

20. Mcconnell, H., Intramolecular Charge Transfer in Aromatic Free Radicals. *Journal of Chemical Physics* **1961,** 35, (2), 508-&.

21. Davis, W. B.; Svec, W. A.; Ratner, M. A.; Wasielewski, M. R., Molecular-wire behaviour in p-phenylenevinylene oligomers. *Nature* **1998,** 396, (6706), 60-63.

22. Witt, H.; Zickermann, V.; Ludwig, B., Site-directed mutagenesis of cytochrome c oxidase reveals two acidic residues involved in the binding of cytochrome c. *Biochim Biophys Acta* **1995,** 1230, (1-2), 74-6.

23. Geren, L. M.; Beasley, J. R.; Fine, B. R.; Saunders, A. J.; Hibdon, S.; Pielak, G. J.; Durham, B.; Millett, F., Design of a Ruthenium-Cytochrome c Derivative to Measure Electron Transfer to the Initial Acceptor in Cytochrome c oxidase. *J. Biol. Chem.* **1995,** 270, 2466 - 2662.

24. Ramirez, B. E.; Malmstrom, B. G.; Winkler, J. R.; Gray, H. B., The currents of life: The terminal electron-transfer complex of respiration. *Proc. Natl. Acad. Sci. USA* **1995,** 92, 11949 - 11951.

25. Regan, J. J.; Ramirez, B. E.; Winkler, J. R.; Gray, H. B.; Malmstrom, B. G., Pathways for electron tunneling in cytochrome c oxidase. *Journal of Bioenergetics and Biomembranes* **1998,** 30, (1), 35-39.

26. Gamelin, D. R.; Randall, D. W.; Hay, M. T.; Houser, R. P.; Mulder, T. C.; Canters, G. W.; de Vries, S.; Tolman, W. B.; Lu, Y.; Solomon, E. I., Spectroscopy of mixed-valence Cu_A-type centers: Ligand-field control of ground-state properties related to electron transfer. *J. Am. Chem. Soc.* **1998,** 120, 5246-5263.

27. George, S. D.; Metz, M.; Szilagyi, R. K.; Wang, H. X.; Cramer, S. P.; Lu, Y.; Tolman, W. B.; Hedman, B.; Hodgson, K. O.; Solomon, E. I., A quantitative description of the ground-state wave function of Cu-A by X-ray absorption spectroscopy: Comparison to plastocyanin and relevance to electron transfer. *Journal of the American Chemical Society* **2001,** 123, (24), 5757-5767.

28. Medvedev, D. M.; Daizadeh, I.; Stuchebrukhov, A. A., Electron transfer tunneling pathways in bovine heart cytochrome c oxidase. *Journal of the American Chemical Society* **2000,** 122, (28), 6571-6582.

29. Liu, W. T.; Thorp, H. H., Photoinduced Proton-Transfer between Transdioxorhenium(V) and Metal-Hydrides - a Convenient Method for Determining Kinetic Acidities. *Abstracts of Papers of the American Chemical Society* **1995,** 210, 168-INOR.

30. Cukier, R. I., Mechanism for Proton-Coupled Electron-Transfer Reactions. *Journal of Physical Chemistry* **1994,** 98, (9), 2377-2381.

31. Cukier, R. I., Proton-Coupled Electron-Transfer through an Asymmetric Hydrogen-Bended Interface. *Journal of Physical Chemistry* **1995,** 99, (43), 16101-16115.

32. Fang, J. Y.; Hammes-Schiffer, S., Proton-coupled electron transfer reactions in solution: Molecular dynamics with quantum transitions for model systems. *Journal of Chemical Physics* **1997,** 106, (20), 8442-8454.

33. Christen, G.; Renger, G., The role of hydrogen bonds for the multiphasic P680(+center dot) reduction by Y-z in photosystem II with intact oxygen evolution capacity. Analysis of kinetic H/D isotope exchange effects. *Biochemistry* **1999,** 38, (7), 2068-2077.

34. de Grotthuss, C. J. T., Sur la decomposition de l'eau et des corps qu'elle tient en dissolution a l'aide de l'electricite galvanique. *Annales de Chimie (Paris)* **1806,** LVIII, 54-74.

35. Onsager, L., Ion Passages in Lipid Bilayers. *Science* **1967,** 156, (3774), 541-&.

36. Nagle, J. F.; Morowitz, H. J., Molecular Mechanisms for Proton Transport in Membranes. *Proceedings of the National Academy of Sciences of the United States of America* **1978,** 75, 298-302.

37. Pomes, R.; Roux, B., Molecular mechanism of H+ conduction in the single-file water chain of the gramicidin channel. *Biophys J* **2002,** 82, (5), 2304-16.

38. Trumpower, B., A concerted, alternating sites mechanism of ubiquinol oxidation by the dimeric cytochrome bc1 complex. *Biochim. Biophys. Acta* **2002,** 1555, 166-173.

39. Lanyi, J. K.; Luecke, H., Bacteriorhodopsin. *Curr Opin Struct Biol* **2001,** 11, (4), 415-9.

40. Garczarek, F.; Gerwert, K., Functional waters in intraprotein proton transfer monitored by FTIR difference spectroscopy. *Nature* **2006,** 439, (7072), 109-112.

41. Hosler, J. P.; Ferguson-Miller, S.; Calhoun, M. W.; Thomas, J. W.; Hill, J.; Lemieux, L.; Ma, J.; Georgiou, C.; Fetter, J.; Shapleigh, J. P.; Tecklenburg, M. M. J.; Babcock, G. T.; Gennis, R. B., Insight into the Active-Site Structure and Function of Cytochrome Oxidase by Analysis of Site-Directed Mutants of Bacterial Cytochrome aa_3 and Cytochrome *bo*. *J. Bioenerg. Biomembr.* **1993,** 25, 121-136.

42. Hosler, J. P.; Shapleigh, J. P.; Mitchell, D. M.; Kim, Y.; Pressler, M.; Georgiou, C.; Babcock, G. T.; Alben, J. O.; Ferguson-Miller, S.; Gennis, R. B., Polar Residues in Helix VIII of Subunit I of Cytochrome *c* Oxidase Influence the Activity and the Structure of the Active Site. *Biochemistry* **1996,** 35, 10776-10783.

43. Thomas, J. W.; Lemieux, L. J.; Alben, J. O.; Gennis, R. B., Site-directed mutagenesis of highly conserved residues in helix VIII of subunit I of the cytochrome bo ubiquinol oxidase from Escherichia coli: an amphipathic transmembrane helix that may be important in conveying protons to the binuclear center. *Biochemistry* **1993,** 32, (41), 11173-80.

44. Garcia-Horsman, J. A.; Puustinen, A.; Gennis, R. B.; Wikstrom, M., Proton transfer in cytochrome bo3 ubiquinol oxidase of Escherichia coli: second-site mutations in subunit I that restore proton pumping in the mutant Asp135-->Asn. *Biochemistry* **1995,** 34, (13), 4428-33.

45. Fetter, J. R.; Qian, J.; Shapleigh, J.; Thomas, J. W.; García-Horsman, J. A.; Schmidt, E.; Hosler, J.; Babcock, G. T.; Gennis, R. B.; Ferguson-Miller, S., Possible Proton Relay Pathways in Cytochrome *c* Oxidase. *Proc. Nat. Acad. Sci. U. S.A.* **1995,** 92, 1604-1608.

46. Yoshikawa, S.; Shinzawa-Itoh, K.; Nakashima, R.; Yaono, R.; Yamashita, E.; Inoue, N.; Yao, M.; Fei, M. J.; Libeu, C. P.; Mizushima, T.; Yamaguchi, H.; Tomizaki,

T.; Tsukihara, T., Redox-coupled crystal structural changes in bovine heart cytochrome c oxidase. *Science* **1998,** 280, (5370), 1723-9.

47. Mills, D. A.; Florens, L.; Hiser, C.; Qian, J.; Ferguson-Miller, S., Where is "outside" in cytochrome c oxidase and how and when do protons get there? *Biochim. Biophys. Acta* **2000,** 1458, 180-187.

48. Mills, D. A.; Ferguson-Miller, S., Understanding the mechanism of proton movement linked to oxygen reduction in cytochrome c oxidase: lessons from other proteins. *Febs Letters* **2003,** 545, (1), 47-51.

49. Qian, J.; Mills, D. A.; Geren, L.; Wang, K. F.; Hoganson, C. W.; Schmidt, B.; Hiser, C.; Babcock, G. T.; Durham, B.; Millett, F.; Ferguson-Miller, S., Role of the conserved arginine pair in proton and electron transfer in cytochrome c oxidase. *Biochemistry* **2004,** 43, (19), 5748-5756.

50. Popovic, D. M.; Stuchebrukhov, A. A., Proton exit channels in bovine cytochrome c oxidase. *Journal of Physical Chemistry B* **2005,** 109, (5), 1999-2006.

51. Gottschalk, M.; Dencher, N. A.; Halle, B., Microsecond exchange of internal water molecules in bacteriorhodopsin. *Journal of Molecular Biology* **2001,** 311, (3), 605-621.

52. Preston, G. M.; Carroll, T. P.; Guggino, W. B.; Agre, P., Appearance of Water Channels in Xenopus Oocytes Expressing Red-Cell Chip28 Protein. *Science* **1992,** 256, (5055), 385-387.

53. Fu, D.; Libson, A.; Miercke, L. J.; Weitzman, C.; Nollert, P.; Krucinski, J.; Stroud, R. M., Structure of a glycerol-conducting channel and the basis for its selectivity. *Science* **2000,** 290, (5491), 481-6.

54. Sui, H. X.; Han, B. G.; Lee, J. K.; Walian, P.; Jap, B. K., Structural basis of water-specific transport through the AQP1 water channel. *Nature* **2001,** 414, (6866), 872-878.

55. Walz, T. G. a. T., the structure of aquaporins. *quarterly Reviews of Biophysics* **2006,** 39, (4), 361-396.

56. Loida, P. J.; Sligar, S. G., Molecular Recognition in Cytochrome-P-450 - Mechanism for the Control of Uncoupling Reactions. *Biochemistry* **1993,** 32, (43), 11530-11538.

57. Oprea, T. I.; Hummer, G.; Garcia, A. E., Identification of a functional water channel in cytochrome P450 enzymes. *Proc Natl Acad Sci U S A* **1997,** 94, (6), 2133-8.

58. Tsvetkov, S. A. D. a. Y. D., electron spin echo envelope modulation (ESEEM) spectroscopy. **1992.**

59. Mims, W. B., Envelope Modulation in Spin-Echo Experiments. *Physical Review B* **1972,** 5, (7), 2409-&.

60. Mims, W. B., Pulsed Endor Experiments. *Proceedings of the Royal Society of London Series a-Mathematical and Physical Sciences* **1965,** 283, (1395), 452-&.

61. Davies, E. R., New Pulse Endor Technique. *Physics Letters A* **1974,** A 47, (1), 1-2.

62. Deligiannakis, Y.; Louloudi, M.; Hadjiliadis, N., Electron spin echo envelope modulation (ESEEM) spectroscopy as a tool to investigate the coordination environment of metal centers. *Coordination Chemistry Reviews* **2000,** 204, 1-112.

63. Tan, X. L.; Bernardo, M.; Thomann, H.; Scholes, C. P., Pulsed and Continuous Wave Electron Nuclear Double-Resonance Patterns of Aquo Protons Coordinated in Frozen Solution to High-Spin Mn2+. *Journal of Chemical Physics* **1993,** 98, (7), 5147-5157.

64. Tyryshkin, A. M.; Morton, J. J. L.; Ardavan, A.; Lyon, S. A., Davies electron-nuclear double resonance revisited: Enhanced sensitivity and nuclear spin relaxation. *Journal of Chemical Physics* **2006,** 124, (23), -.

65. Branden, M.; Sigurdson, H.; Namslauer, A.; Gennis, R.; Adelroth, P.; Brzezinski, P., On the role of the K-proton transfer pathway in cytochrome c oxidase. *Proceedings of the National Academy of Sciences of the United States of America* **2001,** 98, 5013-5018.

66. Karpefors, M.; Adelroth, P.; Zhen, Y.; Ferguson-Miller, S.; Brzezinski, P., Proton uptake controls electron transfer in cytochrome c oxidase. *Proc Natl Acad Sci U S A* **1998,** 95, (23), 13606-11.

67. Pecoraro, C.; Gennis, R. B.; Vygodina, T. V.; Konstantinov, A. A., Role of the K-channel in the pH-dependence of the reaction of cytochrome c oxidase with hydrogen peroxide. *Biochemistry* **2001,** 40, (32), 9695-708.

68. Moody, A. J.; Rich, P. R., The Effect of pH on Redox Titrations of Haem *a* in Cyanide-Liganded Cytochrome-*c* Oxidase: Experimental and Modelling Studies. *Biochim. Biophys. Acta* **1990,** 1015, 205-215.

69. Babcock, G. T.; Callahan, P. M., Redox-Linked Hydrogen Bond Strength Changes in Cytochrome *a*: Implications for a Cytochrome Oxidase Proton Pump. *Biochemistry* **1983,** 22, 2314-2319.

70. Capitanio, N.; Capitanio, G.; Demarinis, D. A.; De Nitto, E.; Massari, S.; Papa, S., Factors affecting the H+/e- stoichiometry in mitochondrial cytochrome c oxidase: influence of the rate of electron flow and transmembrane delta pH. *Biochemistry* **1996,** 35, (33), 10800-6.

71. Capitanio, N.; Capitanio, G.; Boffoli, D.; Papa, S., The proton/electron coupling ratio at heme a and Cu(A) in bovine heart cytochrome c oxidase. *Biochemistry* **2000,** 39, (50), 15454-61.

72. Capitanio, N.; Capitanio, G.; Minuto, M.; De Nitto, E.; Palese, L. L.; Nicholls, P.; Papa, S., Coupling of electron transfer with proton transfer at heme a and Cu(A) (redox Bohr effects) in cytochrome c oxidase. Studies with the carbon monoxide inhibited enzyme. *Biochemistry* **2000,** 39, (21), 6373-9.

73. Papa, S.; Capitanio, N.; Villani, G., A cooperative model for protonmotive heme-copper oxidases. The role of heme a in the proton pump of cytochrome c oxidase. *FEBS Lett* **1998,** 439, (1-2), 1-8.

CHAPTER 2

CW EPR INVESTIGATIONS OF THE HEME *A* CENTER IN SEVERAL S44 MUTANTS

1.Introduction

Cytochrome *c* oxidase (C*c*O) is the terminal electron acceptor in the respiratory chain in the inner mitochondrial membrane in eukaryotes and in the bacterial cytoplasmic membrane. C*c*O has four redox-active metal centers: heme *a*, heme a_3, the dinuclear copper center (Cu_A), and a type II copper center (Cu_B) which is magnetically coupled with heme a_3. Time-resolved spectroscopies have shown that electrons are transferred from a reduced cytochrome *c* to Cu_A[1-3], from Cu_A to heme *a*, then to the heme a_3/Cu_B binuclear center, where molecular oxygen binds and is reduced to water (**Fig.2.1**). In *Rhodobacter sphaeroides* cytochrome *c* oxidase (*Rs.*C*c*O), His 102 and His 421 are the two axial ligands for heme *a*. Although heme *a* is not involved in the reduction of molecular oxygen to water, it is proposed that heme *a* reduction is linked to redox changes at the binuclear center[4] and probably to the movement of protons. Bacterial C*c*O has a much simpler structure than its mammalian counterpart, but shows a high degree of sequence homology and functional equivalency [5-7], making it a good model system for the more complex mammalian enzyme. Despite the similarities in the bacterial and mammalian oxidase structures, there are some differences. The *Rs.* and *Paracoccus denitrificans (Pd.)* bacterial C*c*Os have steady-state activities of ~1500s^{-1} which are higher than bovine C*c*O does (~400s^{-1}). A red shift in the visible spectrum was also observed in bacterial C*c*O compared to bovine C*c*O[8]. In addition, the redox potential of bovine heme *a* is measured to be more positive, by ~ +13 mV, relative to the *Rs.* heme *a*, assuming similar redox potentials of Cu_A[9].

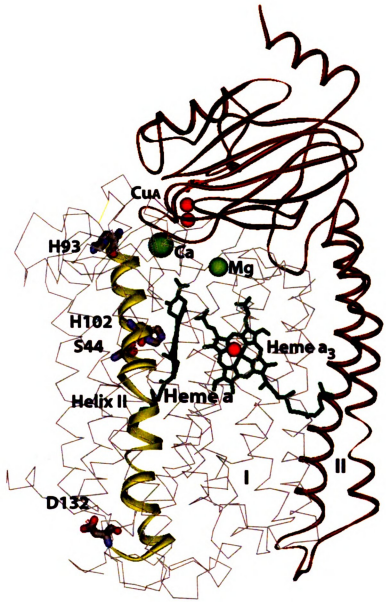

Figure 2.1: The *Rs.* C*c*O crystal structure (PDB ID: 1M56). Subunit I (gray) with the two hemes in light green, Ca and Mg (green spheres) and key residues (stick) of S44, H93, H102 (a ligand of heme *a*), D132 at the entrance of the proton uptake path and helix I (bright yellow) that comprises the residue S44. Subunit II (deep red) is shown with the dinuclear Cu_A (orange spheres). The figure is the courtesy figure from Dr.Mills

The g values of the EPR spectrum of heme *a* in bacterial oxidases are also shifted relative to bovine oxidase, particularly, the g_z peak is 2.82 in *Rs.*C*c*O compared to 3.03 in bovine[8]. It was proposed that the shifted EPR g values in *Rs.*C*c*O were due to an increased anionic character of one or both of the heme *a* histidine axial ligands, possibly due to altered hydrogen bonding of the histidines to nearby residues[10]. Examination of the crystal structure of bovine C*c*O[5] revealed that the peptide backbone oxygen of a conserved glycine in subunit I is hydrogen bonded to a histidine ligand of heme *a* in all mammalian aa_3-type oxidases and in many other species including yeast, wheat and *Thermus thermophilus* ba_3 oxidase[8, 11]. However, in the bacterial aa_3 oxidases, *Pd.* and *Rs.*, the glycine residue has been replaced with a serine (**Fig. 2.2**) with the hydroxyl group of the serine (S44) hydrogen bonded to the histidine (H102 in *Rs.*C*c*O). The other histidine ligand of heme *a* (H421) is surrounded by highly conserved hydrophobic/aromatic amino acids which coincide in an overlay of the *Rs* and bovine structures; thus, it is unlikely to be the source of the altered heme *a* properties between the mammalian and bacterial oxidases.

To test the possible effect of hydrogen bonding to the histidine ligand of heme *a*, the serine 44 residue in *Rs.*CcO was mutated to a glycine to resemble the bovine enzyme, creating a mutant S44G, and the serine was also replaced by an aspartic acid, an glutamate, and a glutamine, creating mutants S44D, S44E, and S44N respectively. With the serine to glycine mutation, a shift of the EPR spectrum towards bovine was observed as predicted; from serine to aspartic acid, and glutamine, the prediction of a shift of their EPR spectra away from bovine was also met, but to a different extent. Further electron

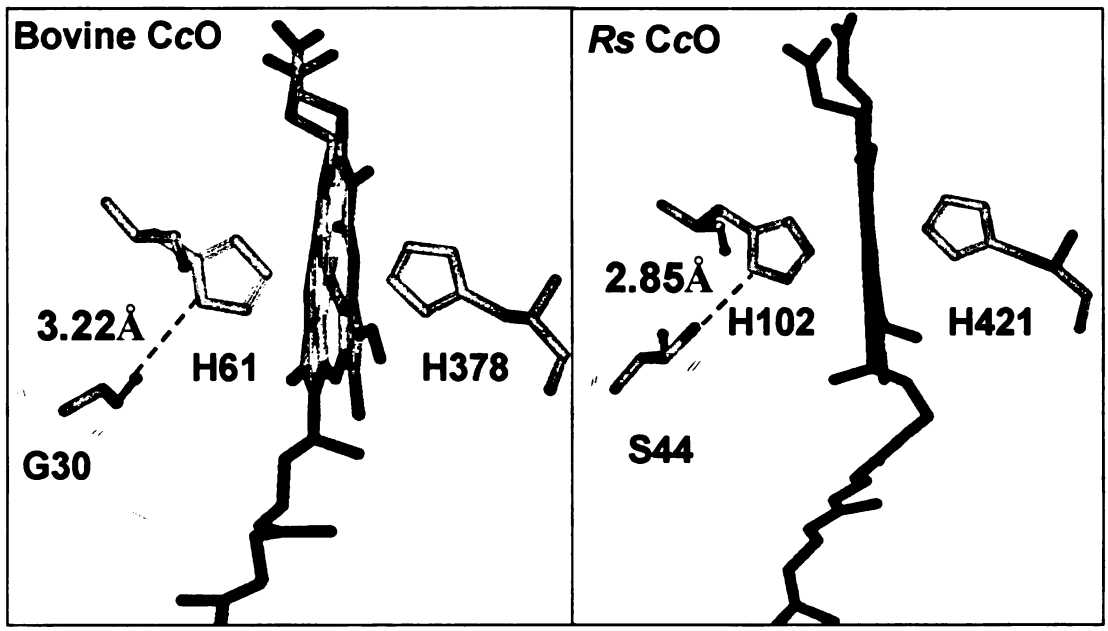

Figure 2.2: The ligands to heme *a* are shown for bovine (1V54 structure) and *Rs* (1M56) C*c*O. The residues that are closest to the heme *a* ligands are shown in stick structure. Bovine CcO shows a glycine (G30) with the carbonyl backbone oxygen hydrogen-bonding to His61. *Rs* C*c*O shows a serine (S44) with its hydroxyl hydrogen-bonding to His 102. The figure is the courtesy figure from Dr.Mills

transfer and fast kinetics measurements showed that the S44G mutant has a wild-type-like kinetic behavior while the electron transfer kinetics of the S44D mutant is significantly altered, leading to unique insights into the control of heme *a* redox behavior, and a potential tool for understanding the electron and proton movements.

2. Experimental Methods

2.1 Protein expression and purification

All the mutants were created by Dr.Hiser as described in[12]. The C*c*O protein was purified by Ni^{2+}-NTA affinity chromatography[13] and further purified by two tandem DEAE ion-exchange column (Tosohaas DEAE-5PW 10μ particle size, 8 mm x 7.5 cm) using a Pharmacia ÄKTA FPLC as previously described[13] to remove excess subunit I and the remaining contaminants. The enzyme was then concentrated and washed into the desired buffer using a Millipore centrifugal filter with a MW cut-off 100K. The amount of Mn^{2+} incorporated into the protein depends on the [Mg] to [Mn] ratio in the growth medium[10]. The YZ-100 strain of *R. sphaeroides*, which over-expresses the wild-type C*c*O with a histidine-tag added to the C-terminus of subunit I, was grown on "high Mn" medium (with $MnSO_4$ and $MgSO_4$ at final concentrations of 700μM and 50μM, respectively). The substitution with Mn^{2+} was necessary to make the native Mg^{2+} center into an EPR visible site. The visible spectral characteristics of Mg- and Mn-substituted wild-type enzymes were identical and oxygen consumption activities were not altered.

2.2 Reconstitution of cytochrome *c* oxidase into phospholipid vesicles (COVs)

All glassware was rinsed with ethanol. Asolectin was suspended to 40mg/ml by sonication in 2% cholate, 75 mM HEPES-KOH, pH 7.4, at 0 °C under argon. A Heat Systems-Ultrasonics sonicator (Model W-225), equipped with a microtip, was used at a power setting of 5 for intervals of 30 s on, 30 s off, until clarity was reached. The suspension was centrifuged for 15 min at 12,000 X g to remove titanium particles. Purified cytochrome c oxidase in 0.2% lauryl maltoside was preincubated with cholate detergent for 6.7mg per nmol enzyme for two hours before adding to the phospholipid suspension to a final concentration of 2 nmol/ml and then dialyzed with rapid stirring at 4 °C in Spectrapor dialysis tubing (number 25225/204, 12-14,000 *M,* cutoff) by the following protocol: 6 h in 100 volumes of 75 mM HEPES-KOH, pH 7.4, 14 mM KC1, 0.1% cholate; 12 h in 100 volumes of 75 mM HEPES-KOH, pH 7.4,14 mM KC1; 12 h in 100 volumes of 50 mM HEPES-KOH, pH 7.4, 24 mM KC1,15 mM sucrose; 12 h in 500 volumes of 1 mM HEPES-KOH, pH 7.4, 44.6 mM KC1, 43.4 mM sucrose[14, 15].

2.3 Activity of COVs under steady-state and stopped-flow proton pumping measurements

C*c*O was first reconstituted into asolectin lipid vesicles (COVs). Measurements of proton pumping were made on an OLIS-rsm stopped-flow with 100 μM phenol red, 50 μM HEPES-KOH pH 7.4, 45 mM KCl on the outside of the COVs, and 75 mM HEPES-KOH pH7.4 on the inside. Activities were obtained from averaging at least three measurements of cytochrome *c* oxidation from scanning a range of 155 nm (x nm -y nm) using double monochromators with a 500 blaze wavelength and a groove density of 600 lines. The rapid scanning of the wavelength range was at the rate of 1 scan/msec. The OLIS-rsm SVD Global Works software package was used to analyse the

spectra.Additionally, exponential fitting of the cytochrome *c* changes monitored at 550 nm using Microcal Origin™, in the absence of phenol red, was performed. The activities of the COVs were measured in the absence of ionophores, forming both a membrane potential and a pH gradient during turnover (controlled state). The addition of valinomycin to COVs removes the $\Delta\Psi$ (membrane potential), and this is the condition in which proton pumping is normally observed as a net acidification (decrease in absorbance) of the phenol red on the outside. The addition of FCCP removes the pH gradient (uncontrolled state) by allowing protons to equilibrate across the membrane, resulting in alkalinization on the outside (increase in absorbance), due to the net consumption of protons for the formation of H_2O at the active site.

2.4 UV-visible Spectroscopy

UV-visible spectra of fully reduced wild-type, S44G, S44D, S44N, and S44E proteins by addition of dithionite were recorded on a Perkin-Elmer Lamda 40P spectrophotometer scanning wavelengths from 400nm to 750nm after appropriate dilution into pH7.4 100mM HEPES, 0.1% lauryl maltoside.

2.5 Electron Paramagnetic Resonance Spectroscopy (EPR)

Continuous-wave X-band EPR spectra of purified *Rs.*C*c*O WT, S44G, S44D, S44E, and S44N were measured on a Bruker ESP300 equipped with a TE102 cavity resonator. Temperature was maintained at 4.5K using an Oxford ESR900 helium cryostat assembly. The g values were determined by direct measurements of the magnetic field strength and microwave frequency. Spectrometer conditions: microwave frequency

9.458GHz; microwave power 50μW; modulation amplitude was 20.0Gauss. Other conditions are described in figure legends.

Electron spin echo-detected EPR and three-pulse ESEEM spectra were recorded on a Bruker E-680X spectrometer operating at X-band and equipped with a model ER4118-MD-X-5-W1 probe that employs a 5mm dielectric resonator. The temperature was maintained at 4.5 K using an Oxford liquid helium flow system equipped with a CF-935 cryostat and an ITC-503 temperature controller. ESEEM data were collected using a three-pulse, stimulated echo sequence (90°-π-90°-T-90°) with 90° microwave pulse widths of 16ns. A four-step phase cycling sequence, together with the appropriate addition and subtraction of the integrated spin-echo intensities served to remove the unwanted echoes and baseline offsets from the data.

3. Results

3.1 Optical spectra and activity

UV-visible spectra of two mutants S44G and S44D in *Rs.Cc*O are similar to that of wild type enzyme with a Soret peak at 445nm and α peak at 606 nm, suggesting that there are no major changes in the environment of the hemes (**Fig.2.3**). For S44G, steady-sate studies (Mills, D.A) show that the maximal activity across the pH range from pH 6 to 9 is not altered, thus the mutation does not change the rate-limiting step in the turnover. Good proton pumping with a usual H^+/e^- ratio of ~1 from reconstituted COV (made by Dr.Mills, see methods) also indicates that S44G behaves just like wild type enzyme. For

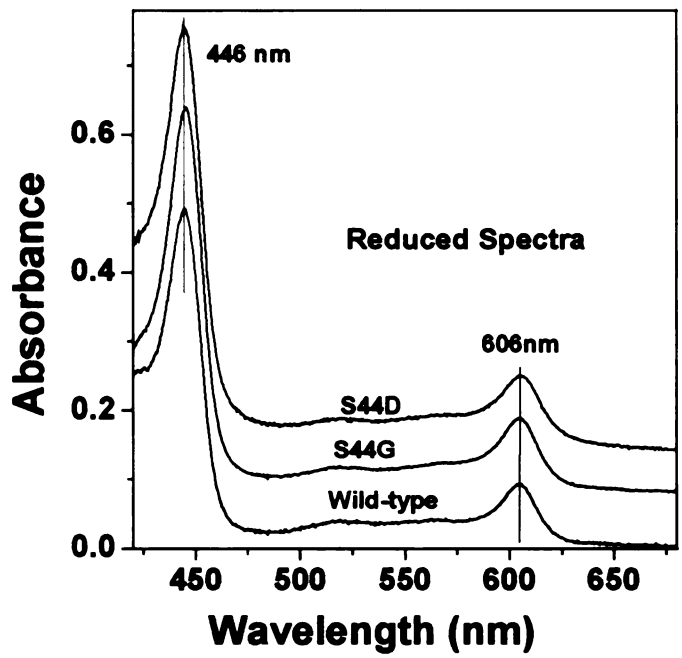

Figure 2.3: The visible spectra of reduced wild type, S44D, and S44G *Cc*Os. The figure is the courtesy figure from Dr.Mills

the S44D mutant, the activity is reduced to less than 30% of the wild-type activity at pH 6.5, under conditions of maximal steady-state activity (data not shown). S44D reconstituted into COVs also showed a lowered respiratory control ratio (RCR: uncontrolled rate/controlled rate). The controlled rate is normally inhibited by both a $\Delta\Psi$ (membrane potential) and ΔpH (pH gradient) and is usually the slowest rate. The proton pumping stoichiometry (H^+/e^-) for S44D is significantly lower than wild-type and S44G (**Table 1**).

S44D has the same pH dependence of its steady-state activity as the wild-type does. However, in the stopped-flow analysis, S44D shows a different pH profile with an apparent p*Ka* less than 6.0 (**Fig. 2.4**), due to different rate-limiting steps in the two assay systems.

3.2 X-band cw EPR

Mutants of serine 44 in *Rs.*C*c*O were created to test the proposal that the position 44 may be important in determining the differences in heme *a* EPR spectra. In **Fig.2.5**, the low-spin heme *a* spectra for wild-type *Rs.* C*c*O and mutants S44G and S44D are shown. The wild-type g values are 2.81, 2.31, and1.63, while bovine oxidase has different g values of 3.03, 2.21, and 1.45 for low spin heme *a* (green arrows), the EPR spectral features of Cu_A in bovine C*c*O are only slightly different from those of the *Rs.*C*c*O (g_z =2.18 and $g_{x,y}$=2.00).

		Activity (e /sec/aa_3)		
COVs	**pH**	**Cont.**	**Uncon.**	**RCR**
WT	**6.5**	**130±12**	**950±24**	**7.3**
	7.4	**80±1**	**1050±28**	**13**
S44D	**6.5**	**90±1**	**297±15**	**3.3**
	7.4	**47±1**	**185±5**	**3.9**
S44G	**6.5**	----	----	----
	7.4	**102±12**	**1020±53**	**10**

Table 1: The steady-state activity of S44G, S44D and wild-type at different pH. The steady-state activity measurements were made in a Gilson oxygraph with 30μM horse cytochrome *c*, 3mM ascorbate, 1mM TMPD, 2 mg of asolectin lipids, and 0.05% lauryl maltoside. Contr.= controlled proton-pumping rate measured in the absence of any ionophores. Uncon.= uncontrolled proton-pumping rate measured in the presence of uncoupler (2μM valinomycin + 5μM CCCP). RCR= respiratory control ration, is the ratio of the uncontrolled rate over the controlled rate.

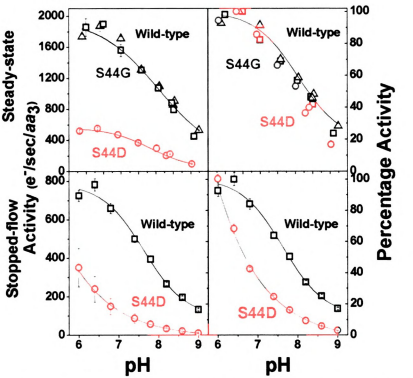

Figure 2.4: The steady-state activity assay of wild type, S44G, and S44D *Cc*Os. The top panel shows the steady-state activity of S44G, S44D and wild type at different pH. The left panel shows the activity (e^-/sec/aa_3) and the right panel shows the percentage activity. The bottom panel shows the activity measured under stopped-flow conditions where the rate of electron transfer is rate limiting. The figure is the courtesy figure from Dr.Mills.

The mutation of S44 in *Rs.*C*c*O to a glycine residue to resemble bovine did produce a shifted EPR spectrum of heme *a* with g values of 2.86, 2.30, and 1.60. All of these values are shifted towards those of bovine C*c*O, though the shifts are not as dramatic as would be expected if the residue were the only contributor to the difference between *Rs.* and bovine C*c*O.

The S44D mutant, however, shows spectral characteristics distinct from those of wild-type and S44G. In the gz region, two peaks for g_z = 2.72/2.78, and gy and gx values of 2.30 and 1.74, are considerably shifted in the opposite direction to those of bovine and of the S44G. When the EPR spectra are measured at different pH values ranging from 5.5 to 8.0, a big shift in the relative intensities of the peaks at 2.72/2.78 is observed: peak 2.72 had the highest intensity at pH 8.0 while peak at 2.78 had increased intensity at pH5.5, suggesting that the EPR spectrum is influenced by a protonation event (**Fig.2.6**). Spin quantification by double integration of two peaks shows that the total area under the peaks is comparable in magnitude at different pH values, indicating an interconversion between them. The results agree well with the proposal that 2.72 and 2.78 respectively represent the deprotonated and the protonated form of Asp 44 (**Fig. 2.6**). When the areas under the two peaks are plotted as a function of pH (**Fig. 2.7**), the p*Ka* of the interconversion is estimated to be less than 5.5, the lowest pH that can be measured without precipitation. This value is also consistent with the results of kinetic measurements of the intrinsic electron transfer rate from Cu_A to heme *a*[9].

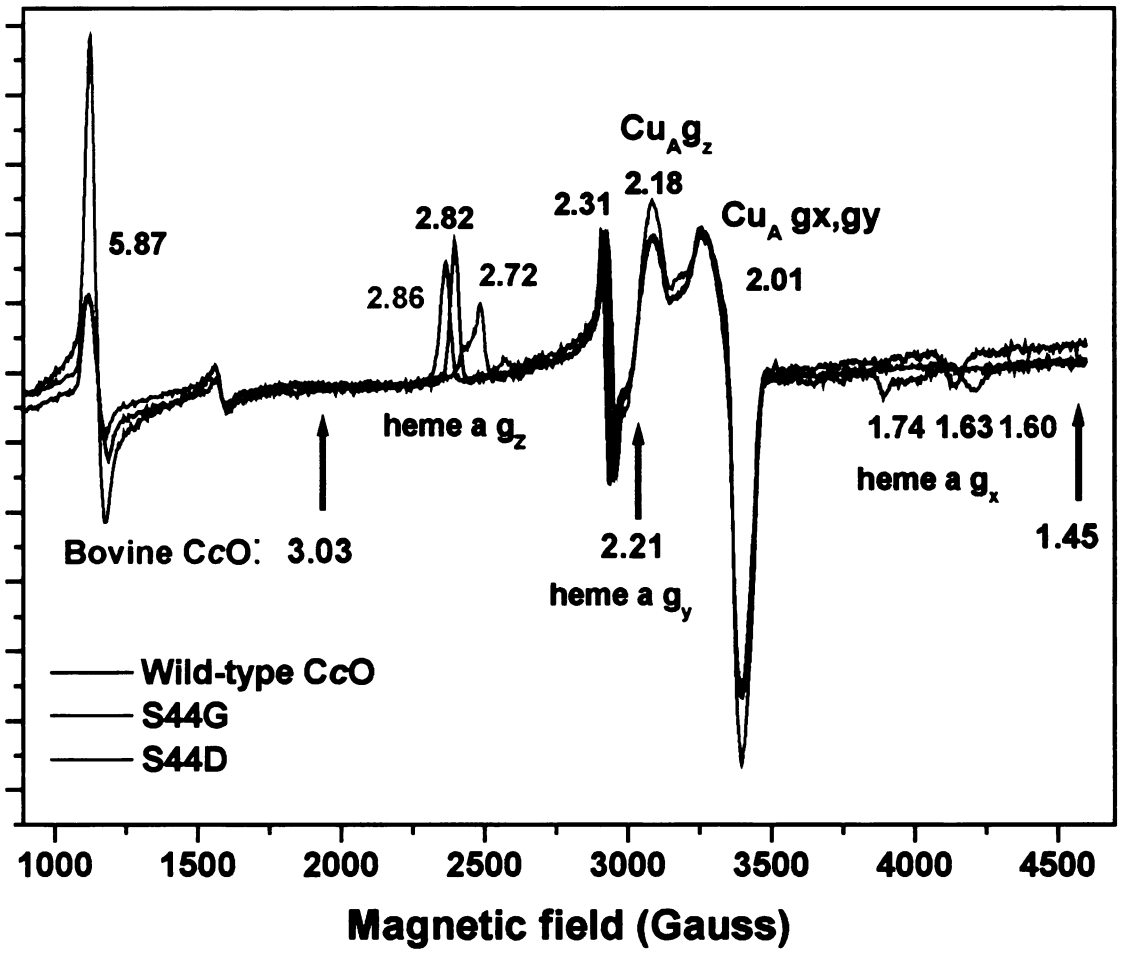

Figure 2.5: Overview of the EPR spectral changes with wild-type *Rs* CcO (black), S44G (red) and S44D (blue). Heme *a* g values of *Rs.* wild type, S44G and S44D are labeled on top of each corresponding peak, and bovine g values are listed beneath in green. Samples were made in buffer with 20mM HEPES-KOH, pH 8.0,14mM KCl, and 0.1%lauryl maltoside with the final concentrations of 82μM, 88μM, and 61μM respectively. The EPR experimental conditions are: microwave frequency: 9.458GHz; microwave power 50μW; modulation frequency: 100kHz; modulation amplitude, 20.0G; conversion time: 327msec; temperature: 4.2K.

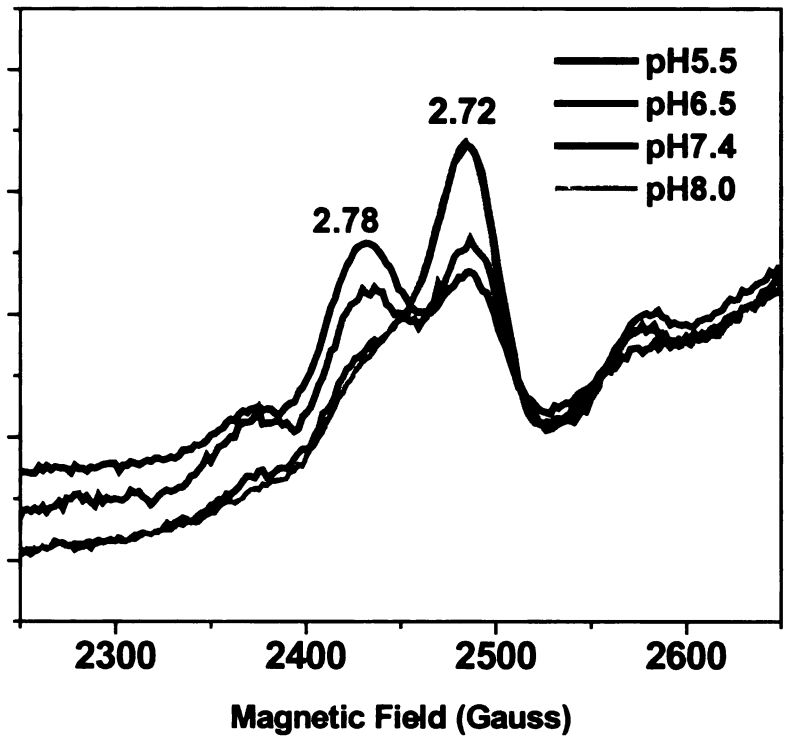

Figure 2.6: Effect of pH on heme *a* gz EPR spectra of S44D C*c*O. pH 5.5 and 6.5 buffer contained 50mM Mes-KOH, and 0.1%lauryl maltoside. pH 7.4 and 8.0 buffers contained 50mM Hepes-KOH, and 0.1%lauryl maltoside. Ionic strength was controlled by adjusting the conductivity using small amount of NaCl. pH 5.5, black; pH 6.5, red; pH 7.4, blue; pH8.0, cyan. EPR conditions are the same as described in figure 2.5.

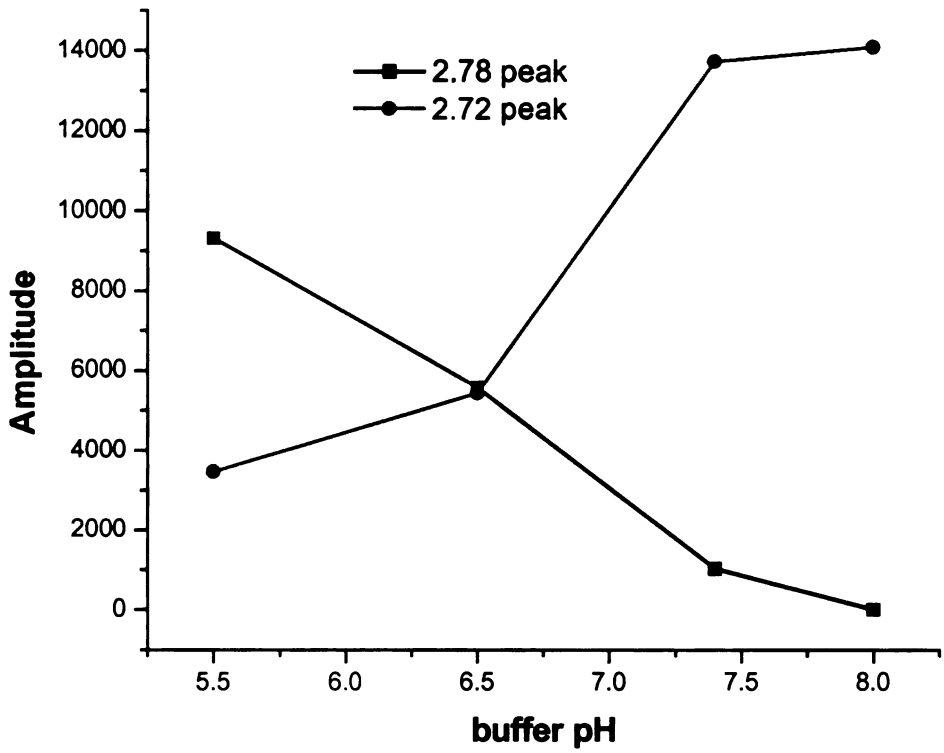

Figure 2.7: Plot of amplitude of 2.72/2.78 double peak for heme *a* versus buffer pH for S44D. Amplitudes were obtained by double integration of areas at two peaks respectively at different pH values. The sample and spectrometer conditions are the same as depicted in figure 2.5.

EPR spectra of samples at different ionic strength were also studied. Higher ionic strength had a similar effect on S44D as lowering pH, making the peak at 2.78 somewhat more intense, although not as dramatic an effect as when the pH is changed. Cytochrome *c* binding also caused a small shift in the relative intensities of the 2.78/2.72; in this case, lowering the intensity of 2.78 peak upon cytochrome *c* binding (**Fig. 2.8**). These results were also consistent with changes observed in kinetic measurements of the intrinsic electron transfer rates[12].

As a control for the effect of charge/protonation state in the S44D mutation, the S44 was mutated to a neutral residue, asparagine (S44N). The resultant EPR spectrum shifted in the same direction as S44D, but only had a single peak at g_z = 2.80, close to that of the apparent protonated form of S44D (**Fig. 2.9**). A further interesting mutant, S44E, also showed a shifted EPR peaks at 2.79, 2.29, and 1.66. To get a better understanding of the changes in EPR characteristics and electron transfer kinetics by these mutations, more EPR and kinetic measurements need to be done.

In the EPR spectrum of the S44D mutant of *Rs.*C*c*O, a relatively intense signal appears at g_z=5.87. This "g = 6" signal is normally attributed to high spin heme a_3. In wild-type C*c*O, due to antiferromagnetic coupling between high spin heme a_3 and Cu_B, very little EPR signal is usually visible in this region. From case to case, if the binuclear center is not perfectly coupled, a weak signal from high-spin heme a_3 is observed in this region in bacterial C*c*O as well as bovine enzyme. The presence of the larger signal in the

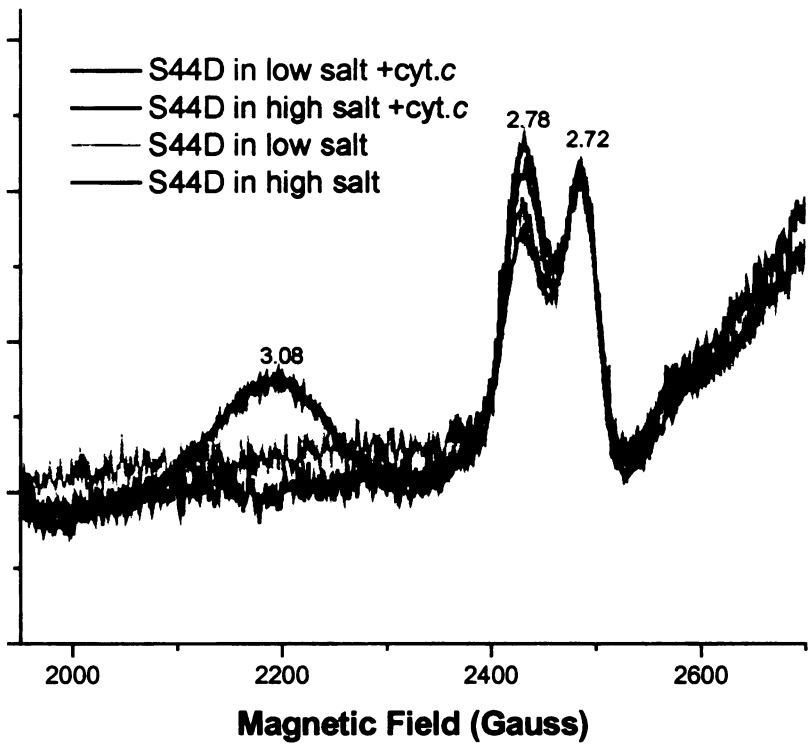

Figure 2.8: Effect of ionic strength and cytochrome *c* binding on heme *a* gz EPR spectra of S44D. Samples were made in buffers with 50mM Hepes-KOH, pH 7.4, and 0.1%lauryl maltoside for low salt and 50mM Hepes-KOH, pH 7.4, 150mM NaCl, and 0.1%lauryl maltoside for high salt. Cytochrome c and protein have same final concentrations. EPR conditions are the same as described in figure 2.5.

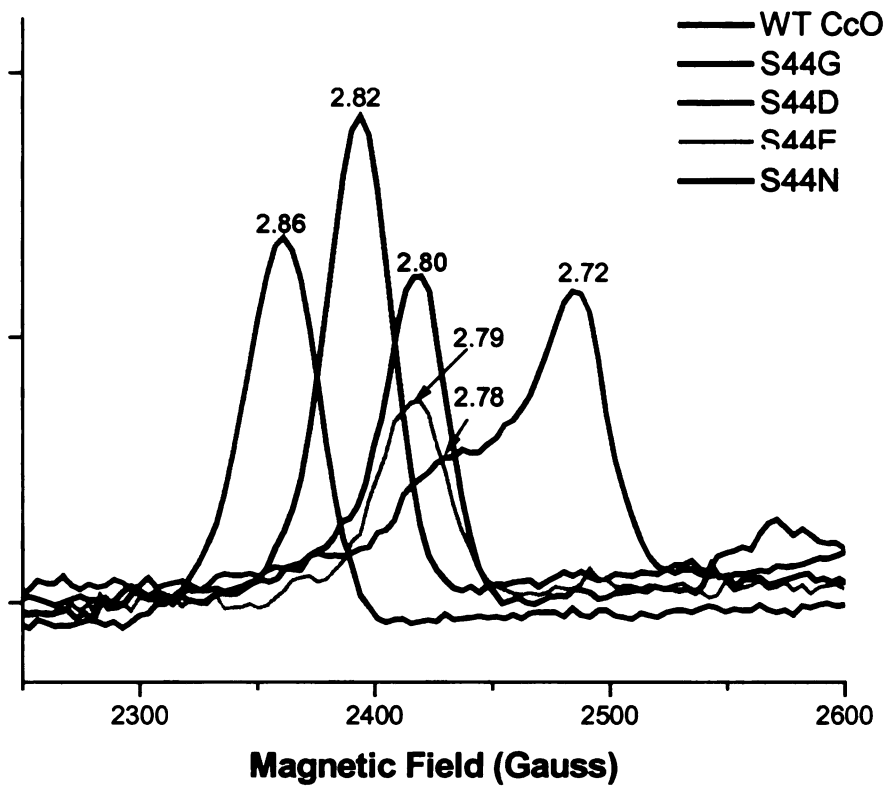

Figure 2.9: EPR spectra overlay of WT, S44G, S44D, S44E, and S44N in the g_z region. Wild type CcO: black; S44G, red; S44D, blue; and S44E, cyan; S44N, dark gray. EPR conditions are the same as described in figure 2.5.

S44D mutant suggests a decoupling that could be the result of some reduction of Cu_B due to the very low redox potential of heme *a* [9].

Above the heme *a* and heme a_3/Cu_B sites, there is one non-redox-active Mg metal site. It is centrally located at the interface of subunits I and II (**Fig.2.1**). Mg can be replaced by an EPR-visible metal, Mn, without any effect on enzyme function, and can be used as a probe to track conformational changes in the region[10]. EPR data indicated that the Mn spectrum in S44D is essentially the same as that of the wild-type enzyme. Unlike heme *a*, the Mn site is unaffected by buffer pH (**Fig.2.10**), ionic strength, and cytochrome *c* binding (data not shown), indicating that no general conformational change is involved in the EPR spectral changes observed in heme *a*.

As shown in **Fig.2.11**, a new EPR feature at g=2.01 region appeared in mutant S44N. This same signal was also observed in S44D samples from one preparation. The appearance of this signal was accompanied by a high spin heme a_3 signal in the g=6.0 region of the spectrum. Double integration revealed that the amount of EPR-visible Cu_A did not change very much (less than 30%). The integration error was estimated to be less than 20%; this error arises from the protein concentration estimate, the baseline correction routine, and the fact that there are small heme signals in the g=2 region at such a low temperature. Since a lowered redox potential of heme *a* in the deprotonated oxidized form of S44D was indicated by the rapid kinetic analysis of Cu_A to heme *a* electron transfer, it is possible that a new electron equilibrium caused this new feature. Various experiments were performed to determine where this feature came from. There

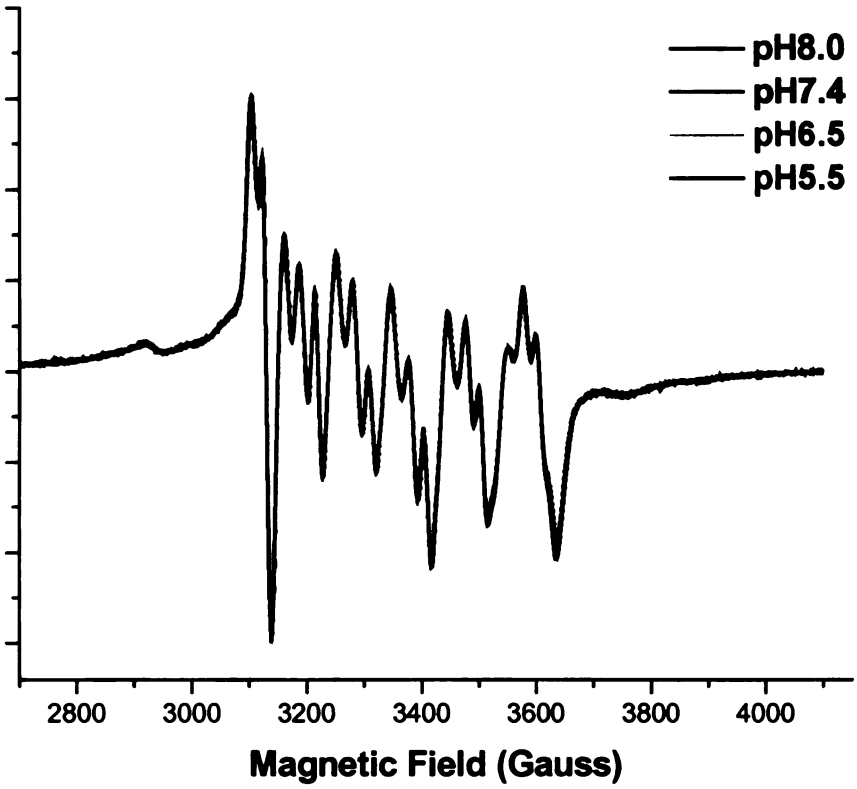

Figure 2.10: The pH profile of Mn EPR spectra of S44D. The buffer conditions and EPR conditions are the same as described in figure2.5

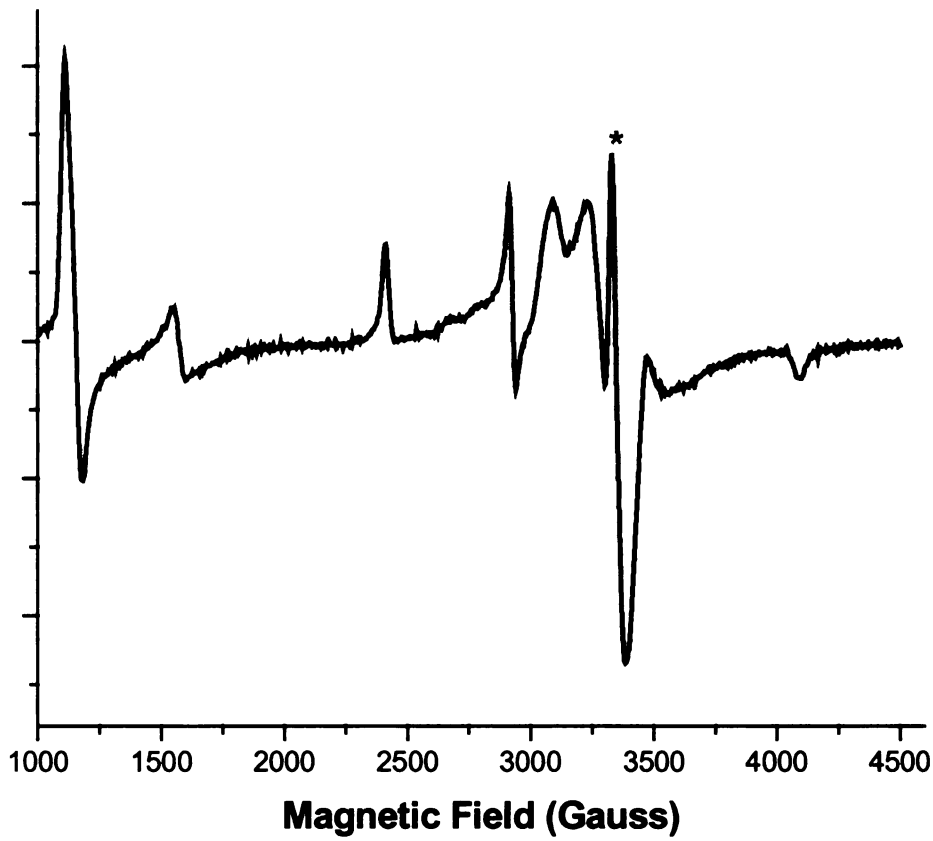

Figure 2.11: The cw EPR spectrum of mutant S44N. The red * indicates the new feature at g=2.0 region. The buffer conditions and EPR conditions are the same as described in Figure2.5

are many possibilities in terms of its origin. This signal could be from a disturbed Cu_A, or from a decoupled Cu_B, or even from a relatively stable radical. In power saturation experiments, microwave power from 0.199μW to 12.6mW was used, and the power saturation pattern for this new EPR feature was different from those of the heme *a*, and Cu_A (data not shown). The temperature dependence of its amplitudes was also studied (**Fig.2.12**). The disappearance of the signal at 110 K ruled out the possibility that the signal came from a radical since the species survived the purification procedure at room temperature. The heme a_3 signal at "g=6" region indicated that the heme a_3/Cu_B binuclear center might be decoupled to some degree upon mutation. As a result of this decoupling, the normally invisible Cu_B center may be observed in g=2.00 region, explaining the new sharp peak in the C*c*O spectrum. To test this speculation, echo-detected EPR absorption and three-pulse ESEEM experiments were carried out. The spectra at different shot repetition times (srt) had no significant difference. The three-pulse ESEEM spectrum of S44D was essentially the same as that of the wild-type C*c*O partly because the resolution is not high enough to recognize the difference if any.

4. Discussion

4.1 Spectroscopic Measurements

In the S44 mutants of *Rs.*C*c*O, there are distinctive alterations in the paramagnetic spectra. The mutation of S44G shifts the heme *a* peak from $g_z = 2.82$ to $g_z = 2.86$, in the direction of the heme *a* EPR signal of bovine oxidase which has a peak at g = 3.03. Additionally, the S44G mutation causes a shift in the low spin heme *a* g_y from 1.63 to

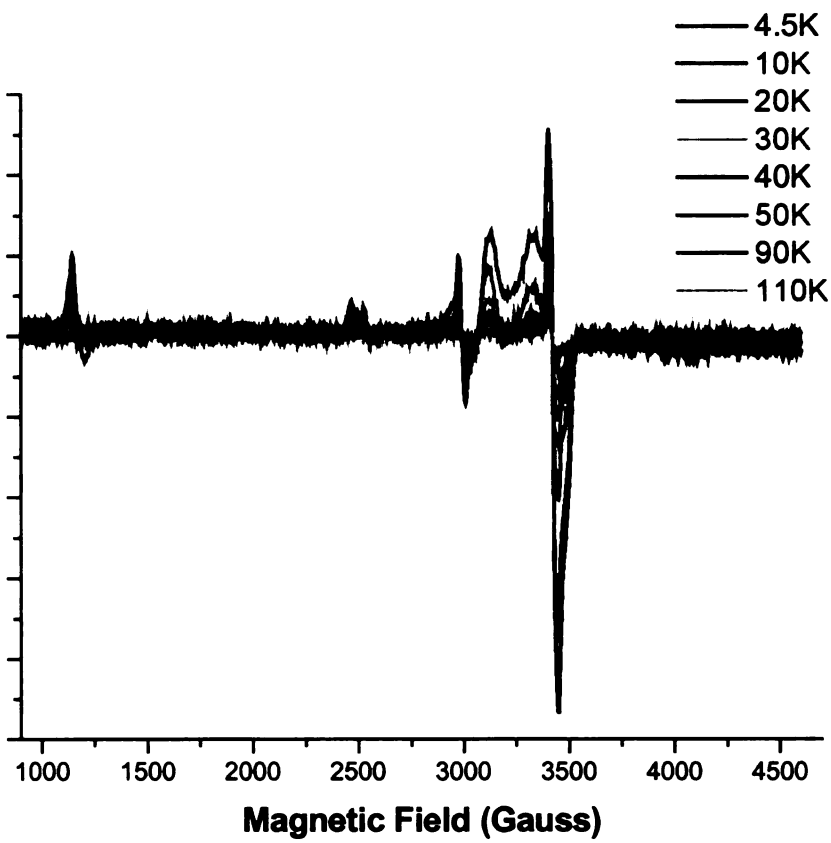

Figure 2.12: The temperature-dependence EPR spectra of S44D. The buffer conditions and EPR conditions are the same as described in figure2.5.

1.60, g_x from 2.31 to 2.30. These changes are not reflected in the visible spectrum of the S44G, which appears identical to wild type.

Despite the shift of the heme *a* g_z signal in S44G to a value closer to that of the bovine C*c*O, the shift by no means completely explains the major difference between the EPR spectra of *Rs* and bovine C*c*O. The remaining difference could be due to other residues that surround the histidine ligand on the same side as the glycine, which are not hydrogen bonded to the histidine. These less conserved residues are mostly hydrophobic and aromatic, and could affect the electronic configuration, augmenting the difference between the serine and the glycine hydrogen bonds[8].

For many years, chemists and bioinorganic chemists have been studying low spin heme complexes[16] and hemeproteins[17-20]. Their findings provided valuable information for understanding spin state, coordination number, the identity of axial ligands, and spectroscopic and magnetic properties of hemes. Among these researchers, Blumberg and Peisach[21] developed a method in which three g values obtained from EPR spectroscopic methods were reduced into two crystal field parameters ("tetragonality", Δ/λ, representative of the electron density at the iron, and "rhombicity", V/Δ, a pure geometric term), and then plotted as various sets individual points. Depending on the nature of the sixth ligand of heme proteins, five regions are arbitrarily drawn where parameters for the five different compounds may be expected to reside. The C group consists of low-spin minority species having methionine as the sixth ligand. The B and H groups consist of complexes of heme in which the sixth ligand is a histidine. The difference between

compounds lying in B and H groups lies in a difference in proton content. The imidazole of histidine in B type has a proton bound to it, while in the H complexes this proton is absent. The O region represents hydroxide forms of the α and β chains of hemes. The last group, P, represents a series of low-spin heme compounds in which the ligand of the heme is a alkyl mercaptide. The members of this group have similar EPR features to the cytochrome P450 family. With the help of "truth diagram", one can predict the electron density at the heme iron in target heme protein and further relate this to specific properties of heme and its axial ligands.

The tetragonality and the rhombicity parameters of bovine wild-type C*c*O, *R.s* wild type, and S44 mutant C*c*Os were calculated using Taylor's formalism[22]. It is interesting to observe that, except for the parameters of bovine C*c*O, the parameters of all the others fall into the H region, a region that contains hemes known to be ligated by an anionic histidine ligand. Points corresponding to S44G, S44N, and S44D are located in order from left to right of the H region, indicating an increase of charge density on the anionic histidine (**Fig.2.13**). For the model in which heme *a* is ligated by two neutral histidines, the tetragonality (Δ/λ) is 2.88; when the model is ligated by two deprotonated histidines, the tetragonality (Δ/λ) is 4.08. All of the calculated tetragonality values are in the middle of these two extremes. With a Δ/λ of 3.77, the apparently deprotonated form of S44D leans toward the extreme where two histidines are mostly deprotonated. Wild type bovine C*c*O (Δ/λ=3.15), on the other hand, is toward the other extreme with two neutral histidines; while both the *Rs.* wild type, and S44G C*c*Os have higher tetragonality values

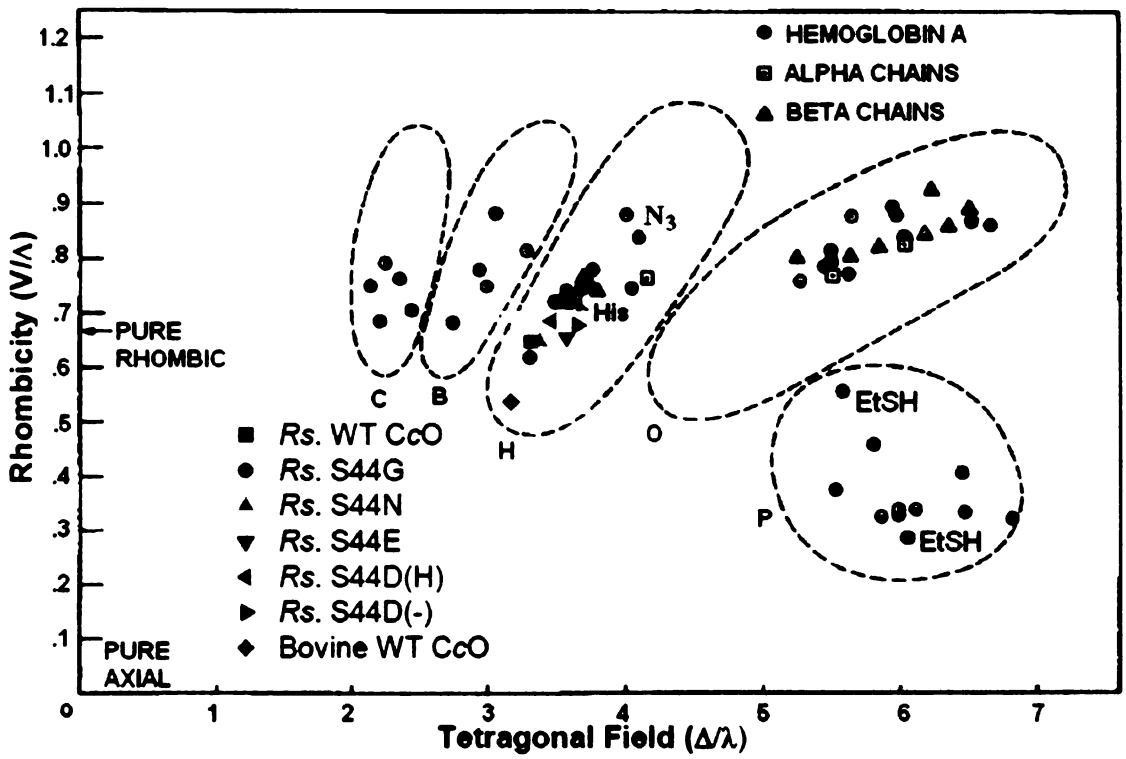

Figure 2.13: Crystal field parameters of bovine wild type C*c*O, *Rs.* wild type C*c*O, and S44 mutants in the frame of the Blumberg-Peisach truth diagram. C region represent the heme species with a methionine as the sixth ligand, B region represent the heme species with a neutral histidine as the sixth ligand, H region represent the heme species with a anionic histidine as the sixth ligand, O region region represent the heme species with hydroxide as the sixth ligand, and P region represent the heme species with an alkyl mercaptide as the sixth ligand. *Rs.*S44D (H) refers to protonated form of S44D where the calculations of tetragonal field and rhombicity are performed using g values of 2.78, 2.31, and 1.68. *Rs.* S44D (-) refers to deprotonated form of S44D where the calculations of tetragonal field and rhombicity are performed using g values of 2.72, 2.31, and 1.74.

(Δ/λ=3.33, 3.34 respectively), which means that there is an increase in electron donation by the axial histidines (**Table 2**).

Unlike the shifts in the heme *a* EPR spectrum of S44G, the shifts in S44D are in the opposite direction, moving further away from bovine C*c*O. EPR spectra of S44D at different pHs are consistent with data from kinetic analysis and electron transfer studies. All these results indicate that the carboxyl group of Asp at position 44 could exist as two differently protonated forms. At first glance, the UV-visible spectrum of the S44D mutant is identical to the wild-type enzyme. Close examination, however, reveals subtle changes in the apparent extinction coefficient at 606nm, a lowering by 20% to 30% compared to the extinction coefficient at 444nm. This change also shows some ionic strength- and pH-dependence, with the lowest extinction coefficient at higher pH. This data again suggests that Asp 44 could associate with the histidine ligand (H102) of the heme *a* in two forms, depending on the environmental pH conditions. The altered kinetics of electron transfer can also be explained by the protonation of Asp at low pH, which would reduce the negative charge in the region of the heme *a* ligand, H102.

Close examination of the local geometry of heme *a* and the nearby residue which is expected to form a hydrogen-bonding with the axial histidine ligand of heme a in crystal structures of bovine wild-type, *Rs.* wild type, S44D(H) and simulated structures of *Rs.* S44N, S44E, S44G revealed a good correlation between hydrogen-bonding distance and heme *a* gz value. Of these six different variants of C*c*O, bovine has the longest distance of 3.22Å and highest gz=3.03, followed by *Rs.* S44G with a distance of 3.03Å and

	gz	gy	gx	V/λ=A	B	Δ/λ =B-A/2	V/Δ
Rs. WT	2.82	2.31	1.63	2.26	4.46	3.34	0.68
Rs. S44G	2.86	2.3	1.6	2.14	4.4	3.33	0.64
Rs.S44N	2.8	2.31	1.65	2.31	4.58	3.42	0.68
Rs.S44E	2.79	2.29	1.66	2.54	4.94	3.67	0.69
Rs. S44D(H)	2.78	2.31	1.68	2.56	5.22	3.53	0.73
Rs. S44D(-)	2.72	2.31	1.74	2.7	5.12	3.77	0.72
Bovine WT	3.03	2.21	1.45	1.68	3.99	3.15	0.53

Table 2: EPR parameters for heme *a* in cytochrome *c* oxidase. The A and B can be calculated as follows: $A = \frac{g_x}{g_y + g_z} + \frac{g_y}{g_z - g_x}$, $B = \frac{g_x}{g_y + g_z} + \frac{g_z}{g_y - g_x}$

gz=2.86, the S44D has the shortest distance of 2.71Å and gz=2.78, and all other mutants have distances between 3.22Å and 2.71Å and g values between 3.03 and 2.78 (**Fig. 2.14**). The trend in distance change within all of six variants reflects the change in strength of hydrogen-bonding between axial histidine ligand and its partner, which is consistent with the result of Peisach-blumberg truth diagram analysis. Axial histidine in bovine wild type C*c*O has the least anionic character because of the weakest hydrogen bond between His61 and G30. Mutation of *Rs.* wild-type C*c*O to S44G made it more like bovine, resulting in a longer distance between His102 and S44G and decreased anionic character on His102. Further mutations to S44N, S44E, and S44D resulted in shortened distances and increased anionic character on His102. It is interesting to observe such a high degree of correlation and consistency within various methods of analysis, which suggests that EPR could be a powerful and independent method to investigate hydrogen-bonding properties of histidine of heme *a* in C*c*O. Without some crystal structures available, EPR data helped us visualize changes caused by mutations on heme *a* local hydrogen-bonding with good confidence. As EPR data and modeling indicated, a glycine residue could form a hydrogen bond in *Rs.* C*c*O with a slight movement of the peptide backbone, which was observed in crystal structure of *Rs.* S44D: similarly asparagine and glutamate seem to manage to accommodate themselves to the position in a manner similar to aspartic acid.

The origin of the new signal at g=2.01 in S44N and S44D is difficult to interpret. Previously, the observation of a Cu_B signal in the EPR spectrum was reported in C*c*O when heme a_3 was decoupled, in which EPR signals did not look like the observed signal[23]. Because Cu_B has different ligation environment than Cu_A does, Cu_B should have

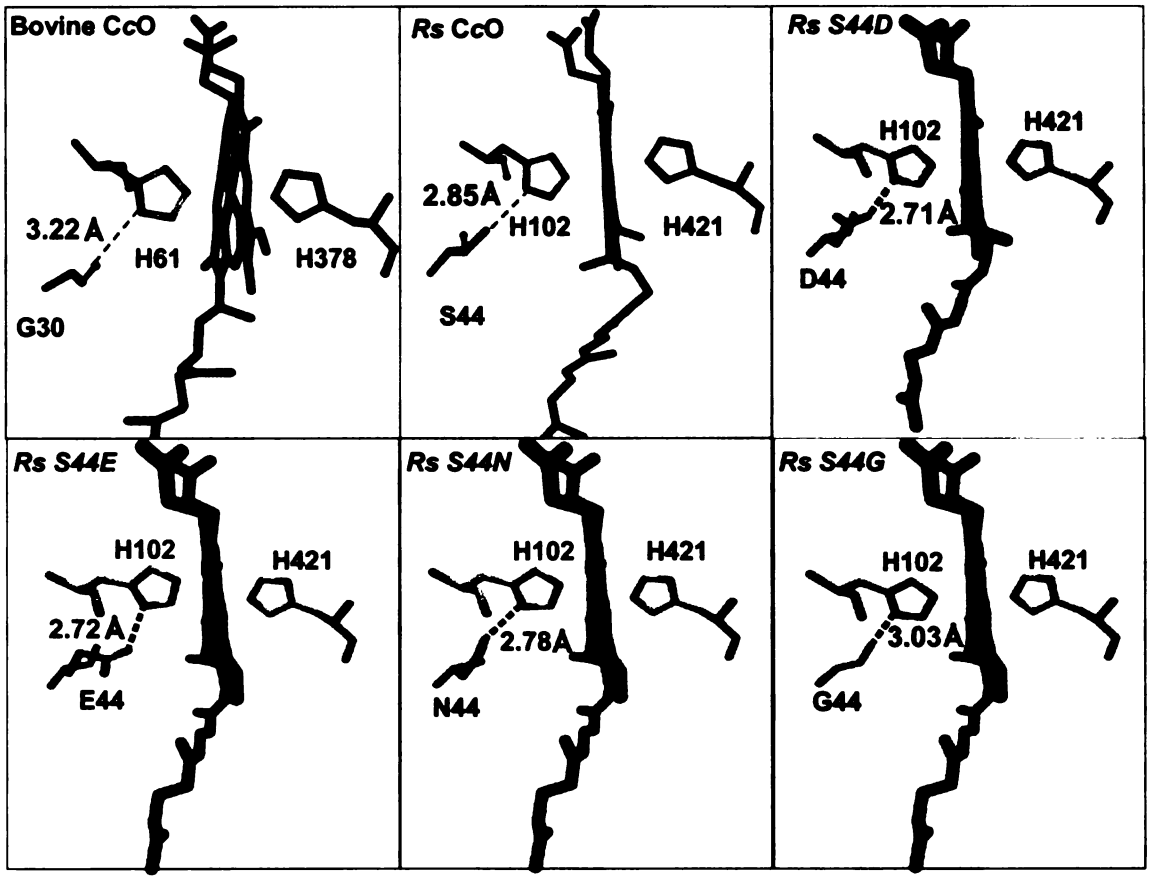

Figure 2.14: The ligands to heme *a* in crystal structures and simulated structures of C*c*O. The residues that are closest to the heme *a* ligands are shown in stick structure. Top figures are from crystal structures of bovine (1V54 structure) *Rs* wild-type C*c*O (1M56), and S44D (unpublished data). Bottom figures are simulated figures generated in Amber program using the crystal structure of *Rs.* wild type C*c*O as template. In simulation program, local geometry minimization is employed to mimic the most possible orientation of the mutated residue at 44.

different ESEEM data modulation pattern. However, three-pulse ESEEM data and echo-detected EPR absorption did not show significant alteration in modulation pattern to support the speculation that this new signal was from Cu_B. The formation of a radical is another possible explanation for the new signal in the g=2.0 region. However, the temperature dependence tests showed that the peak disappeared, along with other signals, when the temperature was increased to 110 K, which ruled out the possibility that it came from a radical considering the fact that this species survived the purification procedure at room temperature. The fact that there are so many overlapping signals in this region makes it a formidable task to find out the origin of this new feature even with higher-resolution techniques such as ESEEM or ENDOR.

Crystal structures of both the oxidized and reduced forms of the S44D mutant in (unpublished data, Qin,) at 2.8Å resolution show that the carboxyl group in D44 is disordered in the oxidized form, but is well resolved in the reduced state with one oxygen atom 2.7 Å from the His102 nitrogen. This finding is consistent with the results of kinetic analysis and the EPR spectra at different pH values, suggesting that the reduced state of heme *a* is stabilized by the protonation of S44D, and the protonated form has a strong hydrogen bond with the histidine nitrogen.

4.2 Effect of mutation on electron transfer and redox potential

For mutant S44G, little change of redox potential in heme *a* is observed, which is probably due to subtle changes in the region around heme *a*. These changes in structure

are not sufficient to cause any significant change in its electron and proton transfer behaviors in steady-state, stopped-flow, and photo-induced rapid kinetic measurements[12].

The mutation of S44 to an aspartate, on the other hand, caused a dramatic change in the kinetics of electron transfer from Cu_A to heme *a*. The electron transfer rate is very sensitive to pH change: at higher pH, the electron transfer is greatly slowed by a factor of 1000; at lower pH, the intrinsic electron transfer rate is biphasic, with a fast rate, followed by a slower rate similar to that at high pH. These observations, along with pH-dependent EPR changes, are most easily rationalized as being due to the ionization state of the aspartate carboxyl group. At higher pH, D44 is likely in its deprotonated state, resulting in a large decrease in the redox potential of heme *a* due to the proximity of the negative charge, and a slowed electron transfer from Cu_A. When the pH is lowered, D44 becomes partially protonated, leading to an increased redox potential and favoring heme *a* reduction. At high pH, the slow electron transfer rate from Cu_A to heme *a* suggests that the rate is dependent on slow access of protons to the S44D site, an example of proton coupled electron transfer (PCET). The observation that the rate of electron transfer at high pH is slow but the reaction goes to completion, indicates that D44 is eventually protonated and a normal redox potential is achieved. As shown in **Scheme 1**, at the beginning point, D44 is deprotonated and heme *a* is oxidized (a^{3+} COO) with a lowered redox potential; at the end, D44 becomes protonated and heme *a* is reduced (a^{2+} COOH) with a normal redox potential. At pH 6.5 and 5.5, D44 has a mixture of protonated/deprotonated forms, corresponding to the double peaks at 2.78/2.72 in EPR spectra, and this also explains the observed biphasic kinetics. The fraction that is

protonated (peak at 2.78) results in the rapid electron transfer from Cu_A to heme *a*, as in wild-type CcO. The fraction corresponding to deprotonated D44 (peak at 2.72) results in a very slow rate of electron transfer from Cu_A to heme *a*, which is rate-limited by the rate of protonation of D44.

This raises an interesting question as to where the protons come from to protonate D44, and to what extent the rate of proton transfer controls the intrinsic rate of electron transfer. It is noteworthy that the S44D mutant is less efficient at proton pumping, suggesting the possibility that the proton required for heme *a* reduction (D44 protonation) is stolen from the pumping path and then leaked when heme *a* is re-oxidized.

An internal rather than external source of protons is suggested by a low deuterium isotope effect[12] and by the fact that low pH does not increase the rate of the slow phase, only the proportion of fast versus slow phase in single electron transfer measurements. That Zn inhibition is not accentuated in the mutant also supports the internal proton source hypothesis. Further crystallographic and kinetic studies on the S44E and S44N mutants could give more insight into the altered EPR characteristics and provide useful tools for studying the role of heme *a* in the proton pumping mechanism.

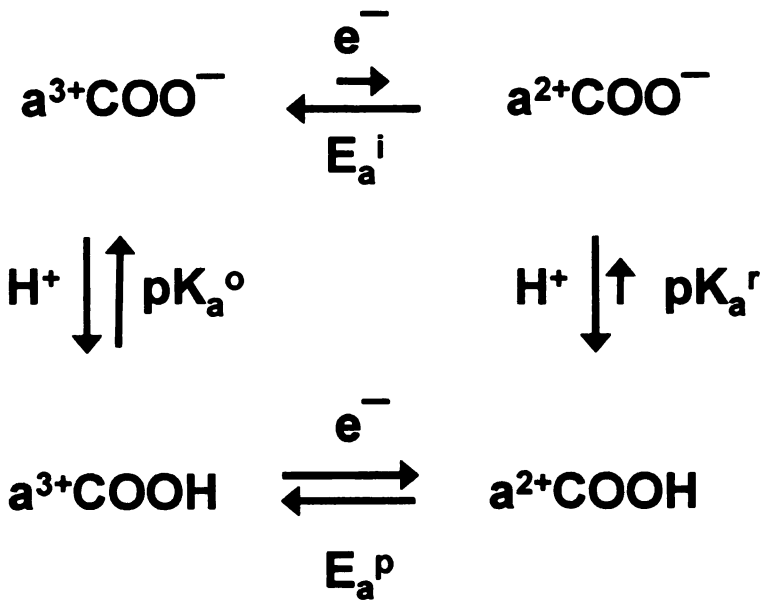

Scheme1

REFERENCES:

1. Pan, L. P.; Hibdon, S.; Liu, R.-Q.; Durham, B.; Millett, F., Intracomplex Electron Transfer Between Ruthenium-Cytochrome *c* Derivatives and Cytochrome *c* Oxidase. *Biochemistry* **1993,** 32, 8492-8498.

2. Pan, L. P.; Li, Z.; Larsen, R.; Chan, S. I., The Nature of Cu_x in Cytochrome *c* Oxidase. *J. Biol. Chem.* **1991,** 266, (3), 1367-1379.

3. Hill, B. C., The Reaction of the Electrostatic Cytochrome *c*-Cytochrome Oxidase Complex with Oxygen. *J. Biol. Chem.* **1991,** 266, (4), 2219-2226.

4. Rich, P.; Meunier, B.; Mitchell, R.; Moody, R., Coupling of Charge and Proton Movement in Cytochrome c Oxidase. *Biochim. Biophys. Acta* **1996,** 1275, 91-95.

5. Tsukihara, T.; Aoyama, H.; Yamashita, E.; Tomizaki, T.; Yamaguchi, H.; Shinzawa-itoh, K.; Nakashima, R.; Yaono, R.; Yoshikawa, S., Structure of Metal Sites of Oxidized Bovine Heart cytochrome c Oxidase at 2.8 Å. *Science* **1995,** 269, 1069-1074.

6. Svensson-Ek, M.; Abramson, J.; Larsson, G.; Tornoth, S.; Brzezinski, P.; Iwata, S., The X-ray crystal structures of wild-type and EQ(I-286) mutant cytochrome c oxidases from *Rhodobacter sphaeroides*. *J. Mol. Biol.* **2002,** 321, 329-339.

7. Qin, L.; Hiser, C.; Mulichak, A.; Garavito, R. M.; Ferguson-Miller, S., Identification of conserved lipid/detergent-binding sites in a high-resolution structure of the membrane protein cytochrome c oxidase. *Proc Natl Acad Sci U S A* **2006,** 103, (44), 16117-22.

8. Hosler, J. P.; Fetter, J.; Tecklenburg, M. M. J.; Espe, M.; Lerma, C.; Ferguson-Miller, S., Cytochrome aa_3 of *Rhodobacter sphaeroides* as a Model for Mitochondrial Cytochrome *c* Oxidase. *J. Biol. Chem.* **1992,** 267, (34), 24264-24272.

9. Millett, F.; Miller, M. A.; Geren, L.; Durham, B., Electron transfer between cytochrome c and cytochrome c peroxidase. *J Bioenerg Biomembr* **1995,** 27, (3), 341-51.

10. Hosler, J. P.; Espe, M. P.; Zhen, Y.; Babcock, G. T.; Ferguson-Miller, S., Analysis of Site-Directed Mutants Locates a Non-Redox-Active Metal near the Active Site of Cytochrome *c* Oxidase of *Rhodobacter sphaeroides*. *Biochemistry* **1995,** 34, 7586-7592.

11. Williams, P. A.; Blackburn, N. J.; Sanders, D.; Bellamy, H.; Stura, E. A.; Fee, J. A.; McRee, D. E., The CuA domain of Thermus thermophilus ba3-type cytochrome c oxidase at 1.6 A resolution. *Nat. Struct. Biol.* **1999,** 6, (6), 509- 516.

12. Mills, D. A. S. X., Lois Geren, Carrie Hiser, Ling Qin, Martyn A.; Sharpe, J. M., Bill Durham, Francis Millett*, Shelagh Ferguson-Miller*. Proton-Dependent Electron

Transfer from CuA to Heme a and an Altered EPR Spectrum in Mutants Close to Heme a of Cytochrome Oxidase *Biochemistry* **2008**.

13. Hiser, C.; Mills, D. A.; Schall, M.; Ferguson-Miller, S., C-terminal truncation and histidine-tagging of cytochrome c oxidase subunit II reveals the native processing site, shows involvemet of the C-terminus in cytochrome c binding, and imporves the assay for proton pumping. *Biochemistry* **2001,** 40, 1606-1615.

14. Fetter, J. R.; Qian, J.; Shapleigh, J.; Thomas, J. W.; García-Horsman, J. A.; Schmidt, E.; Hosler, J.; Babcock, G. T.; Gennis, R. B.; Ferguson-Miller, S., Possible Proton Relay Pathways in Cytochrome *c* Oxidase. *Proc. Nat. Acad. Sci. U. S.A.* **1995,** 92, 1604-1608.

15. Mills, D. A.; Ferguson-Miller, S., Influence of structure, pH and membrane potential on proton movement in cytochrome *c* oxidase. *Biochimica et Biophysica Acta* **2002,** 1555, 96-100.

16. Teschner, T.; Trautwein, A. X.; Schunemann, V.; Yatsunyk, L. A.; Walker, F. A., Low-spin ferriheme models of the cytochromes: Correlation of molecular structure with EPR and Mossbauer spectral parameters. *Hyperfine Interactions* **2004,** 156, (1), 285-291.

17. Gadsby, P. M. A.; Thomson, A. J., Assignment of the Axial Ligands of Ferric Ion in Low-Spin Hemoproteins by near-Infrared Magnetic Circular-Dichroism and Electron-Paramagnetic Resonance Spectroscopy. *Journal of the American Chemical Society* **1990,** 112, (13), 5003-5011.

18. Yonetani, T.; Schleyer, H., Electromagnetic Properties of Hemoproteins .2. Effect of Physical States on Electron Paramagnetic Resonance Parameters of Hemoproteins. *Journal of Biological Chemistry* **1967,** 242, (17), 3926-&.

19. Yonetani, T.; Schleyer, H., Electromagnetic Properties of Hemoproteins .I. Electron Paramagnetic Resonance Absorptions of Single Crystals of Ferrimyoglobin and Cytochrome C Peroxidase. *Journal of Biological Chemistry* **1967,** 242, (17), 3919-&.

20. Yonetani, T.; Yamamoto, H.; Erman, J. E.; Leight, J. S. J.; Reed, G. H., Electromagnetic Properties of Hemoproteins. V. Optical and Electron Paramagnetic Resonance Characteristics of Nitric Oxide Derivatives of Metalloporin-Apohemoprotein Complexes. *J. Biol. Chem.* **1972,** 247, (8), 2447-2455.

21. Peisach, J.; Blumberg, W. E.; Adler, A., Electron-Paramagnetic Resonance Studies of Iron Porphin and Chlorin Systems. *Annals of the New York Academy of Sciences* **1973,** 206, (Oct22), 310-327.

22. Taylor, C. P. S., Epr of Low-Spin Heme Complexes - Relation of T2G Hole Model to Directional Properties of G-Tensor, and a New Method for Calculating Ligand-Field Parameters. *Biochimica Et Biophysica Acta* **1977,** 491, (1), 137-149.

23. Pezeshk, A.; Torres, J.; Wilson, M. T.; Symons, M. C. R., The EPR spectrum for Cu-B in cytochrome c oxidase. *Journal of Inorganic Biochemistry* **2001,** 83, (2-3), 115-119.

CHAPTER 3

PULSED ELECTRON NUCLEAR DOUBLE RESONANCE STUDY OF AQUA PROTONS COORDINATED TO Mn (II) IN CYTOCHROME *C* OXIDASE

1.Introduction

An important bioenergetic function of cytochrome *c* oxidase is to pump protons across the membrane. Thus, it is important to be able to understand proton movements and the mechanism of proton pumping. In crystal structures of C*c*O, the non-redox active Mg site is located in an aqueous region[1](**Fig.3.1**), on the outer side of the membrane, which hints that it may function as a regulator of proton/water exit. The role of the Mg site in C*c*O is difficult to study because of its diamagnetic and non-redox active properties. However, the finding that Mg can be substituted by Mn without any functional effects opens a door for studying this site by EPR methods[2]. Previous studies in the Ferguson-Miller lab have shown some intriguing results[3, 4]. EPR and rapid freeze quench data using ^2H_2O indicate that the water ligands of the Mn^{2+}/Mg^{2+} site, or the protons of these waters, can exchange with bulk solvent at a rate consistent with a role for this region in product release during turnover. Further experiments using $H_2{}^{17}O$ and $^{17}O_2$ showed that water itself was able to reach the Mn^{2+}/Mg^{2+} site from the outside bulk water and from the interior active site. In these studies, the authors established a standard curve of $Mn^{2+}(H_2O)_6$ in different levels of ^2H_2O to estimate the number of exchanged water or protons. Although the estimated number is quite close to the result revealed by X-ray crystal structure assuming full substitution of liganded waters, this indirect method was a compromise using the low resolution of the EPR machine, at that time. However, the EPR machine has been upgraded, and a better quality, higher resolution, and more direct measurement of echo modulation of Mn^{2+} by its water ligands, can be achieved. In ESEEM, the modulation depth is proportional to n/r^6 where n is the number of nuclei

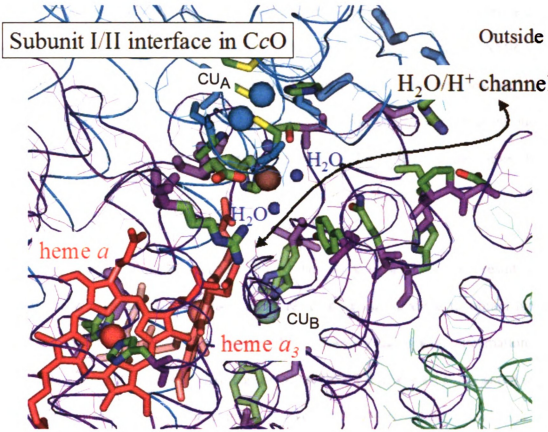

Figure 3.1: Proposed water channel in bovine CcO. Blue ribbons on the top are from subunit II which houses dinuclear Cu_A site (blue spheres). The green ribbons on the far right represent subunit III, which does not have any metal centers and its function is unclear. The purple ribbons represent subunit I which contains two hemes (red) and Cu_B site (light green sphere). The proposed water channel is shown as the gap between subunits I and II, beginning near heme a_3 propionates and the Mg/Mn site (brown sphere), with residues lining the channel in ball-and stick form. The three small blue spheres represent crystallographically visible water molecules. The figure is from Florens, L. et al[3]

coupled to the paramagnetic center and r is the dipolar distance. With either parameter unknown, it is hardly possible to figure out the other parameter without guessing. However, using ENDOR, we can measure r directly by measuring the hyperfine coupling constants. Then we can gain knowledge of the number of coupled nuclei. NMR has been the major method to study the hyperfine coupling interactions between Mn^{2+} and its nearby nuclei. However, most of the hyperfine information was obtained indirectly, which is by measuring the relaxation properties. ENDOR, on the other hand, is straightforward in determining the hyperfine coupling constants.

The electron spin states of Mn^{2+} have relatively long lifetimes. As a result, the EPR signals have narrower line-widths. Therefore, it is usually possible to obtain hyperfine-coupling information from the resolved EPR features and obtain information on the ligand environment. The signature feature of an Mn EPR spectrum is the sextet splittings which arise from the hyperfine coupling between Mn unpaired electrons and its nucleus (I=5/2). However, these hyperfine splittings are not as useful as expected because the sensitivity of the EPR measurement is somewhat diminished by the complicated appearance of EPR spectrum resulting from overlapping of the hyperfine splittings, which are due to each of the five allowed EPR transitions (**Fig.3.2**). It is important to sort out these couplings in the ENDOR pattern, and obtain intrinsic dipolar and contact contributions. Scholes and coworkers[5], using a simple system of manganese hexaquo as the model, did an excellent job in addressing this issue and provided us with a good reference to start with. In this chapter, the same method was applied to a far more

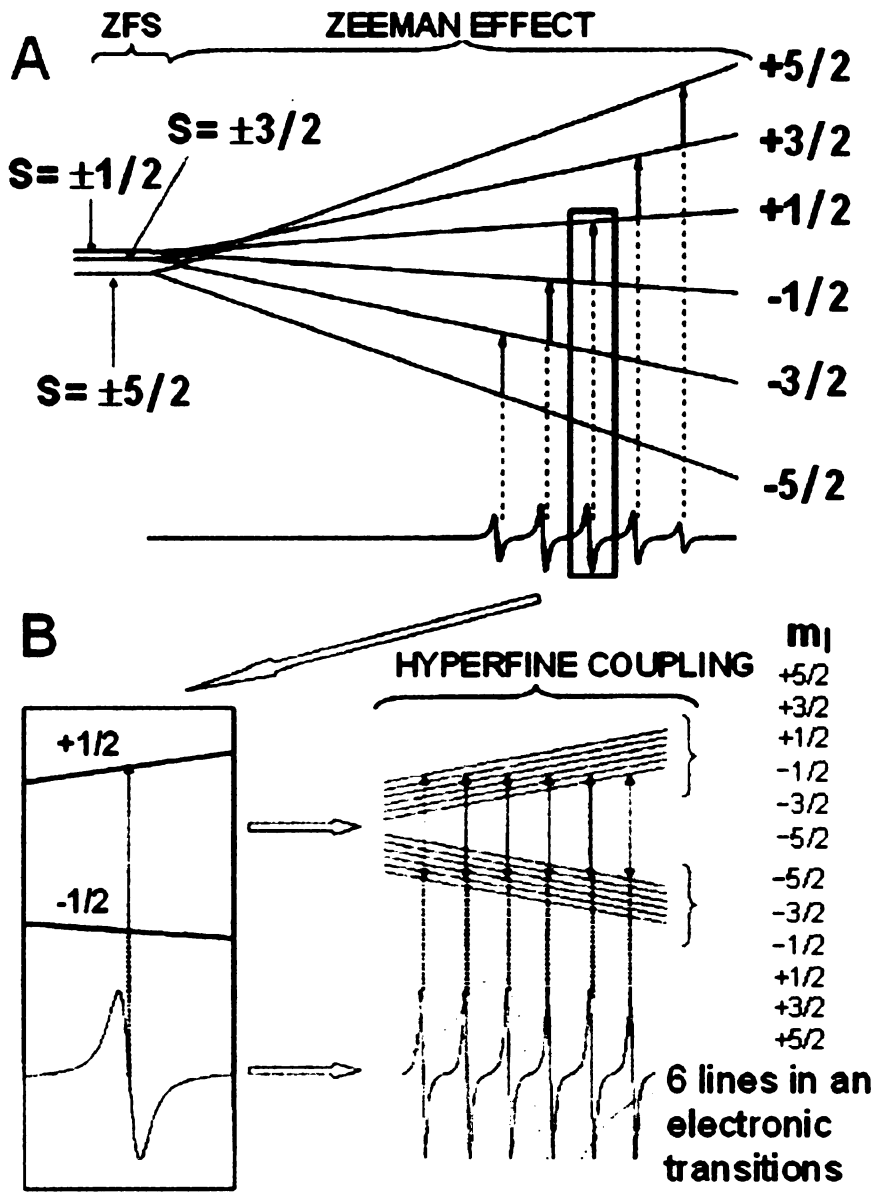

Figure 3.2: Diagram of Mn(II) energy level and EPR transitions. ZFS represents zero-field-splitting. The figure is a modification of a figure from Reed, G. et al [6]

complex system, C*c*O, using Davies ENDOR to study the hyperfine coupling interactions between Mn and its water ligands. The pulse sequence of Davies ENDOR is depicted in a figure (**Fig.3.3**). According to the principles established by previous researchers, ENDOR amplitudes from nuclei with small hyperfine couplings (A<2MHz) are enhanced by longer microwave pulse widths, and ENDOR amplitudes from nuclei with larger hyperfine couplings (A>2MHz) are enhanced by shorter microwave pulse widths with higher magnetic field strengths. In my experiments, different widths of the microwave pulse were used to selectively observe nuclei either strongly or weakly coupled to the Mn^{2+} site. The inner sphere water ligands of the Mn^{2+} site are the focus of my study, therefore, a shorter width of pulse could enhance the ENDOR amplitude, and was used in these experiments.

2. Experimental Methods

2.1 Protein production and purification

The amount of Mn^{2+} incorporated into the protein depends on the [Mg] to [Mn] ratio in the growth medium[2]. The YZ-100 strain of *R. sphaeroides*, which over-expresses wild-type C*c*O with a histidine-tag added to the C-terminus of subunit I, was grown on "high Mn" medium (with $MnSO_4$ and $MgSO_4$ at final concentrations of 700μM and 50μM, respectively). The protein was purified by Ni^{2+}-NTA affinity chromatography and further purified by DEAE ion-exchange chromatography[7] to remove excess subunit I and the remaining contaminants. The procedure involves washing the protein with buffer containing 1mM EDTA to remove the adventitious free extrinsic Mn ions. The enzyme

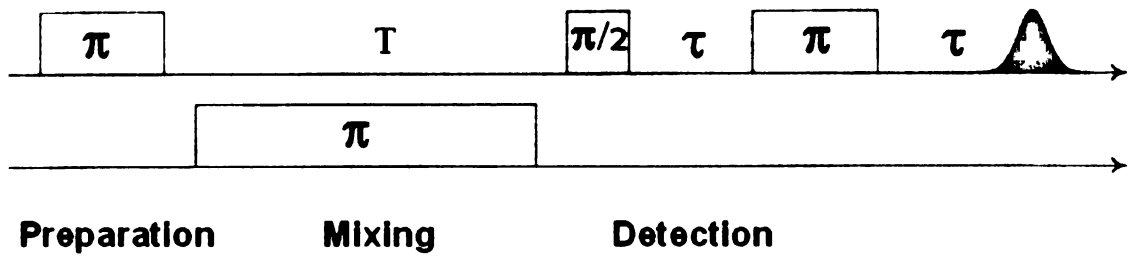

Figure 3.3: Pulse sequence for Davies ENDOR experiment. The figure is a modification of the figure from Prisner, T. et al.[8]

was then concentrated and washed into the desired buffer using a Millipore centrifugal filter with a MW (Molecular Weight) cut-off 100KDa. The visible spectral characteristics of Mg- and Mn-substituted wild-type enzymes were identical and oxygen consumption activities were not altered[2]. The visible spectrum of the resting enzyme also indicated that the purified enzyme is in its oxidized form (**Fig 3.4**).

2.2 Sample preparation

The oxidized sample was made by mixing wild-type Mn (II) substituted C*c*O in 20mM HEPES-KOH buffer, 15mMKCl, 0.1% lauryl maltoside, at pH7.4, resulting in a sample of the protein and glycerol having a final concentration of 148μM and 40%(v/v) respectively. The solution was then degassed by purging with argon gas for more than 30 minutes and then quickly transferred to an EPR-ENDOR tube and frozen in liquid nitrogen. The reduced sample in 100 mM HEPES-KOH buffer, 0.1% lauryl maltoside, at pH7.4 was made by first reducing the enzyme with dithionite with a final concentration of 25mM. Then the same procedure for preparing the oxidized ENDOR sample was followed.

2.3 X-band pulsed electron nuclear double resonance Spectroscopy (ENDOR)

X-band (microwave frequency 9.72GHz) pulsed-ENDOR spectra were measured on a Bruker E-680X spectrometer equipped with an EN 4118X-MD-4-W1 resonator. The temperature was maintained at 4.5 K using an Oxford Instruments liquid helium flow system equipped with a CF-935 cryostat and an ITC-503 temperature controller. ENDOR spectra were recorded using a Davies pulsed-ENDOR sequence. The relative ENDOR

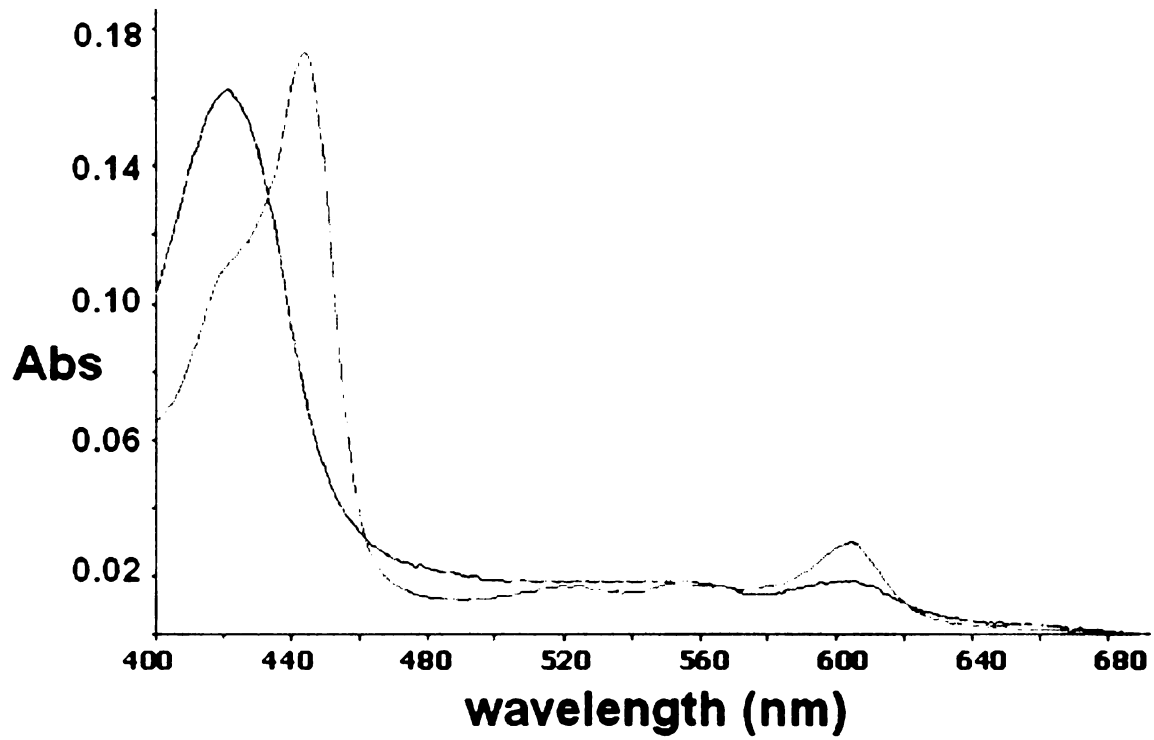

Figure 3.4: The visible spectrum of Mn-substituted C*c*O at resting (blue) and dithionite-reduced (red) states.

amplitude can be enhanced based on the magnitude of the hyperfine-coupling interactions. The choice of pulse widths is therefore an important factor in improving ENDOR sensitivity. The ENDOR conditions used in this study are: microwave π pulse of 96ns and a $\pi/2$ pulse for 48ns.The radio frequency π pulse was 8000ns and was started at 1000ns after the first microwave π pulse. The second microwave $\pi/2$ pulse followed at 1000ns at the end of the radio frequency pulse. The delay time between two pulses of the detection Hahn-echo sequence was 400ns.

2.4 Simulation of EPR and ENDOR spectra

As a hard metal, Mn^{2+} has an affinity for hard oxygen or nitrogen-containing ligands such as water, carboxylate, and histidine. In C*c*O, the Mn^{2+} ion was observed to be ligated by six ligands: three water molecules, two carboxylates, and one histidine[1]. The distorted octahedral coordination of Mn^{2+} generates zero-field splittings in the frozen solution. Such zero-field splittings cause a broadening of the EPR spectrum on either side of the central g=2.00 feature, and shift the EPR intensity away from g=2.00 to contain contributions from M_s= ±3/2 and ±5/2 electron spin states, although not as significantly as seen in the manganese hexaquo.

EPR spectra simulations were accomplished by using software Xsophe which is the standard software on a Bruker E-680X machine. The electronic spin Hamiltonian for Mn^{2+} can be written as: $He = g_e\beta_e \mathbf{H}\bullet\mathbf{S} + D\,[S_z^2 - 1/3S(S+1)] + A\mathbf{I}\bullet\mathbf{S}$ where the first term is the electron Zeeman interaction. The second term is the zero-field splitting term, and the "z" axis is the direction of the distortion from octahedral symmetry. Due to nearly

spherical distribution of electron spins about the Mn nucleus, the Mn hyperfine coupling is treated as isotropic and the third term represents the isotropic electron-nuclear hyperfine coupling. In the simulation, the zero-field splitting parameters of D =145G, and A =96.5G were used[9].

The simulation strategy for ENDOR is based on the ENDOR work done by Kwiram et al.[10]. The ENDOR frequencies of the protons coupled to the Mn (II) can be expressed as:

$$\nu(\theta,\phi) = \{\sum_{i=1}^{3}[l_i^2(\theta,\phi)(A_i M_s - \nu_0)^2]\}^{\frac{1}{2}} \qquad 3.1$$

Where θ and ϕ are the spherical polar angles relating the applied magnetic field to the principal axes of the hyperfine tensor. ν_0 is defined by $g_n\beta_n H_0/h$. $l_1 = \sin\theta\cos\phi$, $l_2 = \sin\theta\sin\phi$, and $l_3 = \cos\theta$. The A_1, A_2, and A_3 are principal hyperfine coupling constants, and M_S represents the electron spin quantum number.

The simulation procedure contains four steps: first, the powder pattern for each electron spin transition was obtained according to equation 3.1, then same procedure was applied to the next transition, until all five electron spin transitions were completed. Second, was to use the Simpson's rule to approximate the integral of the $\nu(\theta,\phi)$ function over all angles. The next step was to multiply the overall ENDOR powder pattern by the proper weightings (underlying EPR intensities obtained from echo-detected EPR spectrum). In the last step, the resultant histogram was smoothed by the Gaussian convolution function in Matlab program. At 2K or less there is a thermal population

difference between Mn^{2+} with different M_S quantum number, which cannot be ignored. This Boltzmann population factor was not included in this simulation because the experiments were performed at a relatively high temperature, 4.5K. As a result, there is no difference in intensity for transitions $|-3/2> \leftrightarrow |-1/2>$ and $|+1/2> \leftrightarrow |+3/2>$. For the same reason, $|-5/2> \leftrightarrow |-3/2>$ and $|+3/2> \leftrightarrow |+5/2>$ have the same intensity.

3 Results and Discussion

3.1 Electron spin-echo-detected absorption EPR spectroscopy

As a starting point for the later theoretical simulations, the EPR absorption spectrum was monitored by the spin-echo amplitude at 4.5K (**Fig.3.5**). The spectrum contained the EPR transitions due to the Mn (II) S=5/2 spin sextet. The six relatively narrow lines are due to the central transition of the S=5/2, split by the hyperfine coupling interactions with Mn (II)'s I=5/2 nuclear spin. The broad unresolved background is due to other electron spin transitions that contribute intensity to the central region of the spctrum. The relative contributions from individual transition were estimated using the Xsophe program equipped on Bruker E680 machine. The zero-field splitting parameters used in the simulation are from the reference[9]. The relative weights of these transitions are: 0.36 for $|-1/2> \leftrightarrow |+1/2>$, 0.20 for $|-3/2> \leftrightarrow |-1/2>$, 0.20 for $|+1/2> \leftrightarrow |+3/2>$, 0.12 for $|-5/2> \leftrightarrow |-3/2>$, and 0.12 for $|+3/2> \leftrightarrow |+5/2>$. These weightings are an approximate estimation, but represent fairly well the contributions from different electron spin states.

3.2 ^{1}H ENDOR spectroscopy

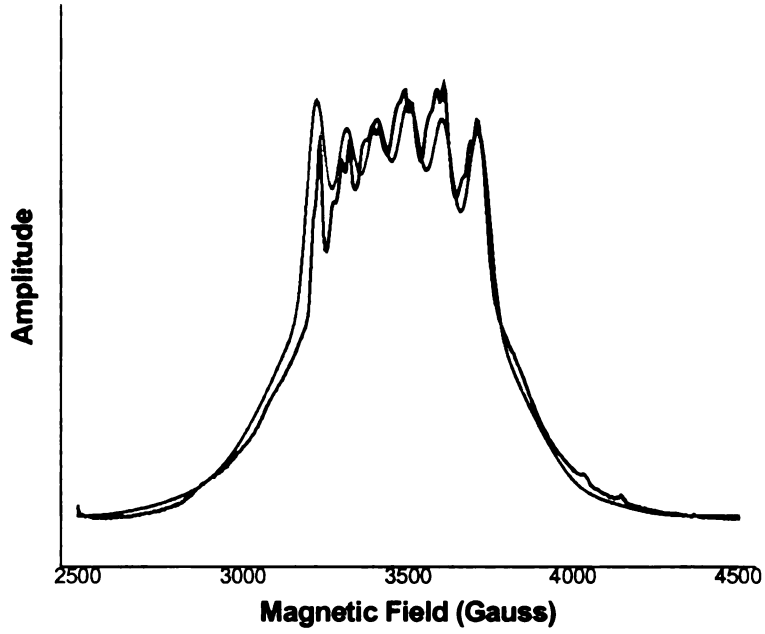

Figure 3.5: Experimental (black) and simulated (red) electron spin-echo-detected absorption EPR spectra of Mn-substituted cytochrome *c* oxidase. Experimental conditions for the measurement: νe =9.712GHz; central field is 3.5KG, mw pulse widths 48ns and 96ns for π/2 and π pulses, respectively; temperature, 4.5K. Simulation conditions are: D=145G; E/D=0.193; A=96.5G; Weightings from the individual transitions are 0.36 for |-1/2> ↔ |+1/2>, 0.24 for |-3/2> ↔ |-1/2>, 0.22 for |+1/2> ↔ |+3/2>, 0.08 for |-5/2> ↔ |-3/2>, and 0.10 for |+3/2> ↔ |+5/2>.

Davies ENDOR was recorded at a central field of 3700G within the central transition region, where the microwave frequency is about 9.72GHz. As **Fig.3.6** shows, the ^{1}H ENDOR signals lie approximately symmetrical with respect to the proton Larmor frequency and are split by hyperfine coupling interactions. The spectra of oxidized and dithionite-reduced proteins were obtained under conditions that optimize the coupling through bond features between 9 and 22MHz. The features are centered at the free proton Larmor frequency (ν_p) and have splittings away from ν_p of ±1.6, ± 4.7, and ± 7.4MHz. These splittings have a ratio of approximately 1:3:5, indicating that these features were mostly from the same type of proton nucleus, where it was respectively coupled to electron spin states ±1/2, ± 3/2, and ± 5/2. The spectra of oxidized and dithionite-reduced ENDOR samples are similar to each other except that the spectrum of the reduced sample is more symmetrical in terms of the splittings centered at ν_p. Most of the shoulders in the spectrum vanished in the deuterated protein sample, suggesting that the protons are exchangeable (**Fig.3.7**). The residual shoulder features of the ENDOR spectrum are most likely from incomplete deuteration because exchanging the protein into $^{2}H_2O$ cannot achieve 100% efficiency. Another reason is that the presence of the non-exchangeable protons from non-deuterated glycerol (added as cryoprotectant) and the protein.

Although the C*c*O ENDOR spectrum has the same basic shape as the Mn $(H_2O)_6$ complex, the former has a far more complicated spectrum. Peaks and shoulders from M_S = ±3/2 and ±5/2 were hidden in the baseline and are difficult to recognize.

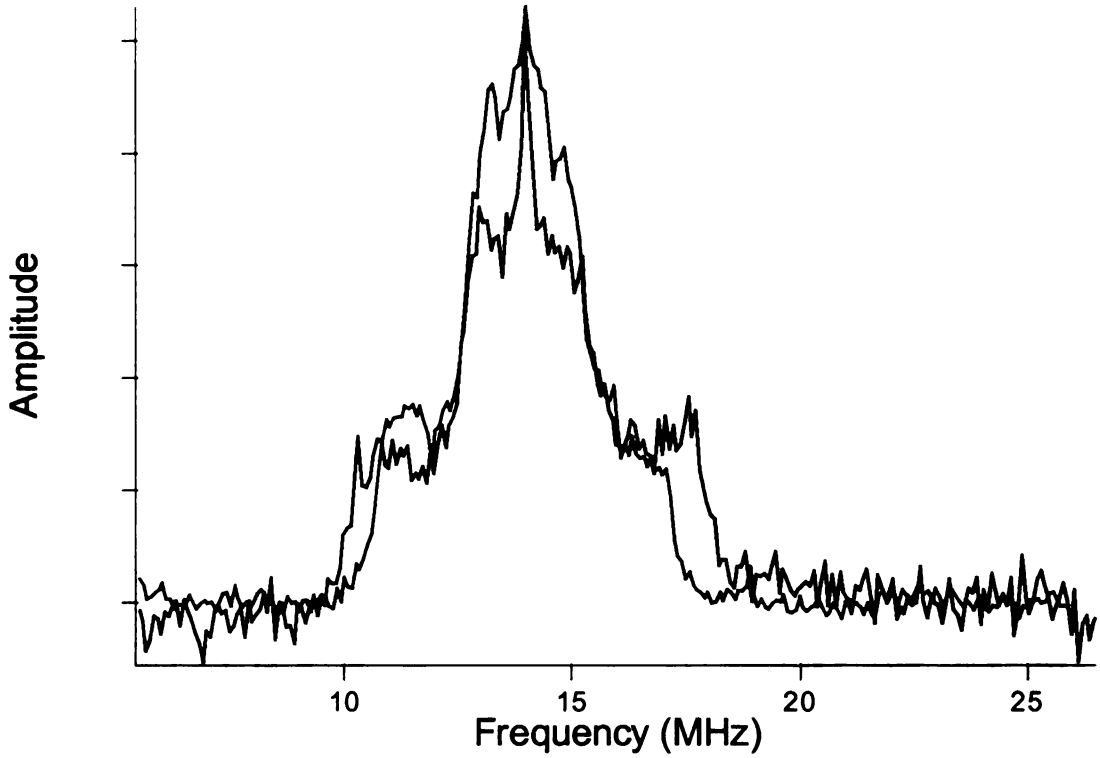

Figure 3.6: Davies ENDOR spectra of the oxidized (red) and the reduced (black) cytochrome *c* oxidase at central field 3.7kG. Oxidized protein sample is in 20mM HEPES-KOH, pH 7.4, 14mMKCl, and 0.1%lauryl maltoside buffer. The reduced protein sample in 100 mM HEPES-KOH buffer, 0.1% lauryl maltoside, at pH7.4 was made reducing the enzyme with dithionite with a final concentration of 25mM. ENDOR conditions: mw frequency, νe=9.72GHz; mw power, 20μW; π/2 and π mw pulse widths are 48ns and 96ns respectively; RF pulse width is 8000ns; τ= 400ns; T=40ns; srt=2000ns; signal averaging number 100; scan number n=25; temperature, 4.5K.

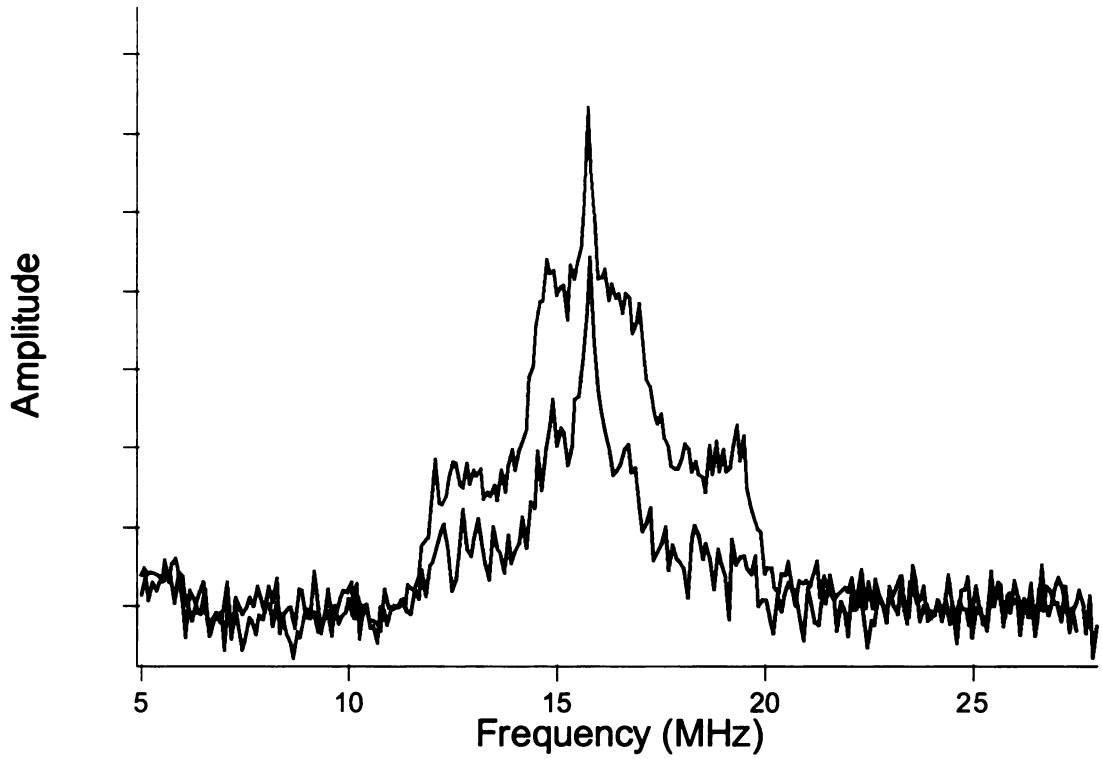

Figure 3.7: Davies ENDOR spectra of reduced cytochrome c oxidase in pH 7.4 water buffer (red) and 75% ^2H_2O buffer (black). Protein sample in H_2O is made in 100mM HEPES-KOH, pH 7.4, and 0.1%lauryl maltoside buffer and reduced by dithionite with a final concentration of 25mM. Protein sample in ^2H_2O is washed with ^2H_2O buffer of the same components as the water buffer several times to ensure the ^2H_2O level to at least 90%. ENDOR conditions: mw frequency, νe=9.72GHz; mw power, 20μW; π/2 and π mw pulse widths are 48ns and 96ns respectively; RF pulse width is 8000ns; τ= 400ns; T=40ns; srt=2000ns; signal averaging number 100; scan number n=25; temperature, 4.5K.

3.3 ENDOR simulation

To better understand the ENDOR spectra of the Mn in the C*c*O enzyme, it was useful to simulate ENDOR powder patterns with the purpose of predicting the positions of peaks and shoulders in the ENDOR spectrum. A series of trial simulations of ENDOR spectrum were performed using a Matlab-written program (Krzyaniak Matt.) with the procedures described in the method. The simulated powder pattern ENDOR spectrum matches well with the experimental data (**Fig.3.8**).

The protons around the Mn^{2+} site in C*c*O yielded the values of $A_{\|}$ and $A_{\perp}$ of 7.6MHz and –2.2MHz, respectively. From equations $A_{\|} = 2A_d + A_s$ and $A_{\perp} = A_s - A_d$, an isotropic coupling As =1.06MHz, and a dipolar coupling Ad = 3.26MHz were obtained. The $A_{\|}$ and $A_{\perp}$ values represent the averaged hyperfine coupling interactions from different protons within a certain distance range, ca. 5 Å.

4. Conclusion

The Davies ENDOR proves to be a powerful tool to provide hyperfine-coupling constants. The simulation of the overall ENDOR powder pattern yielded an isotropic coupling A_s=1.07MHz and a dipolar coupling A_d=3.27MHz, where $A_{||}=2A_d+A_s$ (7.6MHz) and $A_{\perp}=A_s-A_d$. (-2.2MHz). The major contribution to the hyperfine coupling is the through-space dipolar coupling to protons that are about 2.89Å from the Mn site. The estimated distance between Mn and protons is in the range of the distances between Mn and its inner-sphere protons (2.17~ 2.86 Å) revealed in 2.0Å X-ray crystal structure[11] and is close to the value of 2.8-2.9 Å observed using ^{1}H ENDOR in Mn hexaaquo complex[12].

The agreement between the estimated distance using simulated hyperfine coupling constants and the distance from crystal structure validated our simulation. The hyperfine coupling constants therefore would be good enough to be used in ESEEM simulation to quantify the number of protons bound to Mn site, which is the focus of the next chapter.

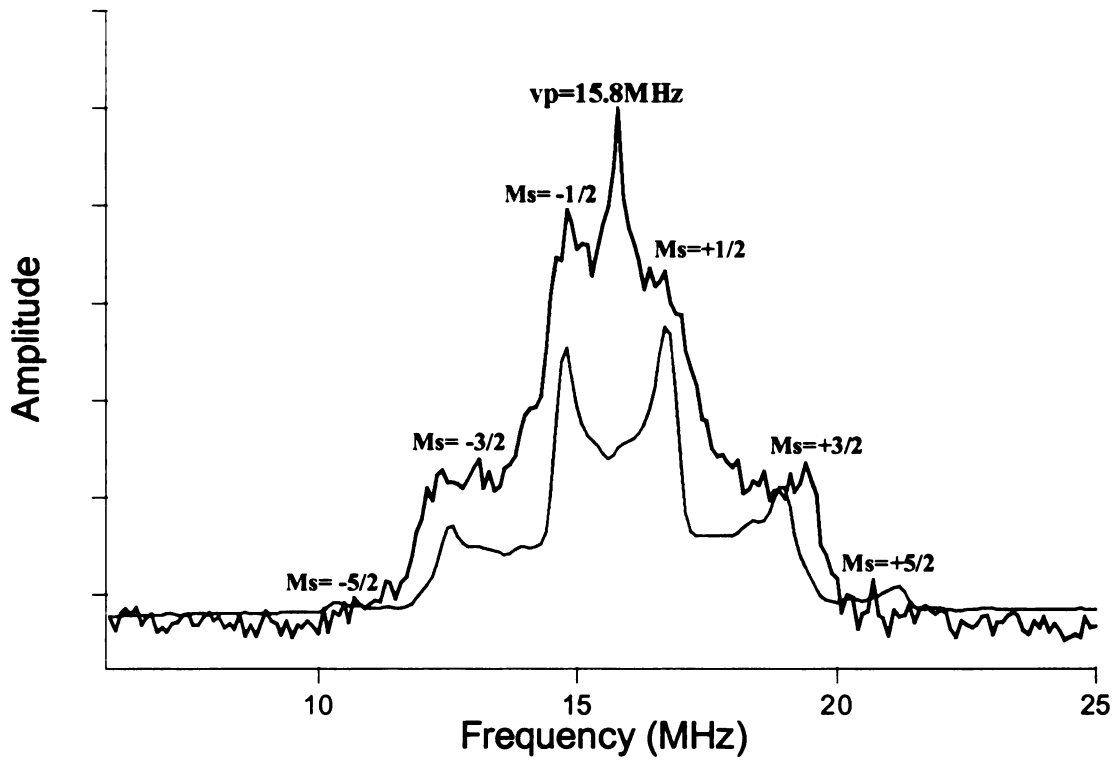

Figure 3.8: Experimental (black) and simulated (red) ENDOR powder pattern spectra at central field H=3.7kG. The simulation used $A_{||}$=7.6MHz and $A_{\perp}$=-2.2MHz

REFERENCES:

1. Tsukihara, T.; Aoyama, H.; Yamashita, E.; Tomizaki, T.; Yamaguchi, H.; Shinzawa-Itoh, K.; Nakashima, R.; Yaono, R.; Yoshikawa, S., The Whole Structure of the 13-Subunit Oxidized Cytochrome c Oxidase at 2.8 Å. *Science* **1996,** 272, 1136-1144.

2. Hosler, J. P.; Espe, M. P.; Zhen, Y.; Babcock, G. T.; Ferguson-Miller, S., Analysis of Site-Directed Mutants Locates a Non-Redox-Active Metal near the Active Site of Cytochrome *c* Oxidase of *Rhodobacter sphaeroides*. *Biochemistry* **1995,** 34, 7586-7592.

3. Florens, L.; Schmidt, B.; McCracken, J.; Ferguson-Miller, S., Fast deuterium access to the buried magnesium/manganese site in cytochrome c oxidase. *Biochemistry* **2001,** 40, (25), 7491-7497.

4. Schmidt, B.; McCracken, J.; Ferguson-Miller, S., A discrete water exit pathway in the membrane protein cytochrome c oxidase. *Proc Natl Acad Sci U S A* **2003,** 100, (26), 15539-42.

5. Tan, X. L.; Bernardo, M.; Thomann, H.; Scholes, C. P., Pulsed and Continuous Wave Electron Nuclear Double-Resonance Patterns of Aquo Protons Coordinated in Frozen Solution to High-Spin Mn2+. *Journal of Chemical Physics* **1993,** 98, (7), 5147-5157.

6. Reed, G. H. a. M., G. D., EPR of Mn(II) complexes with enzymes and other proteins. *Biological Magnetic Resonance* **1984,** 6, 73-142.

7. Hiser, C.; Mills, D. A.; Schall, M.; Ferguson-Miller, S., C-terminal truncation and histidine-tagging of cytochrome c oxidase subunit II reveals the native processing site, shows involvemet of the C-terminus in cytochrome c binding, and imporves the assay for proton pumping. *Biochemistry* **2001,** 40, 1606-1615.

8. Prisner, T.; Rohrer, M.; MacMillan, F., Pulsed EPR spectroscopy: Biological applications. *Annual Review of Physical Chemistry* **2001,** 52, 279-313.

9. Kass, H.; MacMillan, F.; Ludwig, B.; Prisner, T. F., Investigation of the Mn binding site in cytochrome c oxidase from Paracoccus denitrificans by high-frequency EPR. *Journal of Physical Chemistry B* **2000,** 104, (22), 5362-5371.

10. Kwiram, A. L., Endor Studies in Molecular Crystals .1. Glutaric Acid at 4.2 Degrees K. *Journal of Chemical Physics* **1971,** 55, (5), 2484-&.

11. Qin, L.; Hiser, C.; Mulichak, A.; Garavito, R. M.; Ferguson-Miller, S., Identification of conserved lipid/detergent-binding sites in a high-resolution structure of the membrane protein cytochrome c oxidase. *Proc Natl Acad Sci U S A* **2006,** 103, (44), 16117-22.

12. Hoogstraten, C. G.; Britt, R. D., Water counting: Quantitating the hydration level of paramagnetic metal ions bound to nucleotides and nucleic acids. *Rna-a Publication of the Rna Society* **2002,** 8, (2), 252-260.

Chapter 4

ELECTRON SPIN ECHO ENVELOPE MODULATION (ESEEM) STUDY OF WATER LIGANDS BOUND TO Mg/Mn SITE IN CYTOCHROME *C* OXIDASE

1. Introduction

Electron spin echo envelope modulation (ESEEM) spectroscopy is a very versatile technique. ESEEM spectra contain information on the strength of hyperfine coupling, the identity of the coupled nucleus, and the number of nuclei coupled to the electron spin. Because of this potential advantage, ESEEM has found many applications to paramagnetic centers having an electron spin S=1/2. However, for systems with S≥1, more attention has been paid to the analysis of spectral line positions and shapes than on analysis of modulation amplitude to quantify the number of coupled nuclei.

As one of the more abundant heavy metals in the earth's crust, Mn^{2+} can be found in many metalloenzymes as part of their active sites such as the photosynthetic complex, pyruvate kinase, superoxide dismutase. The ESEEM study of the Mn^{2+} sites in biological systems interests many spectroscopists. In C*c*O, the Mg site can be substituted by Mn^{2+} and studied by ESEEM method. ESEEM studies of Mn-C*c*O[1] indicated that a histidine was bound to the Mg/Mn site, which was confirmed later by the crystal structure. Further studies of fast deuterium access to the buried Mn^{2+}/Mg^{2+} site in C*c*O, combining ESEEM with rapid freeze quench (RFQ)[2], indicated that the water ligands of the Mn^{2+}/Mg^{2+} site, and the protons of these waters, can exchange with bulk solvent at a rate consistent with a role for this metal in product release during turnover. Because of the complexity of S=5/2 system, simulations of Mn(II) ESEEM spectra are rarely done. A relatively convenient way to quantify the number of waters coupled to the Mn site is to establish a standard curve for quantification. In the deuterium exchange study, Florens et al. used $Mn^{2+}(H_2O)_6$

as a standard to determine the number of exchanged water or protons. In their experiment, the standard curve was established by first obtaining the echo modulation of Mn^{2+} by one water ligand by taking the fifth root of the spectrum of $Mn^{2+}(H_2O)_6$ in 80% ^2H_2O and then raising the resultant spectrum to increase the power up to five. The single-dataset-generated standard curve introduced one problem that partly caused the estimation of two water ligands exchanged with deuterium at the Mn site, which was argued to be an underestimate. A better way to count the number of waters that are able to undergo deuterium exchange at the Mn site relies on both higher signal-to-niose ESEEM data and a more precise simulation program. Recently, Astashkin and Raitsimring[3] developed an ESEEM theory for a spin system with S>1/2 like Mn^{2+} that avoids some of the shortcomings of previous work [4, 5]. Using their simulation strategy together with information from X-ray crystal structures, we will use ESEEM spectroscopy to quantify ligand displacement chemistry at the Mn site.

Since the release of high-resolution crystal structures of C*c*O, a focus on the role of water in the facilitation of proton movement has prompted us to pay more attention to the Mg/Mn site, which bridges subunits I and II, shares one ligand with dinuclear Cu_A site, and is located in the vicinity of the aqueous region. Critical examination of bovine C*c*O crystal structures in oxidized and reduced states revealed two key water molecules, $W1_{Mg}$, which is in the sixth coordination position on Mg, and $W1_{E198}$, which is in the exit channel and appears to undergo protonation upon Cu_A reduction. In the oxidized enzyme both $W1_{Mg}$ and $W1_{E198II}$ are neutral water molecules (**Fig. 4.1A**). Upon Cu_A reduction, a proton movement is implied by the generation of H^+-$W1_{E198II}$, and a $^{(1-)}$OH ligated to

Mg^{2+} at the $W1_{Mg}$ position (**Fig. 4.1B**). To test the crystallographic observations and the implied hypothesis that the proton movement is one step in a redox-linked export of a pumped proton from the binuclear center into the exit pathway, cw EPR and ESEEM techniques were utilized to monitor the change in Mn cw EPR spectra and the change in number of protons coupled to the Mn site at different oxidation states, with or without the presence of extrinsic ligand, cyanide.

2. Experimental methods

2.1 Protein production and purification

The amount of Mn^{2+} incorporated into the protein depends on the [Mg] to [Mn] ratio in the growth medium[6]. The YZ-100 strain of *R. sphaeroides*, which over-expresses wild-type C*c*O with a histidine-tag added to the C-terminus of subunit I, was grown on "high Mn" medium (with $MnSO_4$ and $MgSO_4$ at final concentrations of 700μM and 50μM, respectively). The protein was purified by Ni^{2+}-NTA affinity chromatography and further purified by DEAE ion-exchange chromatography[7] to remove excess subunit I and the remaining contaminants. The procedure involves washing the protein with buffer containing 1mM EDTA to remove the adventitious free extrinsic Mn ions. The enzyme was then concentrated and washed into the desired buffer using a Millipore centrifugal filter with a MW (Molecular Weight) cut-off 100KDa. The visible spectral characteristics of Mg- and Mn-substituted wild-type enzymes were identical and oxygen consumption activities were not altered[6]. The visible spectrum of the purified enzyme showed that it

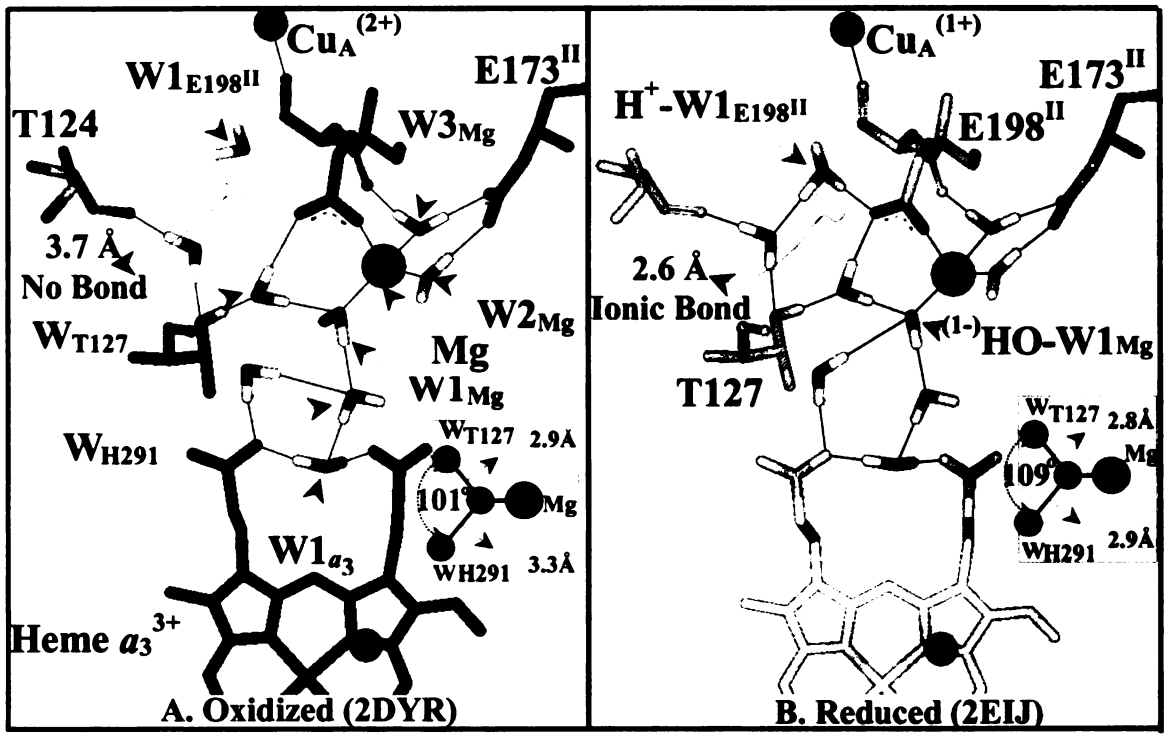

Figure 4.1: The formation of a hydroxide/hydronium pair upon Cu_A reduction; modeled on bovine oxidase oxidized and reduced structures. A comparison of the oxidized (A) and reduced (B) structures of bovine oxidase indicates a change in the protonation status and bonding of two water molecules: $W1_{E198^{II}}$ is HOH289 in the bovine 2DYR (Ox) and HOH291 in the bovine 2EIJ (Red) structures. The figure is a modification of a courtesy figure from Dr. Martyn Sharpe.

was in its fully oxidized form (see chapter 3 for the spectrum).

2.2 Sample preparation

Purified protein was mixed with buffers containing 20mM HEPES-KOH, 15mMKCl, 0.1% lauryl maltoside, at pH7.4 with varying levels of ^2H_2O, which resulted in final percentages of ^2H_2O ranging from 0% to 75% (v/v). Protein samples in different levels of ^2H_2O had the same final concentration of 36μM and were frozen in liquid nitrogen. A parallel series of protein samples with 0.4M sucrose as a glassing agent were also made. Reduced samples were made by adding 10 mM dithionite to samples which had been de-aerated using three vacuum/argon cycles. The buffer of the reduced samples was modified to contain100mM HEPES-KOH, 0.1% lauryl maltoside, at pH7.4 to buffer the acidification caused by adding the dithionite.

The model compound Mn^{2+}-DTPA was prepared with a slight excess of chelator in H_2O and different level of ^2H_2O, which also contained 0.4M sucrose. The $Mn^{2+}(H_2O)_6$ was prepared by dissolving $MnSO_4$ in H_2O and different level of ^2H_2O with 0.4M sucrose.

2.3 Electron Spin Echo Envelope Modulation (ESEEM) spectroscopy and Data Analysis

Pulsed measurements were made on a Bruker E-680X spectrometer operating at X band and equipped with a model ER 4118X-MD-X5-W1 probe that employs a 5mm dielectric resonator. The temperature was maintained at 4.5K using an Oxford instruments liquid helium flow system equipped with a CF-935 cryostat and an ITC-503

temperature controller. ESEEM data were collected using three-pulse (stimulated echo) with the sequence of 90°-τ-90°-T-90° and a 90° microwave pulse widths of 16 ns. τ was 204ns in all ESEEM measurements. An integration window of 24ns was used to acquire spin echo amplitude, and data set lengths were 512 points.

To determine the hydration level, three-pulse ESEEM was performed under such conditions that signals from protons are suppressed. The modulations in the ESEEM spectrum are from three sources: the magnetic nuclei from nearby residues, largely ^{14}N from histidine imidazoles; inner-sphere water deuterons; outer-sphere water deuterons and deuterons of the protein. Since the experimental modulation function is the product of all contributions, the contribution from ^{2}H nuclei can be isolated by using ratio method[8] in which the experimental data is divided by the data of control containing the unwanted contributions from sources such as the coordinating histidine. Individual ESEEM spectra were normalized by dividing each data set by its maximum amplitude. The normalized ^{2}H ESEEM data were then divided by the correspondingly normalized ^{1}H ESEEM data, resulting in ESEEM data dominated by the ^{2}H contribution to the ESEEM. These data were then tapered using a Hamming window function and subjected to a cosine Fourier transformation. The resulting ESEEM spectra were obtained by taking the absolute value of the transforms.

2.4 ESEEM simulation

For Mn(II) system, an approximate ESEEM theory was developed by Coffino and Peisach[4], and by Larson and Singel[5], However, in all their publications, authors were

focused on the spectral analysis without attempt to utilize , or compare the experimental intensities of spectral lines with theoretical evaluations. Recently, Astashkin and Raitsimring[3] revised and corrected the previous theory and derived new expressions for the ESEEM from high spin system Mn^{2+}. The simulation program used in this work is based on the original work done by Mims[9] with some modifications suggested by Astashkin and Raitsimring[3] in their paper. The program was written in Matlab by Matthew Krzyaniak (Michigan State University, Department of Chemistry).

3. Results

3.1 The use of cryoprotectant

Under cryogenic temperature (4.5K), a glassing agent or cryoprotectant is critical to preventing solute from segregation and other adverse effects. However, many cryoptotectants contain alcohol group that can occupy coordination site on metal ions, and therefore introduce errors in determining the number of waters bound to metal center. For instance, Halkides et al[10] found in their studies that glycerol, a commonly used cryoprotectant, ligates directly to the Mn^{2+} bound in the active site of P21-*ras* by displacing a water ligand. So the choice of cryoprotectant must be considered. Hoogstraten et al[11] demonstrated in their study of hydration level of the Mn^{2+} bound to nucleic acid and nucleotide that glycerol and ethylene glycol will occupy some of the inner-sphere coordination sites on the Mn^{2+} in aqueous solution, while sucrose or similar saccharide-based cryoprotectant are relatively safe choice for water counting purpose. In

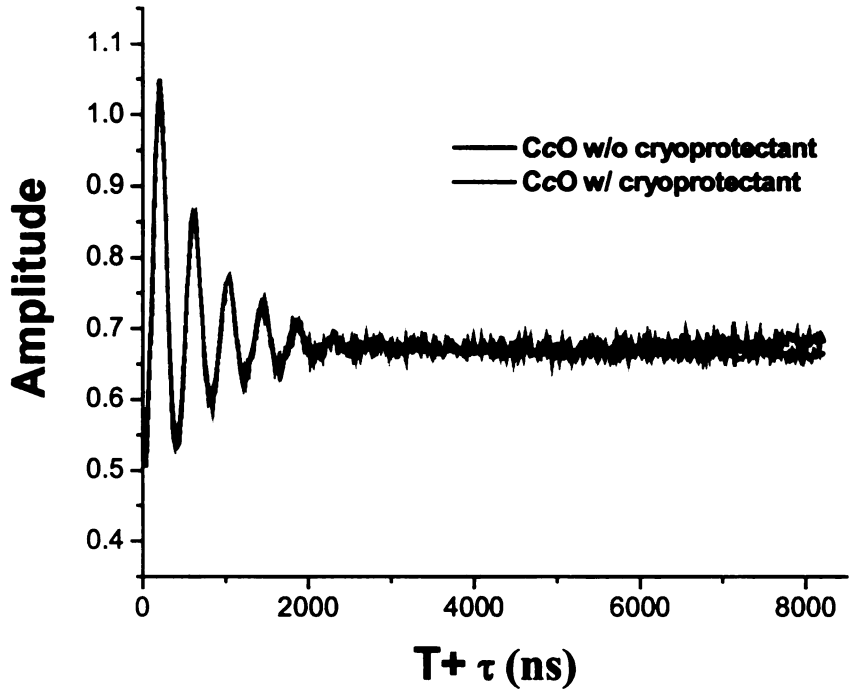

Figure 4.2: Effect of the cryoprotectant on *Cc*O three-pulse ESEEM data. The spectra are normalized and divided by 0% ^2H_2O control sample. Protein samples are made in 75% ^2H_2O level buffer with 20mM HEPES-KOH, pH 8.0,14mM KCl, and 0.1%lauryl maltoside with a final concentration of 36μM. Spectrometer conditions are: mw frequency, 9.72GHz; central field, 3.7kG; microwave power, 50mW; π/2 pulse width, 16ns; τ, 204ns; integration window, 24ns.

this study, 0.4M sucrose was added in $Mn^{2+}(H_2O)_6$ and Mn-DTPA samples. For the C*c*O samples, two parallel samples were made respectively with and without sucrose; ESEEM data showed no significant difference in modulation depth (**Fig.4.2**). This finding can be explained by the large size of the C*c*O protein sorrounding the Mn in which electron spins of the Mn^{2+} site are well segregated. But for better protection of the EPR sample tubes during freezing, a cryoprotectant was still used.

3.2 The deuterium standard curve for $Mn^{2+}(H_2O)_6$ and Mn-DTPA

$Mn^{2+}(H_2O)_6$ is octahedrally coordinated, having six inner sphere water molecules and a great number of outer-sphere water molecules. The deuterium modulation depth consists of contributions from both inner and outer-sphere waters. While in the Mn-DTPA complex, inner sphere binding sites are occupied by DTPA, resulting in only outer-sphere modulation depth in ESEEM spectrum. ESEEM modulation depth from pure inner-sphere water contribution can be determined by dividing Mn-DTPA modulation from $Mn^{2+}(H_2O)_6$ modulation.

The isolation of ^2H ESEEM from inner-sphere water ligands is demonstrated **in Fig.4.3A** which shows raw ESEEM data of $Mn(H_2O)_6$ in H_2O and ^2H_2O, along with the ^2H_2O /H_2O ratio. ^2Hs in the solvent give rise to strong modulations within about 500ns. **Fig.4.3B** shows the corresponding ESEEM curves for the Mn-DTPA complex, which does not have inner-sphere water ligands. **Fig.4.3C** shows the final processed modulation curve, representing pure inner-sphere bound water ESEEM in $Mn(H_2O)_6$ complex. There

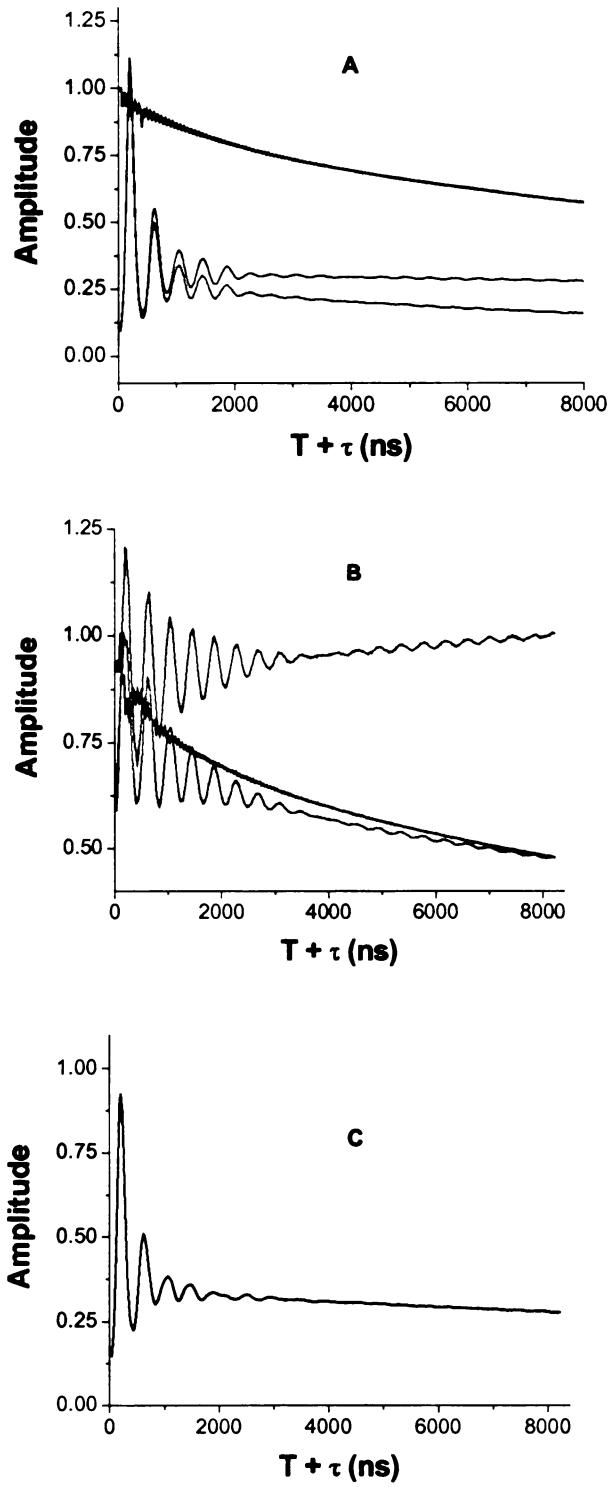

Figure 4.3: Three-pulse ESEEM time-domain data of $Mn(H_2O)_6$(A), Mn-DTPA (B), and $Mn(H_2O)_6$/ Mn-DTPA ratio (C). Samples in H_2O (blue line), D_2O (black line), and D/H ratio (red line). All the spectrometer conditions are the same as depicted in figure 4.2.

are two features worth mentioning: first, the comparison of the data for $Mn(H_2O)_6$ with the corresponding data for Mn-DTPA indicates that inner-sphere waters contribute about 70% ESEEM modulation, which is in good agreement with the literature[11]; second, the damping of the deuterium ESEEM from the difference spectrum, which contains only inner-sphere deuteron contribution, is very rapid which is expected because of the shorter distance of inner-sphere deuterons from the electron spin[12, 13].

3.3 ESEEM spectra of oxidized C*c*O in deuterated solvents with cryoprotectant

Similar studies were performed on Mn^{2+}-substituted C*c*O at 3.7kG. Ratios of modulation data remove contributions from ^{14}N from the histidine ligand to Mn (His411). Time-domain spectra of these samples showed pronounced modulations from deuteron hyperfine interactions and an increase in modulation depth as percentage of ^2H_2O was increased, indicating increased number of coupled deuteron nuclei (**Fig.4.4A**). The fairly rapid damping of the deuterium ESEEM suggests that the inner-sphere deuterons contribute predominantly to the ESEEM spectrum. The Fourier transformation of time-domain spectra results in the frequency domain spectra of all samples (**Fig.4.4B**). The frequency modulation at 2.42MHz is from coupled deuterons. Due to the use of proton suppression time, the proton modulation amplitude at 15.8MHz is minimized. The intensity of the 2.4MHz deuterium signal increased as the concentration of ^2H_2O was increased. A nearly linear relationship was observed between the echo modulation and the concentration of ^2H_2O. The data was fit with a linear function (**Fig.4.5**).

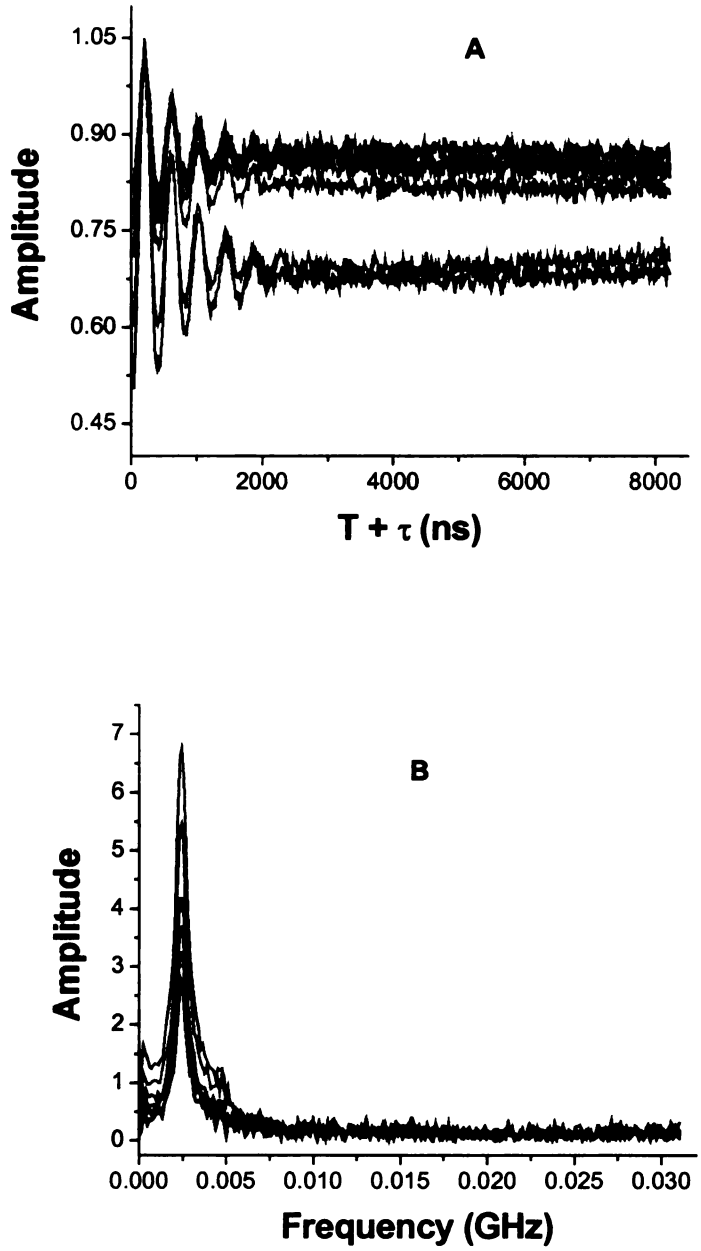

Figure 4.4: Three-pulse ESEEM time-domain spectra (A), frequency-domain spectra (B) of *Rs.* C*c*O in varying levels of ^2H_2O buffers ranging from 25% to 75% in the absence of cryoprotectant. Colors represent: black, 25% D_2O; red, 30% D_2O; cyan, 35% D_2O; purple, 40% D_2O; pink, 50% D_2O; green, 75%D_2O. Sample preparations and the ESEEM conditions are the same as depicted in figure 4.2.

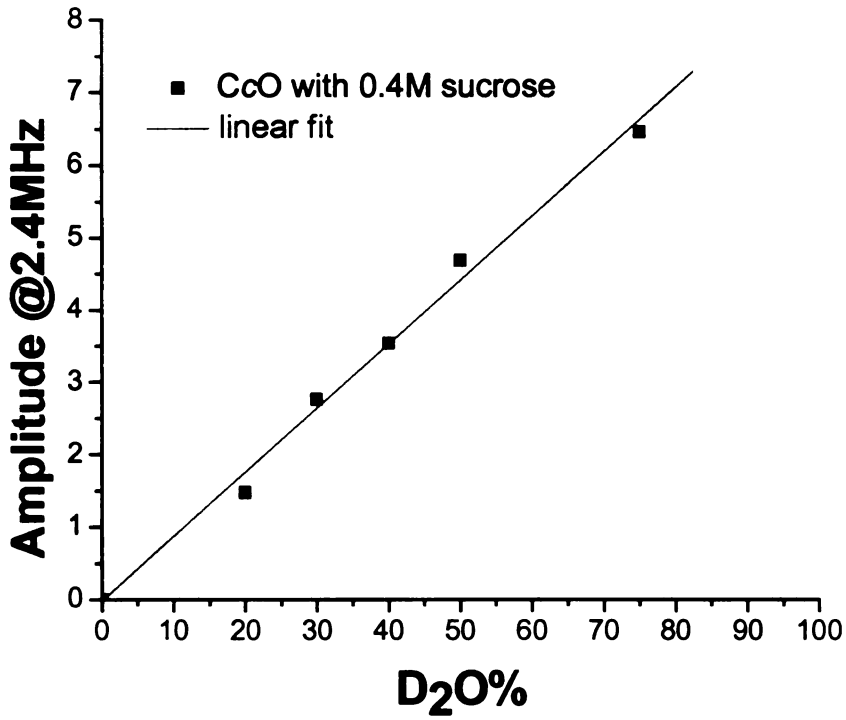

Figure 4.5: Fit of Fourier-transformed three-pulse ESEEM spectra of oxidized C*c*O in different concentration of ^2H_2O buffers with cryoprotectant with a linear function. The samples are made in the same way as described in figure 4.2. And the spectrometer conditions are the same as depicted in figure 4.2.

3.4 cw EPR and ESEEM studies of the oxidized and reduced C*c*O plus or minus cyanide

To test the hypothesis that $W1_{Mg}$ becomes a hydroxide in the reduced C*c*O, the enzyme was reduced and studied by cw EPR, **Figure 4.6** shows a comparison of the cw EPR spectra of reduced and oxidized *Rs.* C*c*O in the absence and presence of the externally added ligand, cyanide. Addition of cyanide to the oxidized enzyme had no effect on the line shape of the Mn EPR signal but did broaden the Mn lineshape in the reduced enzyme sample. This line shape change indicates that cyanide is perturbing the electronic structure of the Mn center.

ESEEM experiments were also carried out on the oxidized and reduced C*c*O plus or minus cyanide at 3.7kG. The time-domain spectra of the reduced C*c*O are similar to those of the oxidized enzyme. When the time-domain spectrum of the oxidized C*c*O plus cyanide is divided by the corresponding spectrum of the C*c*O without cyanide and then Fourier transformed, it is clear that there is no signals observed, which was consistent with the cw EPR data (**Figure 4.7A**). However, the same procedure for the reduced oxidase plus cyanide and reduced oxidase resulted in the observation of the modulation at 1.5MHz, 3.4MHz, and 5.2MHz, which can be assigned in part to perturbation of the nitrogen from the liganded histidine (**Figure 4.7B**).

The reduced C*c*O with and without cyanide in different percentages of ^2H_2O buffer were also studied by ESEEM. Plotting the peak amplitude at 2.42MHz versus ^2H_2O concentration and fitting with a linear function resulted in the similar relationship between echo amplitude and ^2H_2O concentration. When two plots of the reduced C*c*O

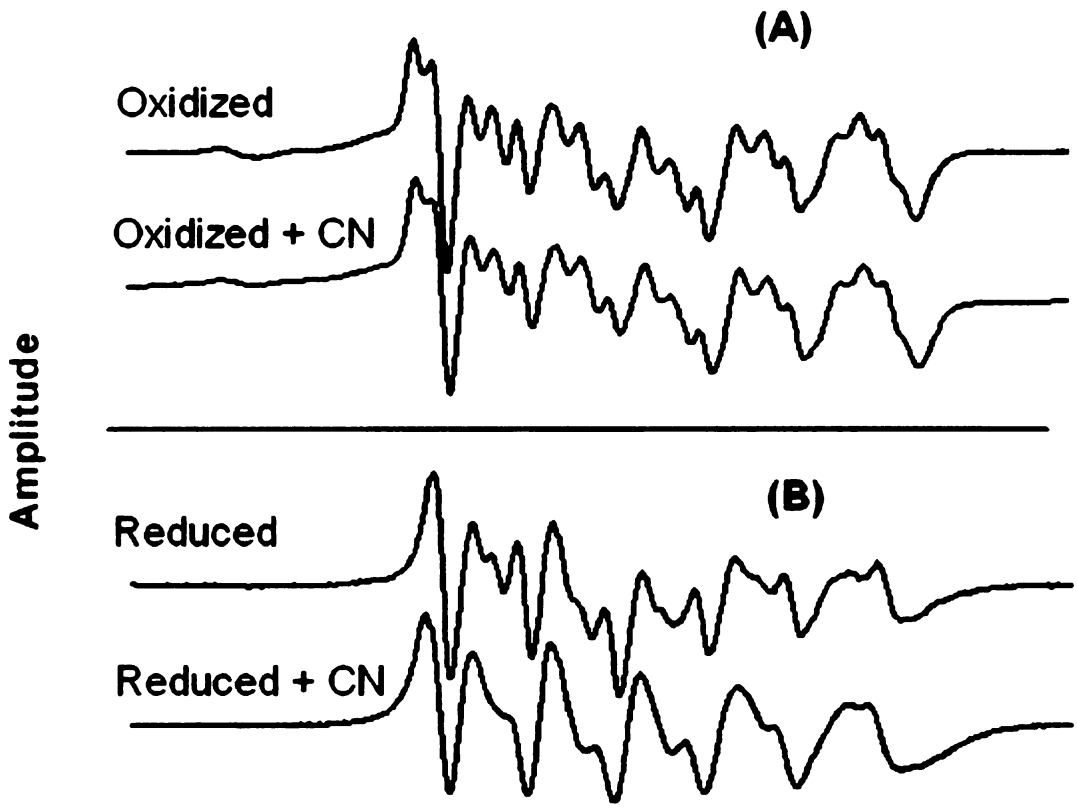

Figure 4.6: cw EPR spectra of oxidized and reduced CcO in the presence or absence of cyanide. The protein samples are in 20 mM HEPES-KOH, 4 mM KCl, pH 7.0 buffer with cyanide final concentration of 5 mM, and dithionite of 10 mM. The spectrometer conditions are: mw frequency, 9.46 GHz; mw power, 50 uW; modulation frequency, 100 kHz; modulation amplitude, 13.0 G; conversion time, 327ms.

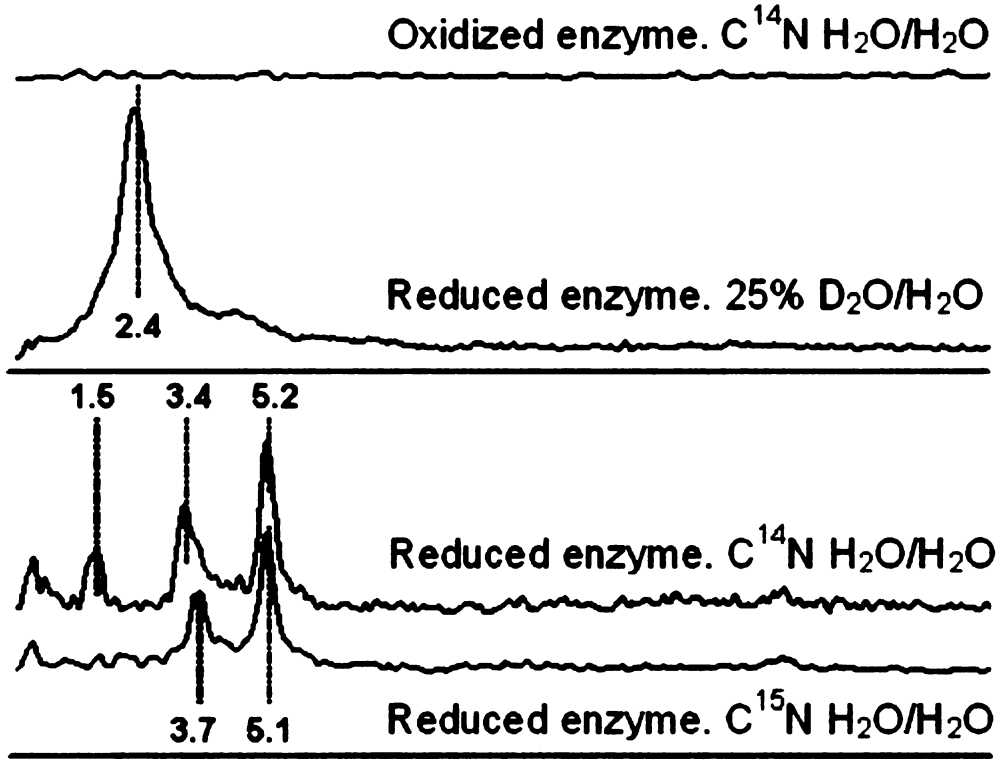

Figure 4.7 Effect of different radionucleotide of cyanide on the three-pulse ESEEM spectra of the Mn center of *R.s.* oxidase. The figure is a modification of the courtesy figure from Dr. Martyn Sharpe.

and the reduced C*c*O plus cyanide are put on the same axes for comparison, it is interesting to observe that the difference in slopes of two lines in **Figure 4.8** is approximately 9%. This difference could give us some insight into the change in deuteron number associated with the Mn^{2+} upon cyanide addition in the reduced enzyme.

3.5 ESEEM simulation

The ESEEM spectrum for C*c*O is simulated using the parameters obtained from simulation of the echo-detected EPR spectrum (see chapter 3 for the details): the relative weights of various electron spin transitions are 0.36 for $|-1/2> \leftrightarrow |+1/2>$, 0.20 for $|-3/2> \leftrightarrow |-1/2>$, 0.20 for $|+1/2> \leftrightarrow |+3/2>$, 0.12 for $|-5/2> \leftrightarrow |-3/2>$, and 0.12 for $|+3/2> \leftrightarrow |+5/2>$; the super hyperfine coupling parameters are $A_{\|}$=7.6MHz $A_{\perp}$= –2.2MHz for proton, $A_{\|}$=1.16MHz, $A_{\perp}$= –0.34MHz for deuteron. Because high spin Mn^{2+} has a nearly zero orbital angular momentum, the g value is usually treated as isotropic and has a value close to free electron g value. Due to the nearly spherical distribution of unpaired electrons about the ^{55}Mn nucleus, the ^{55}Mn hyperfine coupling is virtually isotropic except in highly distorted complexes.

The resultant simulated spectra assuming there are four, five or six deuterons in the inner sphere of the Mn^{2+} site are shown in **Figure 4.9**. Comparing the simulated spectrum with the experimental data, we can observe very good match in spectra between the simulated and the experimental in terms of the lineshape. The amplitude at deuteron Larmor frequency (2.42MHz) in the simulated spectrum, however, does not match that in

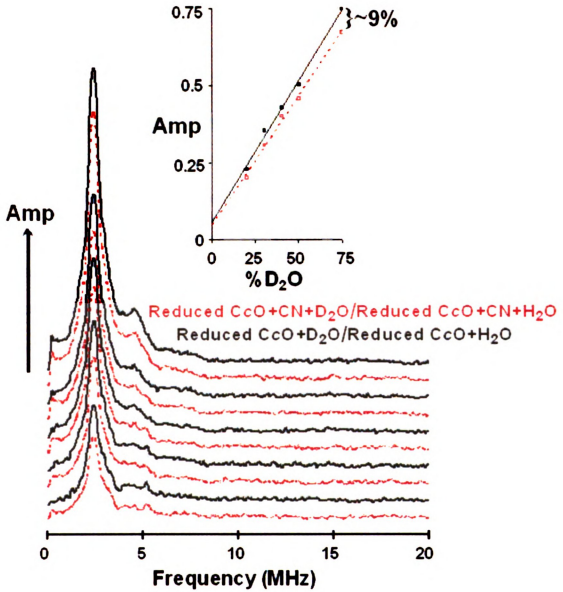

Figure 4.8: Plot of the amplitude at 2.42MHz versus ^2H_2O concentration for the reduced *Cc*O ratio and the reduced *Cc*O plus cyanide ratio. The figure is a modification of a courtesy figure from Dr. Martyn Sharpe.

the experimental spectrum, assuming there are three water molecules bound to the Mn site (**Figure 4.10**).

4 Discussion

Previous ESEEM studies of C*c*O were more focused on the analysis of the modulation frequency. In an ESEEM study, C*c*O was incubated in buffered ^2H_2O under resting or turnover conditions for 90 minutes and then frozen for experiments[14]. The observation of the deuteron Larmor frequency in ESEEM data provided an indication that the deuterium was introduced into the Cu_A environment. A further ESEEM study of the Mn site[1] in C*c*O provided direct evidence for a nitrogen ligand bound to the Mn site and assigned this nitrogen to a histidine ligand, which was later confirmed by crystal structures[15]. One attempt to use modulation amplitude was made by Schmidt et al. [16] who studied the deuterium exchange at the Mn^{2+} site in C*c*O and estimated the number of bound water ligands based on the analysis of deuteron modulation amplitude. This attempt proved to be a pretty successful trial but can be improved with a higher sensitivity instrument and better simulation program.

Examination of recent crystallographic data[17, 18] revealed that the reduced C*c*O structure appeared to have a hydronium ion close to the Cu_A-Mn pair $W198_{II}$ and that one of the water ligands of Mn, $W1_{Mg}$, was deprotonated. This suggested that a proton could be cycling between $W198_{II}$ and $W1_{Mg}$ as a function of the redox state of the enzyme, playing a role in proton pumping. Experiments with cw EPR showed a perturbed Mn spectrum when cyanide was added to the reduced C*c*O, but had no effect on the oxidized

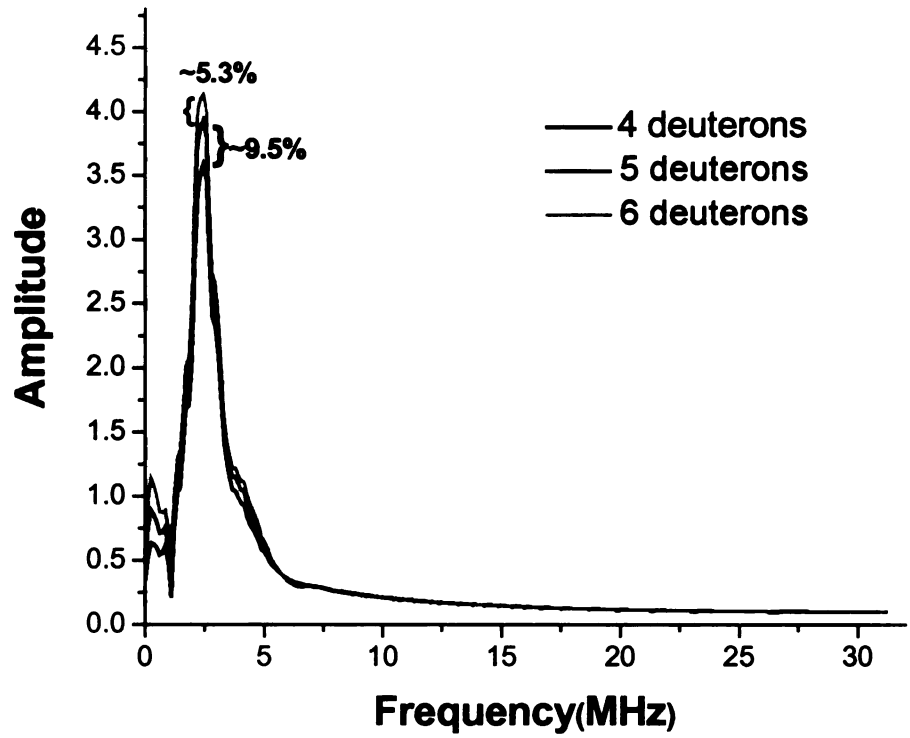

Figure 4.9: The ESEEM simulated spectra of C*c*O assuming different numbers of deuterons bound to the Mn site. The ESEEM simulation conditions are: central field, 3700G; mw frequency, 9.72GHz; starting T, 40ns; tau, 204ns; T increment, 16ns; Axx, Ayy for deuteron, -0.34MHz, and Azz, 1.16MHz. The relative weights of these transitions: 0.36 for |-1/2> ↔ |+1/2>, 0.20 for |-3/2> ↔ |-1/2>, 0.20 for |+1/2> ↔ |+3/2>, 0.12 for |-5/2> ↔ |-3/2>, and 0.12 for |+3/2> ↔ |+5/2>.

enzyme as predicted if cyanide could substitute for hydroxide. Because of its sensitivity to the change in ligand environment, ESEEM is used to monitor the change in ligands. Both cw EPR and ESEEM data showed that the extrinsic ligand cyanide could bind to the Mn site when Cu_A was reduced. In the reduced crystal structures, one of three water ligands of the Mn site appears to be deprotonated, giving a hydroxide ion ligand. This predicts a negatively charged cyanide ligand could replace it, as observed. In the oxidized enzyme, no cyanide binding was detected by ESEEM. Modulation amplitude analysis of the reduced and the reduced C*c*O plus cyanide indicated that a drop of about 9% in intensity at deuteron modulation was caused by the binding of the cyanide. With the help of the crystal structures, it is calculated that if one of three water ligands is a hydroxide, then five inner sphere deuterons are expected. If the hydroxide is replaced by a cyanide, a decrease of one out of five deuterons is expected, corresponding to a 9.5% decrease in signal intensity. The closeness between the experimental data and the theoretical calculation make it reasonable to conclude that cyanide replaces a hydroxide ligand to Mn in the reduced enzyme, but cannot displace the aqueous ligand present in the oxidized enzyme.

ESEEM data indicates that the difference in modulation amplitude is due to the displacement of a hydroxide ion by a cyanide ion, and supports the hypothesis that the reduction of the Cu_A caused one of the water ligands of the Mn to become a hydroxide ion. The cycling between water and hydroxide ion of Mg water ligand could play an important role in proton transfer upon change in electron density on Cu_A. A role for the Cu_A/Mg site in proton movements could represent an important part of the proton exit

mechanism. Further experiments are needed to better explore this interesting possibility, proposed by Dr. Sharpe, M. et al. (paper submitted)

Finally, the simulation we used to help determine the number of water, turned out to be more complicated than we thought. The simulated spectrum successfully matches in lineshape with the experimental data but did not exactly match the intensity of the modulation (**Figure 4.10**). This discrepancy in amplitude could be explained in several reasons: first, the way we ratio the data may cause the loss of some spectroscopic information although it effectively simplifies the spectrum; second, according to our study, the six inner sphere deuterons in the simulated spectrum only represents about 70% of the echo amplitude and the contributions from out sphere deuterons were not considered in the simulation; third, to simulate such complicated spin systems as Mn^{2+} is not a trivia task: assumptions and simplifications in the simulation procedure make it inevitable that the simulation is only an approximation.

Interestingly, the simulation program we used to monitor the change in modulation amplitude upon the change in coupled nuclei provided us with good results. It is found that when the number of coupled deuterons changed from five to four, the modulation amplitude decreased by 9.5%, which agrees well with experimental data, in which the decrease is 9.0%. When the number of deuterons changed from six to five, the modulation amplitude decreased by 5.3%. A total change in modulation amplitude was observed to be 15.3% for deuterons change from six to four. The agreement of simulated data with experimental data proved to be useful in estimating the change in relative

numbers of coupled nuclei during the reaction and may be a good tool to help us understand better the proton movements.

Note: Previous work done by Kass et al.[19] indicated the Cu_A in the oxidized enzyme dipolar coupled with the Mn site and affected the EPR characteristics of Mn site. Because of this spin-spin interaction, the ligand field of Mn is somewhat altered. This interaction may affect the deuterium modulation in such a complicated manner that it is not very useful to compare the deuterium echo amplitude in oxidized and reduced enzyme in ESEEM experiments (**see Figure 4.11**). This explained why we carry out more complicated cyanide experiments in the reduced enzyme instead of just comparing the oxidized and reduced enzyme to test the hypothesis.

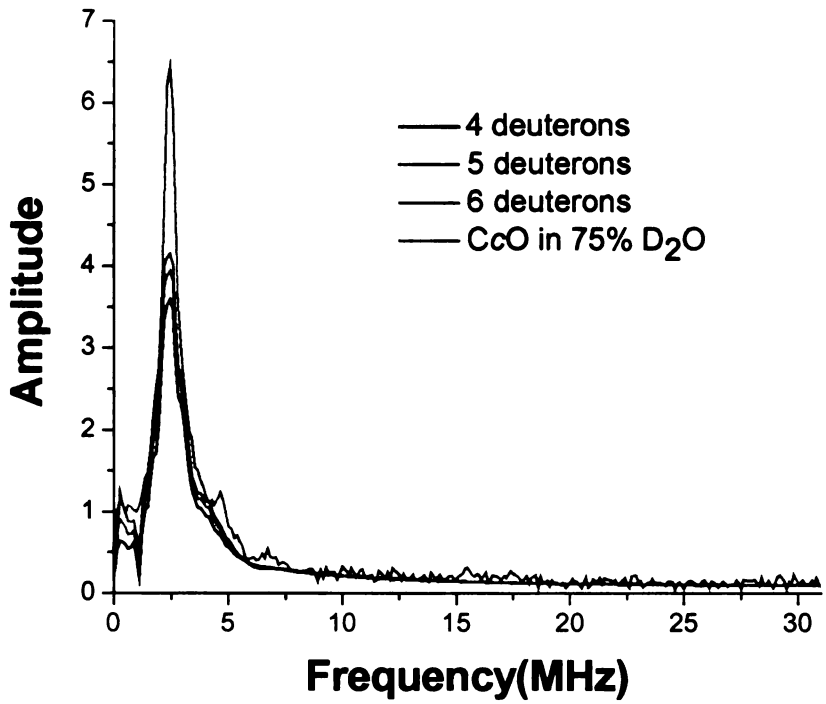

Figure 4.10: Comparison of the simulated and the experimental data. The experimental data is the C*c*O in 75%(v/v) $^{2}H_2O$. The sample and spectrometer conditions are depicted in figure 4.2

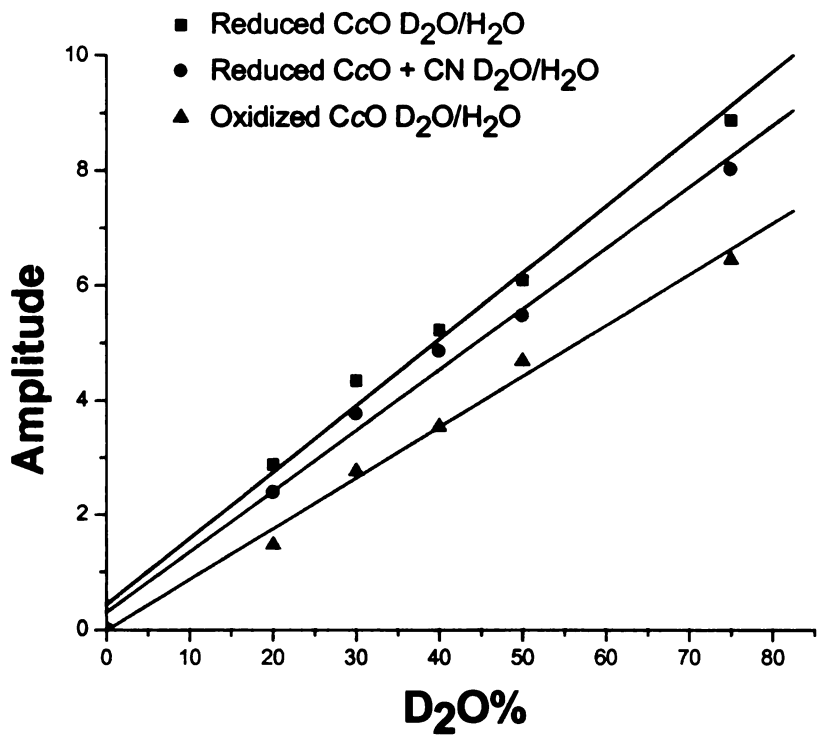

Figure 4.11: Plots of the amplitude at 2.42MHz versus ^2H_2O concentration for the oxidized C*c*O ratio, reduced C*c*O ratio and the reduced C*c*O plus cyanide ratio

REFERENCES:

1.Espe, M. P.; Hosler, J. P.; Ferguson-Miller, S.; Babcock, G. T.; McCracken, J., A Continuous Wave and Pulsed EPR Characterization of the Mn^{2+} Binding Site in *Rhodobacter sphaeroides* Cytochrome *c* Oxidase. *Biochemistry* **1995,** 34, 7593-7602.

2.Florens, L.; Schmidt, B.; McCracken, J.; Ferguson-Miller, S., Fast deuterium access to the buried magnesium/manganese site in cytochrome c oxidase. *Biochemistry* **2001,** 40, (25), 7491-7497.

3.Astashkin, A. V.; Raitsimring, A. M., Electron spin echo envelope modulation theory for high electron spin systems in weak crystal field. *Journal of Chemical Physics* **2002,** 117, (13), 6121-6132.

4.Coffino, A. R.; Peisach, J., Nuclear Modulation Effects in High-Spin Electron-Systems with Small Zero-Field Splittings. *Journal of Chemical Physics* **1992,** 97, (5), 3072-3091.

5.Larsen, R. G.; Halkides, C. J.; Singel, D. J., A Geometric Representation of Nuclear Modulation Effects - the Effects of High Electron-Spin Multiplicity on the Electron-Spin Echo Envelope Modulation Spectra of Mn-2+ Complexes of N-Ras P21. *Journal of Chemical Physics* **1993,** 98, (9), 6704-6721.

6.Hosler, J. P.; Espe, M. P.; Zhen, Y.; Babcock, G. T.; Ferguson-Miller, S., Analysis of Site-Directed Mutants Locates a Non-Redox-Active Metal near the Active Site of Cytochrome *c* Oxidase of *Rhodobacter sphaeroides. Biochemistry* **1995,** 34, 7586-7592.

7.Hiser, C.; Mills, D. A.; Schall, M.; Ferguson-Miller, S., C-terminal truncation and histidine-tagging of cytochrome c oxidase subunit II reveals the native processing site, shows involvemet of the C-terminus in cytochrome c binding, and imporves the assay for proton pumping. *Biochemistry* **2001,** 40, 1606-1615.

8.Mims, W. B.; Davis, J. L.; Peisach, J., The Exchange of Hydrogen-Ions and of Water-Molecules near the Active-Site of Cytochrome-C. *Journal of Magnetic Resonance* **1990,** 86, (2), 273-292.

9.Mims, W. B., Envelope Modulation in Spin-Echo Experiments. *Physical Review B* **1972,** 5, (7), 2409-&.

10.Halkides, C. J.; Farrar, C. T.; Singel, D. J., The effects of cryoprotection on the structure and activity of p21 ras: Implications for electron spin-echo envelope modulation spectroscopy. *Journal of Magnetic Resonance* **1998,** 134, (1), 142-153.

11.Hoogstraten, C. G.; Britt, R. D., Water counting: Quantitating the hydration level of paramagnetic metal ions bound to nucleotides and nucleic acids. *Rna-a Publication of the Rna Society* **2002,** 8, (2), 252-260.

12.Mims, W. B.; Davis, J. L.; Peisach, J., The accessibility of type I copper(II) centers in laccase, azurin, and stellacyanin to exchangeable hydrogen and ambient water. *Biophysical Journal* **1984,** 45, 755-766.

13.Mccracken, J.; Peisach, J.; Dooley, D. M., Cu(Ii) Coordination Chemistry of Amine Oxidases - Pulsed Electron-Paramagnetic-Res Studies of Histidine Imidazole, Water, and Exogenous Ligand Coordination. *Journal of the American Chemical Society* **1987,** 109, (13), 4064-4072.

14.Hansen, A. P.; Britt, R. D.; Klein, M. P.; Bender, C. J.; Babcock, G. T., Endor and Eseem Studies of Cytochrome-C-Oxidase - Evidence for Exchangeable Protons at the Cu(a) Site. *Biochemistry* **1993,** 32, (49), 13718-13724.

15.Tsukihara, T.; Aoyama, H.; Yamashita, E.; Tomizaki, T.; Yamaguchi, H.; Shinzawa-Itoh, K.; Nakashima, R.; Yaono, R.; Yoshikawa, S., The Whole Structure of the 13-Subunit Oxidized Cytochrome c Oxidase at 2.8 Å. *Science* **1996,** 272, 1136-1144.

16.Schmidt, B.; Hillier, W.; McCracken, J.; Ferguson-Miller, S., The use of stable isotopes and spectroscopy to investigate the energy transducing protein cytochrome *c* oxidase. *Biochimica et Biophysica Acta* **2003,** *In press.*

17.Shinzawa-Itoh, K.; Aoyama, H.; Muramoto, K.; Terada, H.; Kurauchi, T.; Tadehara, Y.; Yamasaki, A.; Sugimura, T.; Kurono, S.; Tsujimoto, K.; Mizushima, T.; Yamashita, E.; Tsukihara, T.; Yoshikawa, S., Structures and physiological roles of 13 integral lipids of bovine heart cytochrome c oxidase. *Embo Journal* **2007,** 26, (6), 1713-1725.

18.Muramoto, K.; Hirata, K.; Shinzawa-Itoh, K.; Yoko-O, S.; Yamashita, E.; Aoyama, H.; Tsukihara, T.; Yoshikawa, S., A histidine residue acting as a controlling site for dioxygen reduction and proton pumping by cytochrome c oxidase. *Proceedings of the National Academy of Sciences of the United States of America* **2007,** 104, (19), 7881-7886.

19.Kass, H.; MacMillan, F.; Ludwig, B.; Prisner, T. F., Investigation of the Mn binding site in cytochrome c oxidase from Paracoccus denitrificans by high-frequency EPR. *Journal of Physical Chemistry B* **2000,** 104, (22), 5362-5371.

CHAPTER 5

HIGH FIELD/FREQUENCY CW EPR STUDY OF Mn (II) IN CYTOCHROME *C* OXIDASE

1.Introduction

High spin mononuclear Mn^{2+} sites are found in many active sites of metalloenzymes. The most commonly used method to study Mn complexes is by EPR spectroscopy, since the EPR properties of Mn^{2+} are governed by the shape of the magnetization in a given coordination environment. It is known that the shape of the magnetization is determined by the distribution of unpaired electrons around the Mn nucleus, and this distribution is related to the types of ligands present and their geometrical arrangement about the ion. The interpretation of the structural message encoded in the EPR spectrum is a major part of this study.

High spin Mn ion (d^5) is characterized by an electron spin S=5/2 and nuclear spin I=5/2. Its electronic properties can be described by the following spin Hamiltonian:

$$He = g_e\beta_e \mathbf{H} \bullet \mathbf{S} + A\mathbf{I} \bullet \mathbf{S} + D\,[S_z^2 - 1/3S(S+1)] + E\,(S_x^2 - S_y^2) \qquad 5.1$$

where the first two terms represent the electron Zeeman and the isotropic electron-nuclear hyperfine interaction, respectively, whereas the last two terms are the zero-field splitting (zfs) interaction. The zfs parameters D, and E, provide insight into the symmetry of Mn^{2+}coordination. Larger D and E parameters means lower symmetry. For Mn (S=5/2), there are five fine structure transitions arising from transitions between Ms= ±5/2, ±3/2, and ±1/2. Each of these transitions is split into six lines from hyperfine coupling to the Mn nucleus (I=5/2). The total allowed transitions is thirty. The energies of Ms= ±5/2, ±3/2 are dependent on D and E to the first order and are angle-dependent; therefore, in an orientationally-disordered system, the intensities of the EPR transitions from Ms= ±5/2,

±3/2 are weak and hard to observe. By contrast, the energies of Ms= ±1/2 have a very small angular dependence, thus it has more intense EPR signals. In C*c*O, most of the EPR signals are from Ms= ±1/2 transitions. In addition to allowed EPR transitions, there are some forbidden ($\Delta m_I = \pm 1$) EPR transitions. These forbidden transitions have less intensity and depend inversely on the magnetic field. The majority of the EPR work on Mn complexes and enzymes has been done with the X-band (9.5GHz) or Q-band (35GHz) frequencies. But using EPR with a higher magnetic field strength will greatly simplify the EPR spectrum and improve the resolution.

A non-redox-active Mg site is located at an aqueous region, observed in the crystal structure[1], which suggests that it may be involved in proton/water exit. The substitution of Mg by Mn does not affect its function but opens a door for the investigation of this site by EPR[2]. Previously, studies of the Mn site in C*c*O provided some intriguing results. In the deuterium-exchange experiments[3], the results indicated that the ligands of the Mg/Mn site in C*c*O could exchange with the bulk solvent at a fast rate (>3000s^{-1}). In a $H_2{}^{17}O$ exchange experiment, Mn cwEPR spectra were broadened upon water exchange. Additional evidence of ^{17}O presence near the Mn site is given by the observation of the ^{17}O Larmour frequency in the ESEEM spectrum, during the catalytic reaction, with limited turnover in the rapid freeze quench apparatus, with $^{17}O_2$ as the substrate instead of regular oxygen gas. The observed line-broadening of the Mn EPR spectrum indicated that the product waters were bound to the Mn site[4]. It was noticed that the oxidation state of Cu_A was not indicated in the turnover experiment, although it is most likely in its oxidized form. EPR experiments showed that the oxidation state of Cu_A slightly affects

the Mn spectra in the literature[5]. The difference in spectra was interpreted as a conformational change which occurred in C*c*O near the Mg site upon a change in the oxidation state of Cu_A[6]. Investigations of the Mn/Mg site in *Rs.*C*c*O by cw EPR and ESEEM concluded that the difference in the Mn EPR spectra was so small that the geometry of Mn was barely altered by the change in oxidation states of Cu_A[2, 7]. In 2000, Prisner and coworkers reinvestigated the Mn site in *Pd.*C*c*O using high-field EPR (W-band, 95GHz) and concluded that the splitting of the Mn sextet spectrum was due to a dipolar coupling interaction present between Cu_A and Mn and this interaction vanished when the Cu_A site was reduced. The difference in the Mn EPR spectra was attributed to the dipolar coupling interaction between two spin centers[8]. Now, with the high field (HF) EPR machine, the Mn site in oxidized and reduced C*c*O is reinvestigated to see if similar difference in spectra could also be observed in *Rs.*C*c*O. The possible cause behind the difference in the Mn spectra is also discussed. Besides exploring the origin of the observed difference in C*c*O under oxidized and reduced conditions, it is possible that it could be applied to isotope-labeled water-exchange experiments, using HF-EPR to study the ligation environment of Mn in C*c*O.

The hyperfine coupling from ^{17}O (I= 5/2) has been used in EPR investigations of many metalloenzymes to identify ligands for the paramagnetic metal center[9]. Reed and coworkers[10, 11] have developed a useful scheme to determine the number of inner sphere waters of the Mn^{2+} ion by an EPR technique. The method relies on the detection of hyperfine coupling between the unpaired electron spins of Mn^{2+} and the magnetically active nuclei of ligand atoms. The magnitude of the hyperfine coupling between Mn^{2+}

and ^{17}O is smaller compared to the intrinsic line widths caused by other sources of broadening—primarily unresolved ^{1}H hyperfine coupling interactions and dipolar coupling from Cu_A in the oxidized enzyme[8] and second-order fine structure broadening due to zero-field splitting. As a result, the broadening from ^{17}O hyperfine coupling to the EPR signals is difficult to resolve, especially at lower field such as X-band. Since the second-order fine structure broadening is inversely proportional to the field strength, $\mathbf{B_0}$, while hyperfine broadening is independent of $\mathbf{B_0}$, it is obviously more advantageous to do ^{17}O-labeling experiments at higher field.

Advances in high-field EPR enable the investigation of paramagnetic metal ions with $S \geq 1$ and $I \geq 1$, such as Mn^{2+}, for the following reasons: first, a simplified spectrum can be achieved due to the reduction of contributions from second-order fine structure broadening; second, the intensities of forbidden transitions are reduced in high field; third, orientation selectivity can be improved in disordered systems; and fourth, more-precise and more complete information about the system under study can be obtained because of dramatic decrease in cross-relaxation of the paramagnetic center.

Here, in this chapter, the EPR spectra for C*c*O are used to determine the hydration number of Mn^{2+} by ^{17}O hyperfine coupling interactions. Protein samples including: oxidized state, and dithionite-reduced state, in different solvents with ^{2}H and ^{17}O-enrichment were made and studied under W-band (95GHz) EPR.

2. Experimental methods

2.1 Protein production and purification

The amount of Mn^{2+} incorporated into the protein depends on the [Mg] to [Mn] ratio in the growth medium[2]. The YZ-100 strain of *R. sphaeroides*, which over-expresses wild-type C*c*O with a histidine-tag added to the C- terminus of subunit I, was grown on "high Mn" medium (with $MnSO_4$ and $MgSO_4$ at final concentrations of 700μM and 50μM, respectively). The protein was purified by Ni^{2+}-NTA affinity chromatography and further purified by DEAE ion-exchange chromatography[12] to remove excess subunit I and the remaining contaminants. The procedure involves washing the protein with buffer containing 1mM EDTA to remove the adventitious free extrinsic Mn ions. The enzyme was then concentrated and washed into the desired buffer using a Millipore centrifugal filter with a MW cut-off 100KDa. The visible spectral characteristics of Mg- and Mn-substituted wild-type enzymes were identical and oxygen consumption activities were not altered.

2.2 UV-visible spectroscopy

UV-visible spectra of as-purified and dithionite-reduced proteins were recorded on a Perkin-Elmer Lamda 40P spectrophotometer scanning wavelengths from 400nm to 750nm after appropriate dilution into pH7.4 100mM HEPES, 0.1% lauryl maltoside. From the visible spectrum, the purified oxidase is in its fully oxidized state (See spectrum in chapter 3).

2.3 Sample preparation

Approximately 50μM, 200nL each of the oxidized, and the dithionite-reduced wild-type Mn (II) substituted C*c*O was transferred to silica-fused capillary sample tubes with id. 0.40mm and od. 0.55mm (Bruker), which were sealed with silicone high vacuum grease (Bruker). Another two aliquots of reduced enzyme were mixed with 100% ^{2}H-enriched and 40% ^{17}O-enriched water (Cambridge Isotope Laboratories), resulting in 80% ^{2}H and 30% ^{17}O enrichment in the final samples respectively. The samples were then sealed again.

2.4 W-band EPR spectroscopy

W-band cw-EPR spectra were recorded using a commercial W-band EPR spectrometer (Bruker Elexsys E680) equipped with a helium flow Oxford CF935 cryostat, a cylindrical Bruker Teraflex TE110 cavity, and a 6T Magnex superconducting magnet. The microwave frequency was measured with the internal Bruker counter. Both oxidized and reduced samples were investigated in a temperature range from 4.2 to 120K. The EPR parameters were as follows: microwave frequency 94.0 GHz; microwave power 15.8μW; field modulation amplitude 1G; modulation frequency 10KHz; time constant 327ms.

2.5 Strategy for determination of the number of inner sphere waters

Since the ^{17}O has a spin of 5/2, the hyperfine coupling between $H_2{}^{17}O$ ligand(s) and the Mn^{2+} center would split each EPR transition into six approximately equally spaced components, resulting in a broadening of the EPR spectrum. In order to extract the coordination information out of the EPR spectrum, Reed and coworkers developed the

subtraction method[10, 11]. The highest ^{17}O-enriched water available is 40%. Therefore, the signals observed for a sample containing ^{17}O-enriched ligand are a superposition of spectra for enzyme with Mn coordinated to ^{17}O and to other oxygen isotopes. The experimental spectrum, Se, is a weighted sum of n+1 subspectra (assume there are n spectroscopically equivalent $H_2{}^{17}O$ ligands on the Mn^{2+} site). And the difference spectrum, S_d, has the form of $S_d = S_e - F_nS_u$ (S_u represents the spectrum without ^{17}O enrichment and F_n is the adjustable factor between 0 and 1). By trying different F_n, a series of difference spectra are obtained. Only the difference spectrum that does not have extraneous features is useful in providing the hydration number.

If the water ligand is exchanged to ^2H_2O buffer, a narrowing spectrum will be expected, due to the very small g_n of deuterium. The narrowing effects can be potentially used to determine the hydration level of Mn^{2+} too.

3. Results and discussion

3.1 EPR spectra of C*c*O in H_2O

Fig.5.1 shows the W-band spectra of oxidized and reduced C*c*O at 15K. The reduced C*c*O exhibited a typical Mn^{2+} sextet hyperfine pattern centered at the g=2.0 region with an averaged splitting of 94.12G. For the oxidized C*c*O, each line of the sextet was split up by more than 15G. Temperature-dependence experiments from 15K to 120K were also performed. The reduced C*c*O did not show a temperature-dependent behavior, but the oxidized C*c*O did show a dependent behavior (**Fig.5.2**). Below 40K, the EPR

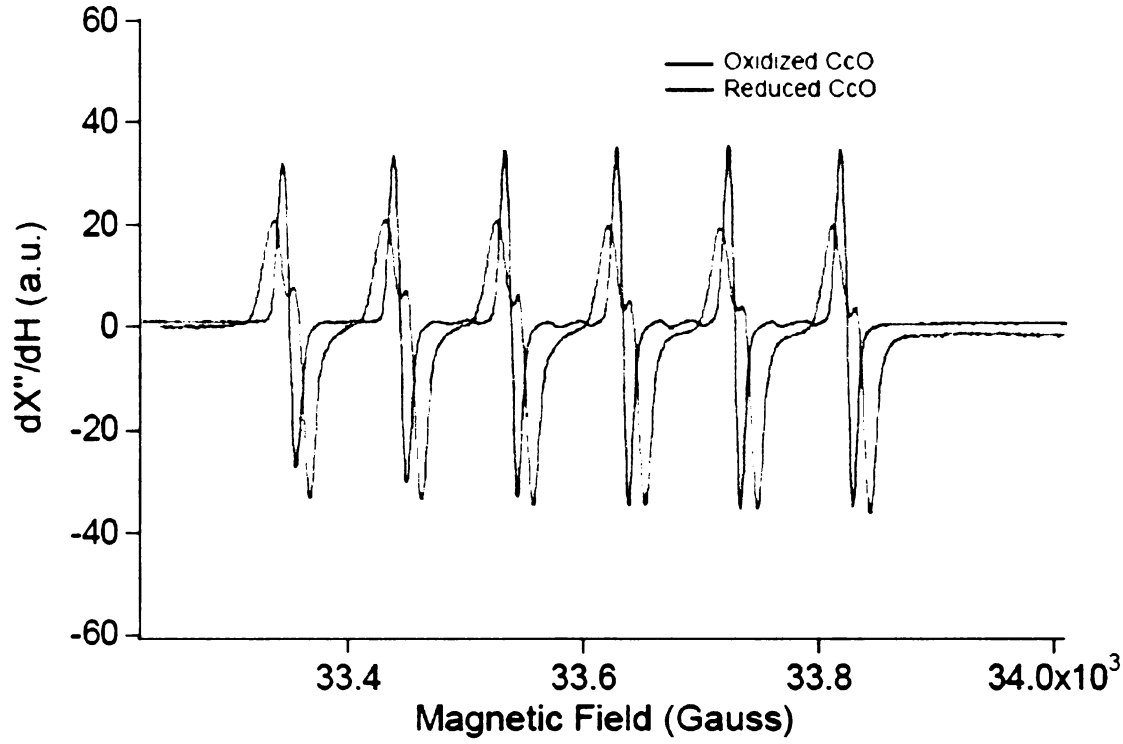

Figure 5.1: The HF-EPR spectra of the oxidized and the reduced wild type C*c*O at 15K. The spectrum of the oxidized C*c*O is shown in red and the spectrum of the reduced C*c*O is shown in blue. The protein sample is in 20mM HEPES-KOH, 14mM KCl, pH 7.4, 0.1% lauryl maltoside with concentration of 50μM. The EPR conditions are: microwave frequency 94.16GHz; microwave power 15.8μW; field modulation amplitude 1G; modulation frequency 10KHz; time constant 327ms.

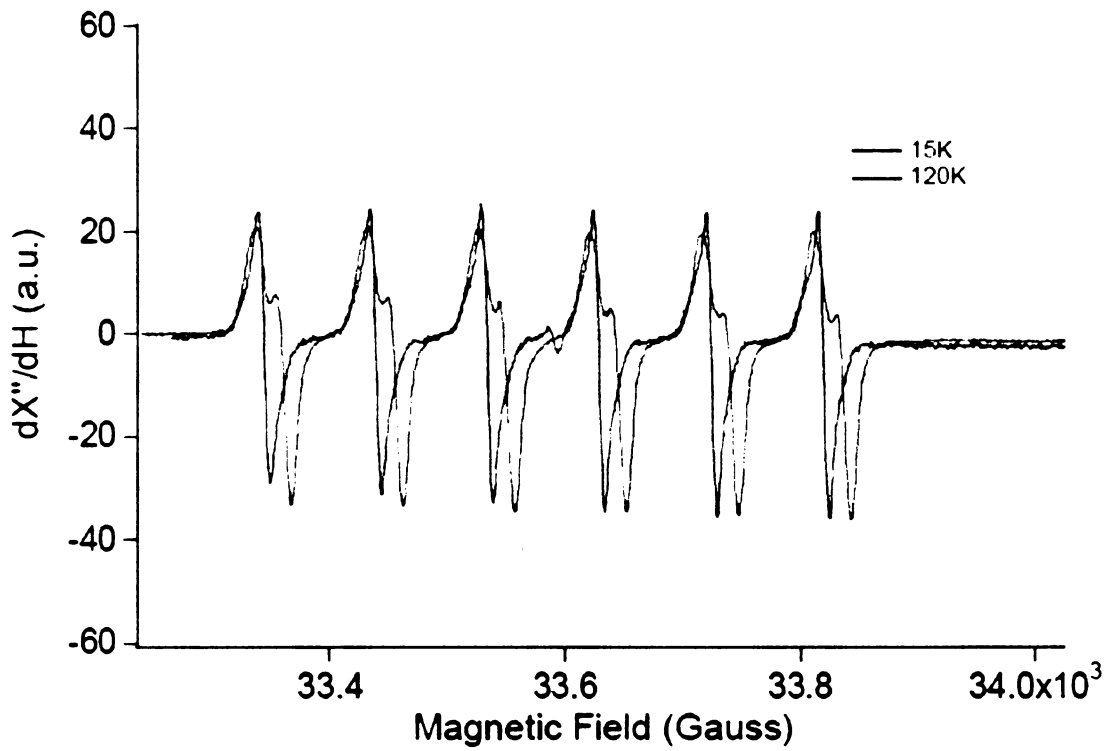

Figure 5.2: The temperature-dependence HF-EPR spectra of the oxidized wild type C*c*O. The red line represents the spectrum of C*c*O at temperature 15K and the blue represents the spectrum of C*c*O at temperature 120K. The sample and EPR conditions are the same as depicted in Fig. 5.1.

spectrum showed the same splittings as observed at 15K. Between 50K and 80K, a change from a splitting doublet to a normal single sextet was observed. Above 90K, the EPR spectrum tended to resemble the spectrum of the reduced C*c*O.

3.2 EPR spectra of the oxidized C*c*O in H_2O and 75% ^2H_2O

The oxidized C*c*O in H_2O and 75% ^2H_2O were studied by HF-EPR at 15K. Both EPR spectra showed the splitting of each peak of the sextet. If carefully examined, the spectrum of the sample in 75% ^2H_2O buffer is slightly narrower, making the dipolar coupling peak more pronounced. When the line widths of the two spectra were measured, it was found that a 2Gauss narrowing in the line width of the ^2H_2O spectrum, which was what we expected to observe if some of the coupled protons were exchanged into deuterons (**Fig. 5.3**).

3.3 EPR spectra of the reduced C*c*O in 75% ^2H_2O and 30% $H_2{}^{17}O$

Fig.5.4 Shows spectra of the reduced C*c*O in water and in 30% $H_2{}^{17}O$ buffer at 15K. The two spectra look almost identical with a normal Mn^{2+} hyperfine pattern. **Fig.5.5** depicts the spectra of reduced C*c*O in water and ^2H_2O at 15K. There was no change in the EPR spectrum for Mn^{2+} upon ^2H_2O exchange.

3.4 Discussion

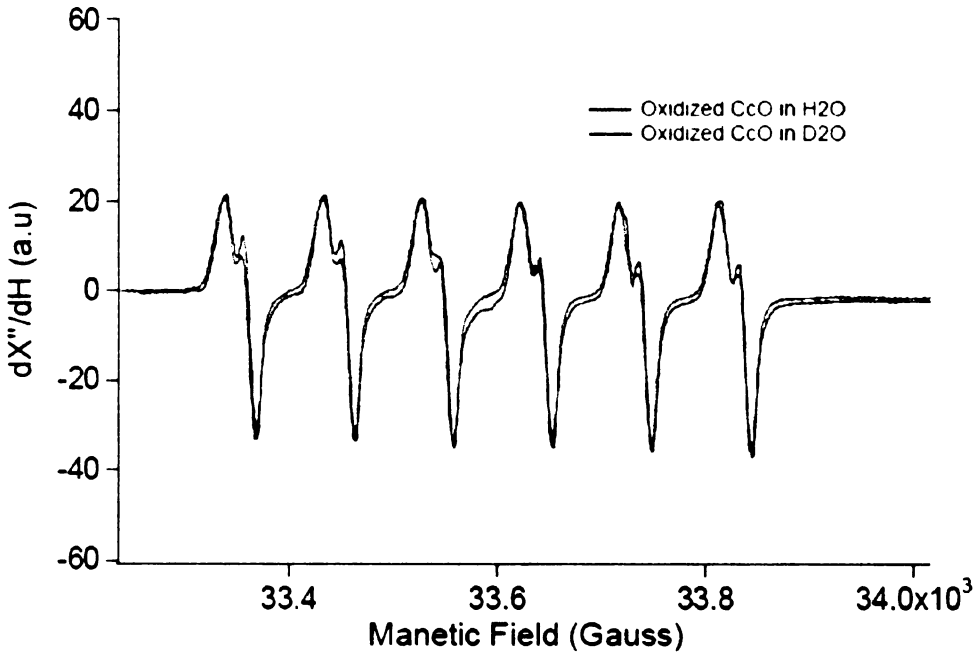

Figure 5.3: The HF-EPR spectra of the oxidized C*c*O in H_2O and ^2H_2O buffers at 15K. The samples and spectrometer conditions are the same as depicted in figure 5.1.

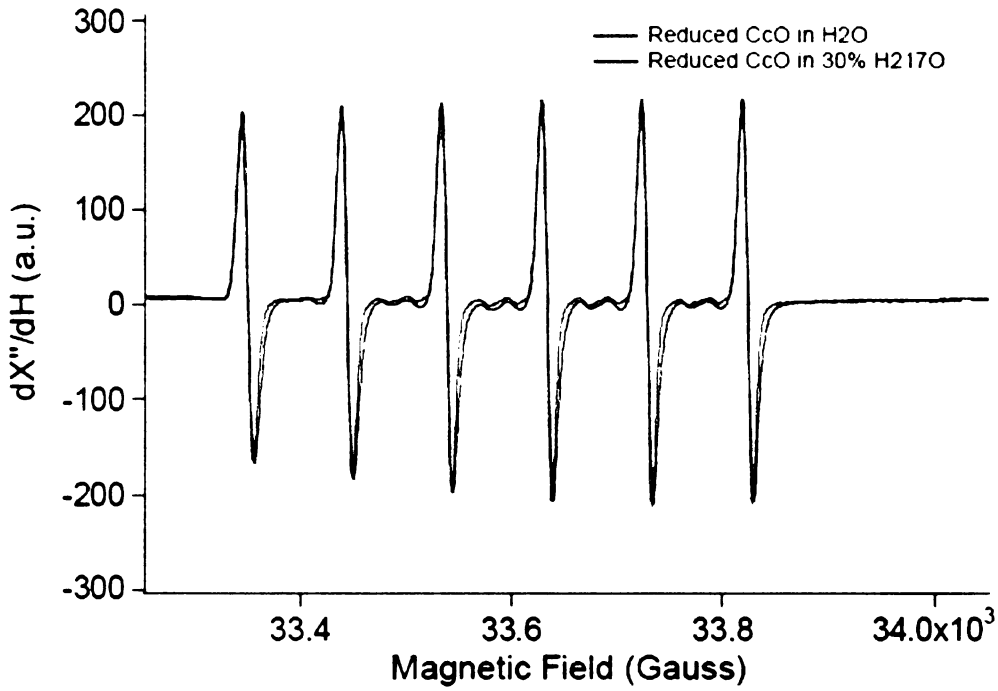

Figure5.4: The HF-EPR spectra of the reduced C*c*O in H_2O and $H_2{}^{17}O$ buffers at 15K. The red line represents the spectrum of the enzyme in H_2O and the blue represents the spectrum of the enzyme in $H_2{}^{17}O$. The protein in 100mM HEPES-KOH, 14mM KCl, pH 7.4, 0.1% lauryl maltoside was first reduced by 25mM dithionite and then diluted by 40% enriched $H_2{}^{17}O$, resulting a protein sample with a final concentration of 50μM and a $H_2{}^{17}O$ enrichment of 30% (v/v).The EPR conditions are the same as depicted in Fig. 5.1

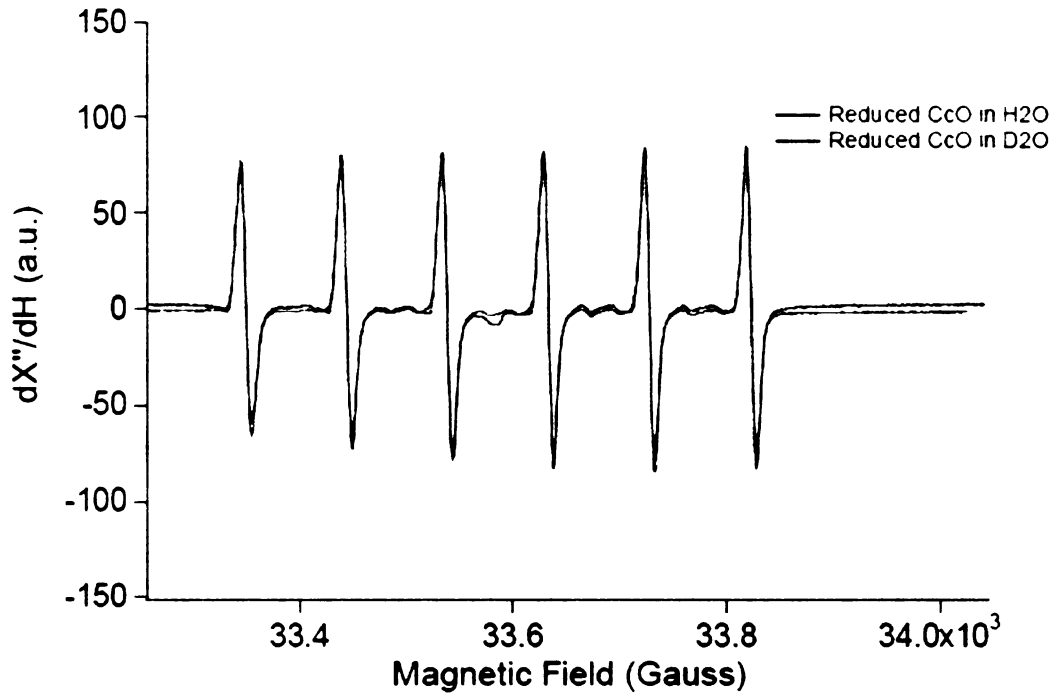

Figure5.5: The HF-EPR spectra of the reduced *Cc*O in H_2O and ^2H_2O buffers at 15K. The red line represents the spectrum of the enzyme in H_2O and the blue represents the spectrum of the enzyme in H_2O. The protein in 100mM HEPES-KOH, 14mM KCl, pH 7.4, 0.1% lauryl maltoside was first reduced by 25mM dithionite and then diluted by ^2H_2O, resulting a protein sample with a final concentration of 50μM and a $H_2{}^{17}O$ enrichment of 80% (v/v). The EPR conditions are the same as depicted in Fig. 5.1.

The difference in the EPR spectra of Mn^{2+} for oxidized and reduced *Pd.* CcO was first reported by Seelig et al. in 1981[5]. The change in the Mn^{2+} EPR signal that is associated with the oxidation state of Cu_A was studied by EPR. The changes were interpreted as a rearrangement in the rhombic octahedral coordination environment of the central Mn^{2+} atom, which is indicative of a redox-linked conformational transition in the enzyme[6]. Later studies of *Rs.* C*c*O, by cw and pulse EPR, indicated that the difference in spectra between oxidized and reduced C*c*O, and therefore the change in geometry of the Mn center upon reduction or oxidation was small[7]. The X-ray crystal structure of bovine C*c*O revealed that Cu_A and Mg shared one ligand, Glu198[1, 13]. This discovery led to an investigation of the Mn site in *Pd.* C*c*O by cw X-, Q-, and W-band EPR methods in 2000[8]. The difference in the Mn EPR spectra was interpreted as the dipolar coupling interaction occurring between the Cu_A site and the Mn^{2+} site. Based on the evaluated dipolar coupling constant, an average distance between these two metal sites was also calculated which was in good agreement with the data from the crystal structure.

The W-band studies of *Rs.*C*c*O in oxidized and reduced states, gave similar results to those observed in *Pd.*C*c*O[8]. The temperature-dependence behavior of the oxidized *Rs.* C*c*O was also similar to that of the *Pd.* C*c*O. Based on all our observations, a conclusion can be drawn that the splittings in the oxidized C*c*O are due to a dipolar coupling interactions between the Cu_A center and the Mn center. Such a high sensitivity of the Mn site to the change in oxidation state of Cu_A can be used as a probe in tracking charge change during the electron transfer process.

The narrowing effect caused by $^{2}H_2O$ was observed in the oxidized C*c*O sample as expected. The modest narrowing effect (about 2Gauss) was promising and prompted us to further experiment with reduced C*c*O which has narrower and simpler spectrum, therefore, easier to observe these effects.

The ^{17}O broadening of EPR spectrum of Mn^{2+}, due to the hyperfine coupling, was used previously to identify ligands for the paramagnetic center and to characterize the metal ligand bonding [11, 14, 15]. In C*c*O, previous data indicated that the Mg/Mn site might play an important role as a water exit. In one experiment, 48%-enriched $H_2{}^{17}O$ water was rapidly mixed in a 1:1 ratio with the oxidized enzyme and then subjected to the X-band cw EPR study. The observed broadening provided the evidence that the $H_2{}^{17}O$ was in a close position to Mn site. Experiments with the reduced C*c*O samples in a 30% ^{17}O-enrichment and 75% ^{2}H-enrichment buffers respectively were performed in high field EPR in the hopes of getting hydration information about the Mn^{2+} site. Unfortunately, the EPR data of C*c*O in ^{17}O and ^{2}H-enriched water buffers failed to show the predicted broadening and narrowing effects, respectively. The unsuccessful trials could be due to higher than we thought temperature, which ruins any solvent effects, let alone the subtle hyperfine coupling effects between the Mn and the ligands. In this respect, temperature control played a crucial role in this experiment and should be given more attention to in the future work.

REFERENCES:

1. Tsukihara, T.; Aoyama, H.; Yamashita, E.; Tomizaki, T.; Yamaguchi, H.; Shinzawa-Itoh, K.; Nakashima, R.; Yaono, R.; Yoshikawa, S., The Whole Structure of the 13-Subunit Oxidized Cytochrome c Oxidase at 2.8 Å. *Science* **1996,** 272, 1136-1144.

2. Hosler, J. P.; Espe, M. P.; Zhen, Y.; Babcock, G. T.; Ferguson-Miller, S., Analysis of Site-Directed Mutants Locates a Non-Redox-Active Metal near the Active Site of Cytochrome *c* Oxidase of *Rhodobacter sphaeroides. Biochemistry* **1995,** 34, 7586-7592.

3. Florens, L.; Schmidt, B.; McCracken, J.; Ferguson-Miller, S., Fast deuterium access to the buried magnesium/manganese site in cytochrome c oxidase. *Biochemistry* **2001,** 40, (25), 7491-7497.

4. Schmidt, B.; McCracken, J.; Ferguson-Miller, S., A discrete water exit pathway in the membrane protein cytochrome c oxidase. *Proc Natl Acad Sci U S A* **2003,** 100, (26), 15539-42.

5. Seelig, A.; Ludwig, B.; Seelig, J.; Schatz, G., Copper and Manganese Electron-Spin Resonance Studies of Cytochrome-C Oxidase from Paracoccus-Denitrificans. *Biochimica Et Biophysica Acta* **1981,** 636, (2), 162-167.

6. Haltia, T., Reduction of Cu_A Induces a Conformational Change in Cytochrome *c* Oxidase from *Paracoccus denitrificans. Biochimica et Biophysica Acta* **1992,** 1098, 343-350.

7. Espe, M. P.; Hosler, J. P.; Ferguson-Miller, S.; Babcock, G. T.; McCracken, J., A Continuous Wave and Pulsed EPR Characterization of the Mn^{2+} Binding Site in *Rhodobacter sphaeroides* Cytochrome *c* Oxidase. *Biochemistry* **1995,** 34, 7593-7602.

8. Kass, H.; MacMillan, F.; Ludwig, B.; Prisner, T. F., Investigation of the Mn binding site in cytochrome c oxidase from Paracoccus denitrificans by high-frequency EPR. *Journal of Physical Chemistry B* **2000,** 104, (22), 5362-5371.

9. Gupta, R. K.; Oesterling, R. M.; Mildvan, A. S., Dual Divalent-Cation Requirement for Activation of Pyruvate-Kinase - Essential Roles of Both Enzyme-Bound and Nucleotide-Bound Metal-Ions. *Biochemistry* **1976,** 15, (13), 2881-2887.

10. Lodato, D. T.; Reed, G. H., Structure of the Oxalate-Atp Complex with Pyruvate-Kinase - Atp as a Bridging Ligand for the 2 Divalent-Cations. *Biochemistry* **1987,** 26, (8), 2243-2250.

11. Reed, G. H.; Leyh, T. S., Identification of the 6 Ligands to Manganese(Ii) in Transition-State-Analogue Complexes of Creatine-Kinase - O-17 Superhyperfine Coupling from Selectively Labeled Ligands. *Biochemistry* **1980,** 19, (24), 5472-5480.

12. Hiser, C.; Mills, D. A.; Schall, M.; Ferguson-Miller, S., C-terminal truncation and histidine-tagging of cytochrome c oxidase subunit II reveals the native processing site, shows involvemet of the C-terminus in cytochrome c binding, and imporves the assay for proton pumping. *Biochemistry* **2001,** 40, 1606-1615.

13. Tsukihara, T.; Aoyama, H.; Yamashita, E.; Tomizaki, T.; Yamaguchi, H.; Shinzawa-itoh, K.; Nakashima, R.; Yaono, R.; Yoshikawa, S., Structure of Metal Sites of Oxidized Bovine Heart cytochrome c Oxidase at 2.8 Å. *Science* **1995,** 269, 1069-1074.

14. Bellew, B. F.; Halkides, C. J.; Gerfen, G. J.; Griffin, R. G.; Singel, D. J., High frequency (139.5 GHz) electron paramagnetic resonance characterization of Mn(II)-(H2O)-O-17 interactions in GDP and GTP forms of p21 ras. *Biochemistry* **1996,** 35, (37), 12186-12193.

15. Rohrer, M.; Prisner, T. F.; Brugmann, O.; Kass, H.; Spoerner, M.; Wittinghofer, A.; Kalbitzer, H. R., Structure of the metal-water complex in Ras center dot GDP studied by high-field EPR spectroscopy and P-31 NMR spectroscopy. *Biochemistry* **2001,** 40, (7), 1884-1889.